POLITECNICO DI MILANO

School of Industrial and Information Engineering

Master of science degree in
Engineering Physics

Spectroscopic characterization of excitons in 2D van der Waals heterostructures

Supervisors: Prof. Alberto BRAMBILLA
Prof. Brian D. GERARDOT

Co - Supervisor: Prof. Paolo BIAGIONI

M.Sc. thesis by:

Giovanni MASCIOCCHI
Matr. 915432

Academic Year 2019 – 2020

Acknowledgement

I would like to thank Prof. Brian Gerardot and his group at Heriot Watt University for their help in this final year project. In particular Mauro for his knowledge in coding and Aidan and Raphael for being patient with me and teaching me how to be a "good experimentalist".

My gratitude goes also to my supervisor at Politecnico di Milano, Prof. Alberto Brambilla, who was keeping track of my work in spite of the distance.

To my parents, Loretta and Giorgio.

Estratto

Sin dalla scoperta del grafene, nel 2004, l'interesse per i materiali bidimensionali ha mostrato un'incredibile crescita. L'investigazione di materiali atomicamente sottili portò alla realizzazione di singoli strati atomici di dicalcogenuri di metalli di transizione (TMD), semiconduttori a band gap diretta con notevoli proprietà optoelettroniche. Tutti questi materiali esistono nella forma di fogli 2D a causa della loro struttura atomica: forti legami covalenti nel piano e deboli forze di van der Waals tra piani paralleli, infatti, rendono possibile la separazione e la stratificazione di fogli di materiali differenti dando forma alle cosiddette etero strutture di van der Waals.

Questo elaborato contiene i risultati del progetto di ricerca svolto ai Quantum Photonics Laboratories della Heriot Watt University nel Regno Unito, incentrato sulla caratterizzazione sperimentale degli eccitoni nei materiali bidimensionali WSe_2 e $MoSe_2$ e relative etero strutture, usando tecniche spettroscopiche sia a temperatura ambiente, che a pochi Kelvin. In particolare, due tecniche spettroscopiche sono state usate: ellissometria a temperatura ambiente in una atmosfera inerte, e spettroscopia di luce bianca confocale a temperature criogeniche. I risultati sperimentali, così come i vantaggi di ognuna di queste tecniche, sono presentati in questo scritto. Sia l'ellissometria che la spettroscopia di luce bianca ci permettono di osservare la manifestazione di marcate transizioni eccitoniche in questi sistemi bidimensionali; tuttavia solo la spettroscopia di luce bianca ci ha dato accesso agli stati eccitati degli eccitoni a causa della riduzione del contributo energetico dei fononi.

Introdotta la struttura elettronica e le proprietà ottiche dei TMD atomicamente sottili, nel primo capitolo si pone particolare attenzione alle proprietà uniche proprie dei materiali bidimensionali come la formazione di eccitoni fortemente legati, principalmente dovuta al debole schermo dielettrico di materiali atomicamente sottili. Nel secondo capitolo, vengono presentate le tecniche sperimentali utilizzate assieme al formalismo matematico usato per descrivere la propagazione della luce in una struttura stratificata. I risultati sperimentali e la discussione di questi sono l'argomento del capitolo 3. Differenti campioni di singoli strati di TMD sono stati sottoposti a misurazioni, mostrando che sia la energia che la larghezza di riga delle transizioni eccitoniche in questi materiali bidimensionali dipendono fortemente dalla composizione dielettrica dei materiali circostanti.

Infine, è stato investigato l'effetto di un forte campo magnetico esterno, applicato perpendicolarmente al campione, usando dei magneti superconduttori incorporati nel

criostato e un setup per luce polarizzata circolarmente. Questi risultati aprono le porte ad innumerevoli possibili applicazioni per l'ingegnerizzazione delle proprietà ottiche dei materiali bidimensionali. Da ultimo, l'appendice contiene una breve descrizione dei codici di programmazione usati per l'analisi dei dati e il calcolo numerico.

Milano, Giugno 2020

Abstract

Since the discovery of graphene in 2004 the interest for 2D materials has experienced an extremely fast growth. The investigation of thin materials brought the realization of monolayer transition metal dichalcogenides: direct band semiconductors with remarkable optoelectronic properties. All these materials exist in the shape of 2D nanosheets due to the nature of their atomic structure: strong in-plane covalent bonding and weak out-of-plane van der Waals forces make feasible the isolation and stacking of sheets of different materials forming the so-called van der Waals heterostructures. This report contains the results of a research project developed in the Quantum Photonics Laboratory of Heriot Watt university (UK) and focuses on the experimental characterisation of excitons in WSe_2 and $MoSe_2$ monolayers and related heterostructures by optical spectroscopy techniques at both room and cryogenic temperatures. In particular, two different optical spectroscopy techniques have been used: ellipsometric imaging characterisation at room temperature in an inert environment, and broadband confocal differential reflectivity at cryogenic temperatures. The experimental results, as well as the advantages of each one of these techniques, are discussed in this report. Both ellipsometric imaging and broadband differential reflectivity allow us to observe the manifestation of strong excitonic transitions in these 2D systems, although only differential reflectivity measurements at cryogenic temperatures give access to higher exciton excited states due to the reduction of the phononic contributions.

This report starts with an introduction to the electronic band structure and optical properties of atomically thin TMDs. Particular attention has been given to the unique properties exhibited by the 2D materials such as the formation of strongly bounded excitons mainly due to the weak and highly non-local dielectric function of atomically thin crystals. In the second chapter, the experimental techniques employed in our investigation have been presented along with the mathematical formalism commonly used to describe the optical properties of layered structures. The experimental results and the discussion can be found in chapter 3. Different samples of monolayer TMDs have been measured. Our results show that both the energy and the linewidth of the excitonic transitions in these 2D materials are strongly dependent on the local dielectric environment of the 2D excitons.

Moreover, the effects of a strong out of plane magnetic field on the sample have been investigated using superconducting magnets embedded in the cryostat and a setup for circularly polarized light. These results open the door to a number of possible applica-

tions to engineer the optical properties of 2D van der Waals semiconductors. At last, the appendix contains a brief description of the codes used for data analysis and numerical fitting.

Milan, June 2020

Contents

List of Figures

List of Tables

Chapter 1

Properties and applications of thin TMDs

Since the discovery of graphene in 2004 a new class of material became a growing subject of studies. 2D materials are atomically thin layers that possess different physical properties with respect to the bulk form and can be used in a completely new monolayer design. In particular, the possibility of stacking a wide variety of 2D layers on upon the other without any lattice-matching constrains, creating a so called "Van der Waals" heterostructure, allows to engineer its properties and to create specific micro sized devices. These stable novel materials look promising in electronics and photonic applications. In this report the excitons of two representative transition metal dichalcogenides will be investigated using different techniques with the aim of unraveling the effects of the local dielectric environment on the 2D excitons in these materials.

The first chapter is used to present the optical properties of the atomically thin TMD with particular attention to excitons. In this way it will be possible to have both a theoretical background, for a better understanding of the results, and a comprehension of the motivation and the relevance of investigating 2D materials.

1.1 Optical properties of TMDs

One kind of 2D materials are transition metal dichalcogenides (TMDs). Those have been widely studied in the last 10 years due to the relevance of their unique properties for optical and optoelectronic applications making them possible candidates to be used in the silicon industry. TMDs are in the form MX_2 where M is a metal (e.g. Mo, W) and X is a dichalcogenide i.e. an element from group 16 of the periodic table of elements (as Se, Te, S) [**1**] . These materials in the bulk form are made by covalently bounded monoatomic layers held together by weak Van der Waals forces. This makes possible the isolation of a single (or few) atomic layer using mechanical exfoliation or their synthesis by chemical vapor deposition[**2**]. One particular optical property of 2D materials is the change of the electronic band structure: when passing from bulk to monolayer it is possible to obtain a direct band gap. The reduction of interlayer interaction indeed produces a lowering of the valance band energy resulting in a indirect to direct bandgap transition. This gives an improvement in the light absorption and in the photoluminescence intensity making these materials ideal for optical applications.

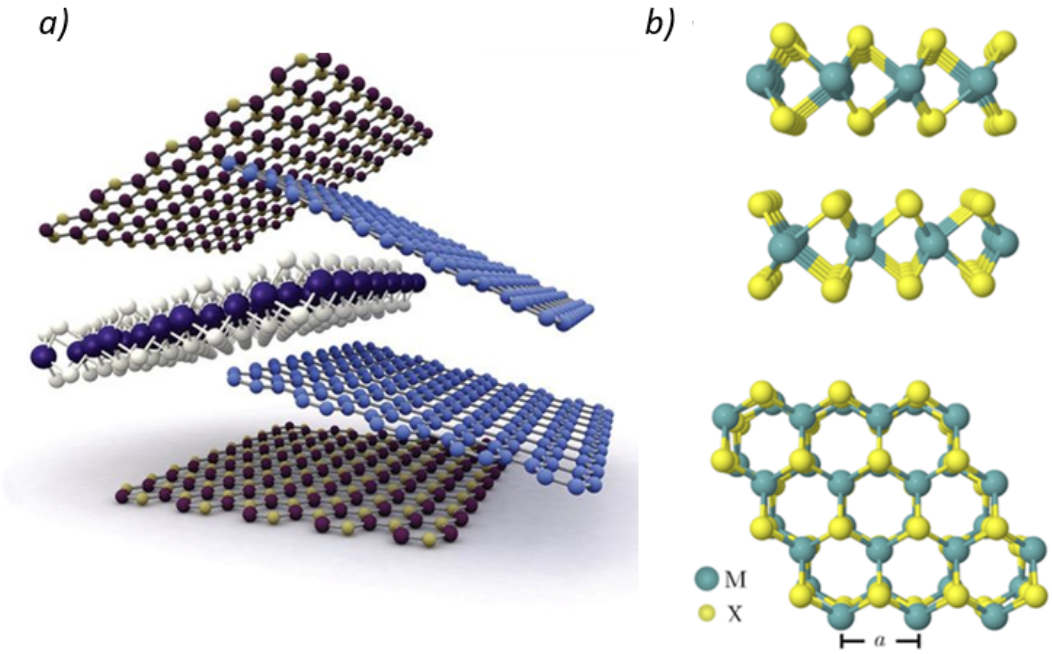

Figure 1.1: *a) Representation of a laye rstack made of 2D materials. The possibility to have extremely thin layers with reduced lattice mismatch, allows the engineering of material properties in the so-called van der Waals heterostructures. b) Side and top view of the hexagonal lattice structure of a transition metal dichalcogenide. Each monolayer contains an heavy metal (M) and a chalcogene atom (X).* From [**3**] and [**4**].

1.1.1 Electronic band structure of TMDs

In this section the electronic band structure and the fundamental interband (i.e. within the conduction and valence bands) transitions will be presented. As previously

mentioned, the TMDs in the form of monolayer change their bandgap becoming direct semiconductors at the K point of the first Brillouin zone of the hexagonal crystal structure, shown in figure 1.1. This is due to the lack of any interlayer interactions in the TMDs monolayer [**5**] and can be seen in figure 1.2 a). This band structure is similar to the one of graphene where the bandgap is originated by the lack of sublattice symmetry [1] [**6**]. Using the tight binding method (TBM) it is possible to write the combination of atomic orbitals used at the K point to calculate energy around E_f. Electrons from d orbitals of metal have been combined with electrons from p orbitals in the chalcogenide. Only one projection of the angular momentum has been considered because lacks inversion symmetry, however the system still has time reversal symmetry and that is why in the K' points the sign is changed. The atomic orbitals used are

$$\begin{array}{ll} \textbf{VBMax (K point)} & \alpha \mid \psi^{M}_{2,-2} > +\beta 1/\sqrt{2}\left(\mid \psi^{X_1}_{1,-1} > + \mid \psi^{X_1}_{1,-1} >\right) \\ \textbf{CBMin (K point)} & \alpha \mid \psi^{M}_{2,0} > +\beta 1/\sqrt{2}\left(\mid \psi^{X_1}_{1,1} > + \mid \psi^{X_1}_{1,1} >\right) \\ \textbf{VBMax (K' point)} & \alpha \mid \psi^{M}_{2,2} > +\beta 1/\sqrt{2}\left(\mid \psi^{X_1}_{1,1} > + \mid \psi^{X_1}_{1,1} >\right) \\ \textbf{CBMin (K' point)} & \alpha \mid \psi^{M}_{2,0} > +\beta 1/\sqrt{2}\left(\mid \psi^{X_1}_{1,-1} > + \mid \psi^{X_1}_{1,-1} >\right) \end{array} \tag{1.1}$$

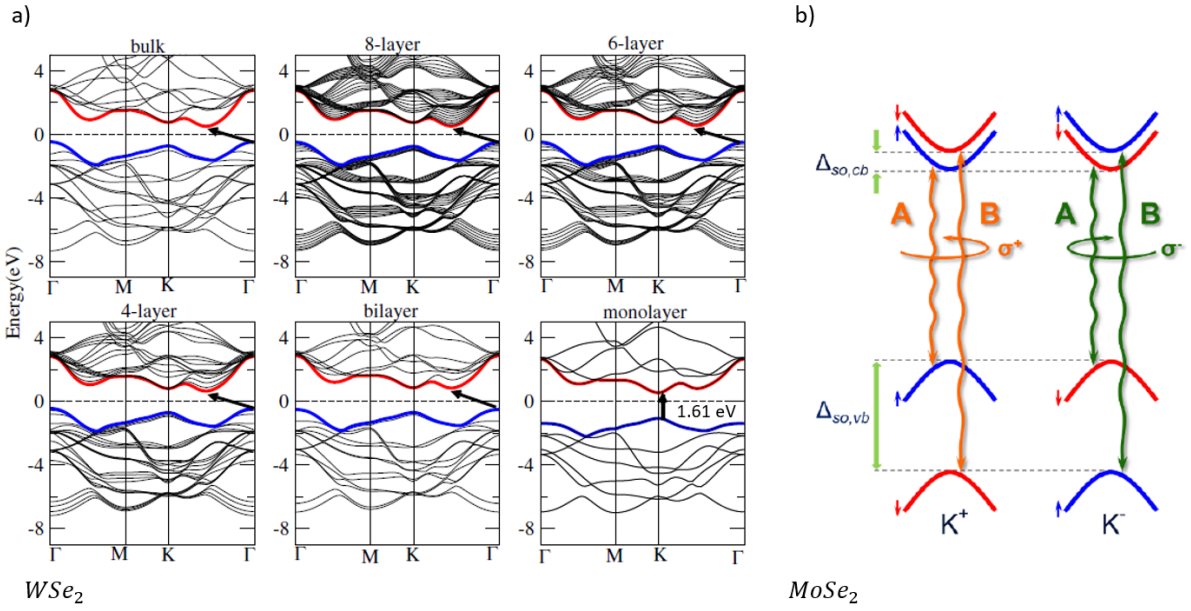

Figure 1.2: *a)Electronic band structure of bulk WSe2, its monolayer, as well as multy-layers calculated ab initio. The top of the valence band is highlighted in blue while the bottom of the conduction band is in red. The arrow indicates the smallest value of the band gap (direct in the case of monolayer). The Fermi level is set at 0 eV. b) Diagram of subbands in the conduction and valence bands at the K^+, K^- points of the Brillouin zone in monolayer MoX_2 and WX_2. The blue (red) curves indicate the spin-up (spin-down) subbands. The wavy lines show the A and B transitions associated with the σ^+ and σ^- polarizations, respectively.* From [**7**] and [**6**].

where α and β are coefficients that can be found with the normalization condition on

[1] This is due to the presence of alternating M and X-enes in the lattice hexagons.

the electronic wavefunction [**8**]. Spin-orbit interaction is then applied to heavy transition metals giving the result shown in figure 1.2 b).

Spin-orbit coupling is a pure quantum effect of a particle with spin moving in a potential. This applies to electrons inside the atoms and can be understood in a semi-classical description of the electron describing an orbit around the nucleus. Let us consider a Hydrogen atom. It is known that has an intrinsic magnetic dipole moment related to its spin. Moreover, the positive charge of the nucleus is moving in the reference frame of the electron and sets up a magnetic field B. This can be calculated[**9**] by the Biot-Savart Law [2]

$$\mathbf{B} = \frac{e}{4\pi\epsilon_0 mc^2 r^3}\mathbf{L} \tag{1.2}$$

Where $\mathbf{L}$ is the electron orbital angular momentum that points in the same direction of $\mathbf{B}$. A magnetic dipole moment in a magnetic field feels a torque and the Hamiltonian of this interaction is

$$H = -\boldsymbol{\mu} \cdot \mathbf{B}. \tag{1.3}$$

The electron magnetic moment turns out to be

$$\boldsymbol{\mu_e} = -\frac{e}{m}\ \mathbf{S} \tag{1.4}$$

and putting all together the spin orbit interaction Hamiltonian is

$$H'_{so} = \left(\frac{e^2}{8\pi\epsilon_0}\right)\frac{1}{m^2c^2r^3}\mathbf{S}\cdot\ \mathbf{L}. \tag{1.5}$$

Using perturbation theory one can calculate the energy levels of the Hydrogen atom including the spin orbit contribution. Due to equation (1.5) the energy ladder will depends on the total angular momentum $\mathbf{J} = \mathbf{L}+\mathbf{S}$ and therefore, degeneracy for energy levels with same quantum number n is now lifted. Only in case $l = 0$ the spin orbit correction is zero, this is the case of atomic orbitals with orbital angular momentum equal to zero.

-	MoS_2	$MoSe_2$	WS_2	WSe_2
$\Delta_{so,cb}[meV]$	3	20 - 22	-29 - -32	-36- -37
$\Delta_{so,vb}[meV]$	138-150	180-202	379-429	400-510

Table 1.1: *Amplitude of the spin-splitting at the K points of the Brillouin zone in the conduction $\Delta_{so,cb}$ and valence $\Delta_{so,vb}$ bands in monolayer S-TMDs deduced from theoretical predictions and experimental results.* From [**10**] and [**11**].

[2] This is true if we consider the movement of a charged particle as a continuous current loop: $B = \frac{\mu_0 I}{2r}$ where I is the effective current.

The splitting is larger at the valence band maxima since these molecular orbitals are made by atomic orbitals with large angular momentum. Table 1.1 contains the amplitude of the spin orbit splitting in some TMDs. Going back to the band structure of TMDs, one can note that K and K' valleys are related to different states, but their energy is the same due to time reversal symmetry. No inversion center leads to a new degree of freedom of carriers associated with the K-valley index (the so called valleytronics). It is possible to distinguish between these two states only if a magnetic field or circular polarized light are applied: the latter allows to selectively excite the electronic population of the two valleys. In the valence band, electrons have a magnetic moment different from zero, and breaking of symmetry (both inversion and time reversal) lead to magnetic moments oriented in different direction. This causes the valley dependent optical selection rules.

The large spin orbit splitting for the valence band $\Delta_{so,vb}$ is responsible for the two main interband transition called A and B transitions at a first approximation, see figure (1.2 b)). The smaller splitting for the conduction band due to the $d_{2,0}$ orbital of the transition metals makes possible to describe further transitions considering second order effects. These are due to the contribution coming from both the transition metal and the X-enes (chalcogen atoms) p orbitals[3]. The first and second order effects have different sign contribution, that means that two different possibilities are likely to happen. The first one has optically active ground state transition since the spin is aligned in the upper VB and lower CB sub bands. Such material is called optically bright monolayer. The second scenario is the case of antiparallel spin in the upper VB and lower CB [**6**]. According to their band structure $MoSe_2$ is expected to be bright and WSe_2, WS_2 are darkish. In the same way, one can distinguish exciton whose recombination gives rise to emission of light from the one whose transition is not dipole allowed[**12**]. Optically bright excitons are bounded pair of electron and hole in two electronic states with same spin orientation. This is due to the fact that, in an optical transition, the spin of the initial and final state must be conserved[4]. If, on the other hand, the electron hole pair is formed between two levels with opposite spin, the exciton is called dark.

It is worth to mention that the direct-bandgap nature of the TDMs explains the pronounced absorption band edge visible in absorbance/reflectance experiments that sums to the A and B transitions cited above. Nevertheless, a complete description of the optical properties of TDMs requires the consideration of excitonic effects.

[3]Since the interaction goes like Z^4 where Z is the atomic number and requires a non-null angular momentum, the contribution from the X atom will be in general weaker.

[4]This comes from the selection rules for electric dipole transitions. Other transition are allowed but they take place at far lower rate than the transition that are allowed according to the electric dipole approximation.

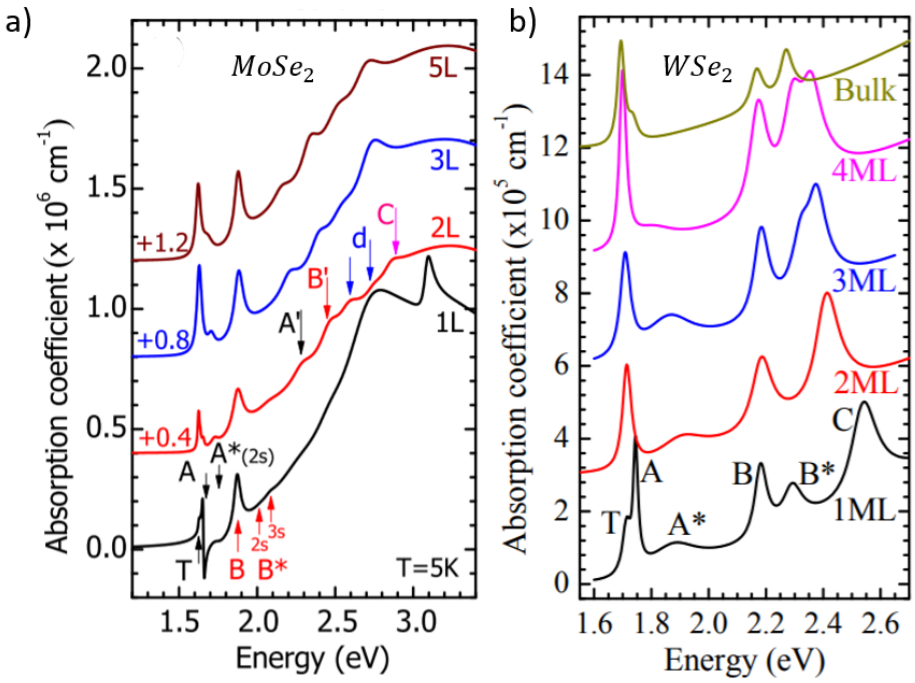

Figure 1.3: *Absorption coefficients for a) $MoSe_2$ and b) WSe_2 measured at low temperature on flakes of different thickness. It is possible to notice both the excitonic absorption peaks and the absorption band edge.* From [**13**].

In figure (1.3) is possible to see the absorption coefficient spectra of two different materials: $MoSe_2$ and WSe_2, respectively. The absorption coefficient is the fraction of shined light onto the sample that is neither transmitted nor reflected and its determination is of great relevance in optoelectronics since describes the interaction of thin TMDs with light. The absorption coefficient α from the Lambert Beer law [5] is indeed related to the refractive index $n = n_1 + in_2$ of the material via the plane wave expression

$$E(x,t) = Re\left[E_0 e^{i(kx-\omega t)}\right] = e^{-2\pi n_2 x/\lambda_0} Re\left[E_0 e^{i(n_1 x-\omega t)}\right] \tag{1.6}$$

With an exponential decay as predicted by the Lambert Beer law. Where the attenuation coefficient becomes

$$\alpha = \frac{4\pi n_2}{\lambda_0} \tag{1.7}$$

When one talks about 2D materials on infinite substrate, the absorbance is usually experimentally determined using the differential reflectivity. For a layered system such as TMDs materials, when thickness is $t << \lambda$ the absorbance can be written as [**14**]

$$A = 1/4(n_s^2 - 1)\frac{\Delta R}{R} \tag{1.8}$$

Where n_s is the substrate refractive index and $\frac{\Delta R}{R}$ is the reflectance contrast of the TMDs with respect to the substrate. In particular for excitons peaks determination just

[5] The Lambert Beer law expresses the attenuation in intensity of the radiation passing through a material as $I(x) = I(0)e^{-\alpha x}$ where I(x) is the intensity of the radiation at a depth x in the material.

$\frac{\Delta R}{R}$ is necessary since it is proportional to the absorption of light in the material. All monolayers of molybdenum and tungsten dichalcogenides display very strong absorption at excitation peaks up to 10% for a single layer[**1**]. This is due to the light-matter interactions of the material and to the presence of band edge excitons. The energy separation between the A and B exciton states in WSe_2 is about 0.4eV[**1**], and is larger compared to the other TMDs due to the strong spin orbit coupling of tungsten.

As it will be explained in more details in chapter 2, the dielectric function can be modeled and experimentally determined by the absorption coefficient using Kramers-Kronig constrained analysis of the reflectance spectra of the monolayer on a transparent substrate. In particular a common way to model the imaginary part of the dielectric function of monolayer TMDs is to use a superposition of Lorentzian oscillators[**15**].

1.1.2 Magnetic effects on the band structure

In this section, the effects of magnetic field on electronic energy levels will be introduced with particular attention to the modification of band structure and electronic population of thin TMDs. Indeed magnetic field can be used to tune the band structure of these monolayers allowing the investigation of novel physics and the use of 2D materials in a wide range of possible application. One of the most known phenomena concerning magnetic fields in solid state physics is the Zeeman effect. It has been experimentally observed as a shift in the energy levels when an atom is placed in a uniform magnetic field. If one considers, for sake of simplicity, a single electron system, the perturbative Hamiltonian is

$$H'_Z = -(\boldsymbol{\mu_l} + \boldsymbol{\mu_s}) \cdot \mathbf{B}_{ext} \tag{1.9}$$

where $\boldsymbol{\mu_s}$ and $\boldsymbol{\mu_l}$ are , respectively, the magnetic dipole moment associated with electron spin and orbital motion. Therefore

$$H'_Z = \frac{e}{2m}(\mathbf{L} + 2\mathbf{S}) \cdot \mathbf{B}_{ext}. \tag{1.10}$$

Let us now consider the case of a weak external magnetic field [6], i.e. $B_{ext} << B_{int}$. In this case the Zeeman effect can be treated as a small perturbation. Using perturbation theory the Zeeman correction to energy is

$$E_Z = \frac{e}{2m}\mathbf{B}_{ext} \cdot < \mathbf{L} + 2\mathbf{S} > \tag{1.11}$$

where, by considering the time average of S one can simplify [**9**] this expression using the Lande g-factor g_J

$$E_Z = \mu_B g_J B_{ext} m_j \tag{1.12}$$

where μ_B is the Bohr magneton and m_j is the azimuthal eigenvalue for the orbital angular momentum, since $\mathbf{B}_{ext}$ has been chosen to be on the arbitrary defined z-axis. This means that the degeneracy for the quantum number m_j can be broken by an applied magnetic field and the energy shift is linear with $\mathbf{B}_{ext}$. Since $m_j = -j, -(j-1), \ldots j-1, j$, $j = l + s$, this phenomenon is often called Zeeman splitting since energy levels are

[6] The strong and weak field can be quantitatively characterized by means of $\mathbf{B}_{int} = \frac{e}{4\pi\epsilon_0 mc^2 r^3}\mathbf{L} \simeq 12T$. Using $r = a$ (hydrogen ground state radius) and $L = \hbar$

originated symmetrically with respect to a single spectral line. This effect is due to the symmetry breaking of the magnetic field. A magnetic field strongly modifies the excitons properties, this can be experimentally seen by applying a strong out of plane magnetic field to the sample[7]. Since the Zeeman shift is an odd function of the **B** field, the difference in energy at opposite intensities, corresponds to the Zeeman splitting energy. Considering the band structure of TMDs, the two valleys at K and $-K$ points of the first Brillouin zone are normally degenerate. When an out of plane magnetic field is applied, the valley degeneracy is lifted due to the opposite spin and orbital configuration of the two time reversal-valleys[**16**]. Therefore the bandgap at one valley is enlarged while at the other one it is reduced. This difference is the Zeeman valley splitting energy that can be expressed as

$$\Delta E_Z = g\mu_B B \tag{1.13}$$

where g is the effective g-factor and $\mu_b = 5.78810^{-5} eV/T$. One expects that the major contribution comes from the d-type orbitals of the valence band, having opposite azimuthal quantum numbers $m_j = \pm 2$ in the two valleys. Therefore they contribute to an effective g-factor of -4 in the Zeeman splitting[**17**]. This can be observed in figure (1.4).

The second magnetic effect we are considering is the diamagnetic shift, an increase in energy of both spin-split levels with magnetic field. In the case of a weak applied magnetic field, the energy increases quadratically with the applied field. This contribution can be calculated with perturbation theory. To describe it [**18**], one can consider the effect of a constant magnetic field perpendicular to the 2D material using the Hamiltonian

$$H = \frac{1}{2\mu}(\mathbf{p} + e\mathbf{A})^2 + V = \frac{1}{2\mu}(p^2 + 2e\mathbf{p}\cdot\mathbf{A} + e^2A^2) + V \tag{1.14}$$

where $\mathbf{A} = 1/2\mathbf{B}\times\mathbf{r}$ and $\mathbf{p}\cdot\mathbf{A} = \frac{1}{2}\mathbf{B}\cdot(\mathbf{r}\times\mathbf{p}) = \frac{1}{2}\mathbf{B}\cdot\mathbf{L}$. Excitons are s-like states with $\mathbf{L} = 0$ so the term $\mathbf{p}\cdot\mathbf{A}$ is zero. The hamiltonian for the diamagnetic term is therefore

$$H_{DM} = \frac{e^2}{8\mu} r^2 B^2 \tag{1.15}$$

The diamagnetic shift of an exciton can be expressed, using perturbation theory, as [**19**]

$$\Delta E_{DM} = \frac{e^2}{8\mu} < r^2 > B^2 = \sigma B^2 \tag{1.16}$$

Where $\mu = (m_e^{-1} + m_h^{-1})^{-1}$ is the exciton's reduced mass and $< r^2 >$ is the expectation value on the envelope wave function of the radial coordinate of the exciton and its root mean square radius is $r = \sqrt{< r^2 >} = \sqrt{8\sigma\mu}/e$.

[7] This is due to the fact that in 2D materials, the current circulation from the orbitals can only be within the plane.

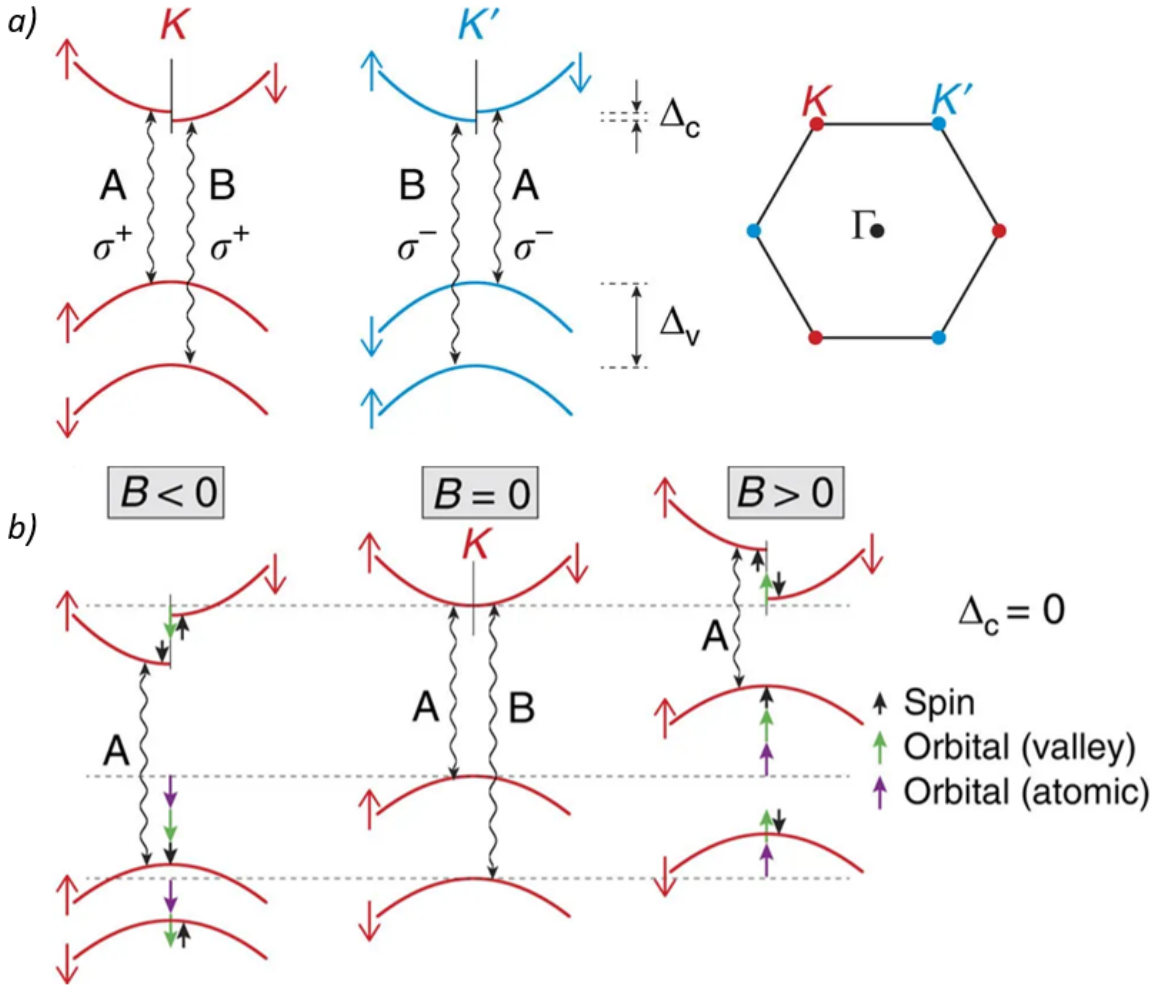

Figure 1.4: *a)Diagrams of the conduction and valence bands at the K and K' valleys of the monolayer transition-metal dichalcogenides, showing the A and B exciton transitions, the associated optical selection rules and the spin orbit coupling of energy levels. b) Diagrams depict the relative shifts of the conduction and valence bands in the K valley. By time-reversal symmetry, the shifts depicted here for $B<0$ in the K valley are equivalent to those in the K' valley (σ^- transitions) when $B>0$. From* [**19**]

A large high-ling exciton is expected therefore to have a larger diamagnetic shift. The TMDs are particularly suitable for optical observation of the Zeeman splitting. The hexagonal nature of these material and the broken inversion symmetry allow the valley polarization of the electron population at the points K and -K. This is due to the fact that the spin orbit coupling splits the bands with opposite spin configuration as can be seen in figure 1.4. The optical selection rules allow to selectively excite electrons in the two valleys separately using, respectively, σ^+ and σ^- circularly polarized light obtaining the Zeeman splitting as $E_{\sigma^+} - E_{\sigma^-} = g\mu_B B$. Both the theoretical and the experimental behavior of a material in a constant magnetic field can be seen in figure (1.5).

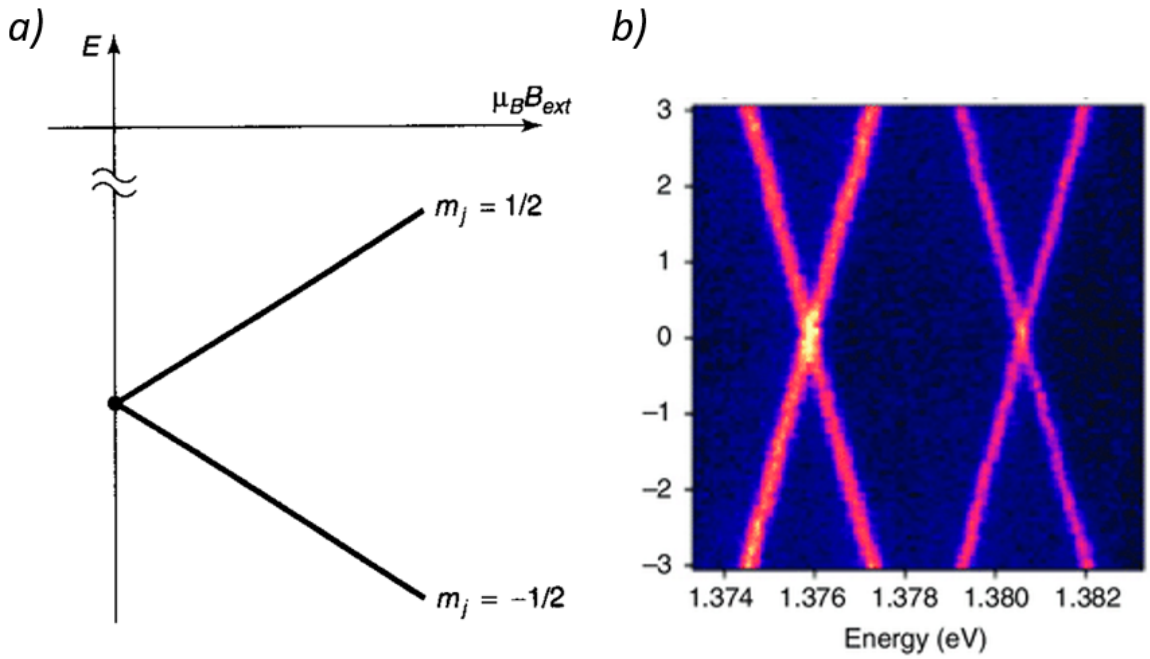

Figure 1.5: *a) Weak field Zeeman splitting for the Hydrogen atom ground state, from* [**9**].*b) Zeeman splitting of the polarization-resolved PL of excitons in Moire superlattice, from* [**20**].

1.2 Excitons in TMDs

Excitons are hydrogen-like bounded states of an electron-hole pair in a material due to Coulomb interaction. They usually have origin in semiconductors when optically excited, are often characterized by a spectrally narrow linewidth and can efficiently emit light when recombination occurs. This electron hole pair can be described as an hydrogenic atom possessing discrete energy levels, internal fine structure and excitation energies lower than the energy gap; this feature allows in principle the realization of electronic and optical devices at the nanoscale. Nevertheless, excitons are often difficult to be used in bulk semiconductors due to the low binding energy[8] (usually $1 - 10meV$) due to high dielectric screening and small quasi-particle mass [**5**]. On the other hand, in 2D semiconductors, as for example monolayers TMDs, the reduced dielectric screening makes excitonic states bounded at room temperature with a binding energy up to hundreds of meV. The photoluminescence and absorption spectrum of these materials is therefore dictated by excitons.

In this paragraph a theoretical description along with some experimental consideration are presented. At first excitons will be described when located in bulk materials: later a description in case of TMDs monolayers is reported in order to compare the two cases. In the last part eventually the dielectric screening and its influence on the exciton binding energy will be discussed. The importance of this effect is crucial in the investigation and understanding of how the dielectric environment influences excitons in a monolayer when stacked in a van der Waals heterostructure.

1.2.1 Excitons in bulk semiconductors

In order to describe bulk excitons[9], let us consider a semiconductor with isotropic and parabolic dispersion relation at $k = 0$ such as

$$\epsilon_c(k) = \epsilon_c(0) + \frac{\hbar^2 k^2}{2m_e} \tag{1.17}$$

$$\epsilon_v(k) = \epsilon_c(0) - \epsilon_g + \frac{\hbar^2 k^2}{2m_k} \tag{1.18}$$

Where ϵ_g is the band gap energy and $m_{e,h}$ effective mass of electrons and holes, respectively. One can write the energy for one-electron excitation as:

$$\epsilon_c(k) - \epsilon_v(k - K) = \epsilon_g(K) + \frac{\hbar^2(k - \frac{m_e}{M}K)^2}{2\mu} = E(k, K) \tag{1.19}$$

Where $\epsilon_g(K) = e_g + \frac{\hbar^2 K^2}{2M}$, $M = m_e + m_h$ and μ is the reduced mass. The wavevectors K and $k - \frac{m_e}{M}K$ represent the motion of electron in the conduction band and hole in the valence band, respectively, both for relative and translational motion. In the excited state there should be an attractive Coulomb potential and repulsive exchange interaction

[8] The binding energy of an exciton in a bulk semiconductor such as Si or GaAs are negligible with respect to thermal fluctuation at room temperature $\simeq 25meV$.

[9] The following derivation is taken from the book "Excitonic processes in solids" [**21**].

between the electron hole pair. If their distance $r = |r_e - r_h|$ is large compared to the lattice constant the material can be treated as medium with dielectric constant ϵ and the potential goes like $1/r$. The Schrodinger equation for the relative motion of the e-h is

$$\left(-\frac{\hbar^2}{2\mu}\nabla_r^2 - \frac{e^2}{\epsilon r}\right)\psi_\lambda(r) = \epsilon_\lambda \psi_\lambda(r) \tag{1.20}$$

This is the equation of the hydrogen atom type and has a discrete set of eigenvalues

$$\epsilon_{nlm} = -\frac{E_e^b x}{n^2} \quad (n = 1, 2, \dots) \tag{1.21}$$

plus a continuum spectrum of unbounded states. Hence, bound excitons lead to discrete absorption peaks below the band gap. Moreover, it is possible to obtain the values for the electron hole binding energy and the effective Bohr radius in the *1s* state using the values of the H atom

$$E_{ex}^b = Ry = \frac{\mu e^4}{2\epsilon^2\hbar^2} = \frac{e^2}{2\epsilon a_B} = \frac{1}{\epsilon^2}\left(\frac{\mu}{m_0}\right) R_H, \tag{1.22}$$

$$a_B = \frac{\epsilon\hbar^2}{\mu e^2} = \epsilon\left(\frac{m_0}{\mu}\right) a_H, \tag{1.23}$$

where m_0 is the mass of one electron and a_B is the effective Bohr radius. The excitation energy is therefore given by

$$E_{\lambda,K} = e_g(K) + \epsilon_\lambda \tag{1.24}$$

The discrete state $\lambda = (n, l, m)$ represent the bound pair of electron and hole which is called an exciton. In particular this situation is realized in small bandgap (large ϵ) semiconductors and these excitons are called Wannier-Mott excitons.

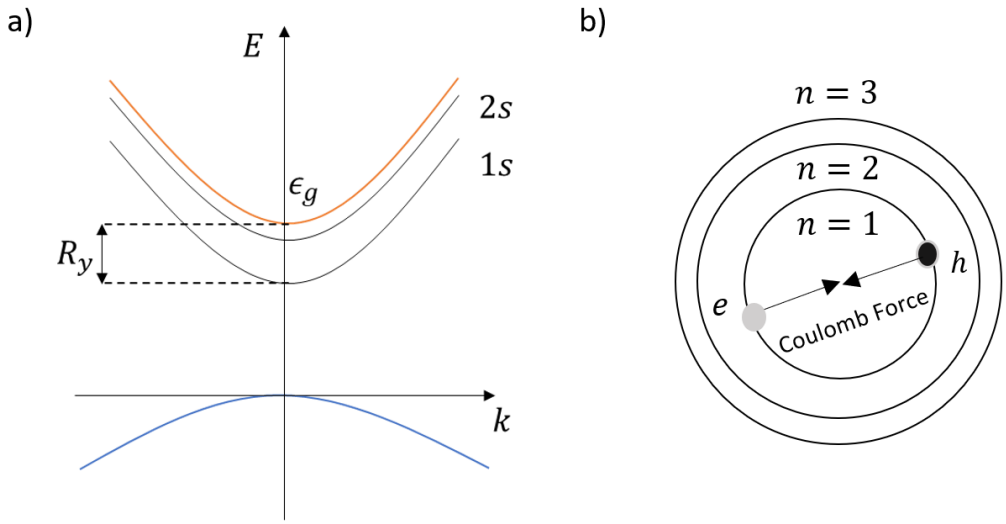

Figure 1.6: *a) Excitation energy of an electron hole pair in a bulk semiconductor as a function of the translational wave vector k. The conduction band (orange) and the valence band (lite blue) are highlighted. The quantity R_y corresponds to the binding energy of the 1s state of the exciton. b) Simplified diagram of a free electron hole pair generated upon optical excitation that is attracted by Coulomb force. The arrows indicate the hydrogenic "Bohr" radius.*

As it is possible to see in figure (1.6 a)) the electron hole pair possesses a series of discrete energetic levels. The highlighted quantity R_y corresponds to the binding energy E^b_{ex} i.e. the energy released upon exciton formation or the energy required for exciton breakup. Note that the exciton is free to move through the crystal and it is not bounded to a specific atom.

We now want to determine the optical absorption spectra that, as previously stated, is dictated by the excitons themselves. The response of a material to an incoming radiation is described by the complex dielectric function $\epsilon(\omega, q) = \epsilon_1(\omega, q) + i\epsilon_2(\omega, q)$. This can be calculated[10] by means of the time dependent perturbation theory and using the Kramers-Kronig relations. The result is an hydrogenic series of discrete lines and a continuum spectrum. The spectral density of the discrete lines reaches the step value for $n \to \infty$. This is the low energy edge of the continuum.

[10]For the sake of simplicity in this paragraph is presented just the result and its physical importance. The complete derivation of the optical absorption spectra can be found in different books as, for example, [**21**].

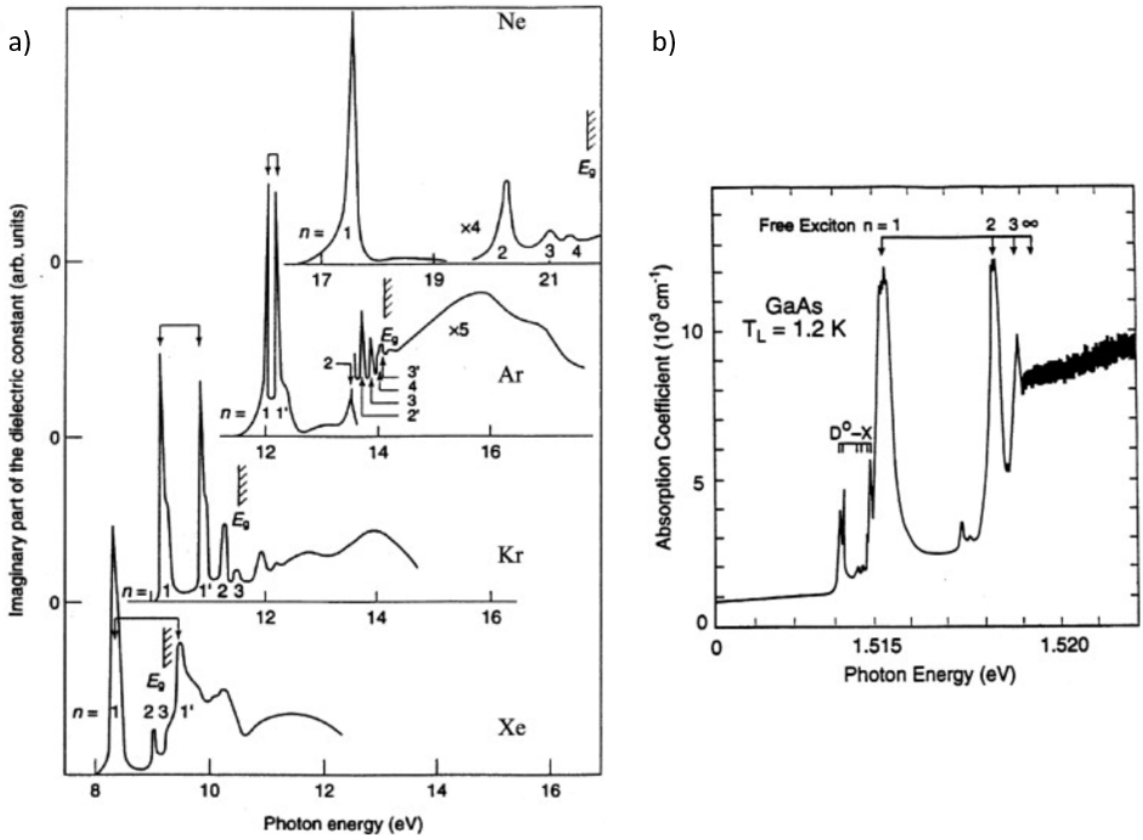

Figure 1.7: *a) Imaginary part of the dielectric function of rare gas solids, the sharp peaks represent the excitonic peaks. b) Absorption spectrum of GaAs at cryogenic temperatures. Here it is possible to notice how exciton binding energies changes depending on the material. As an example in Ne, a large gap insulator, the exciton binding energy is about 4 eV while in GaAs is few meV.* From G. Zimmerer, in *Excited-State Spectroscopy in Solids*, Proc. Intern. School of Physics "Enrico Fermi", edited by U. M. Grassano and N. Terzi (North-Holland, Amsterdam, 1987) and R. G. Ulbrich and C. Weisbuch, unpublished; C. Weisbuch, Thesis, Université Paris VII, 1977.

What has just been described can be visualized in figure (1.7) where the imaginary part of the susceptibility and the absorbance spectra are presented. In the picture is possible to distinguish both the sharp excitonic peaks and the continuum occurring in the presence of the optical bandgap of the material.

The Wannier-Mott excitons have been described. Nevertheless, for strong values of the Coulomb attraction between the electron and hole pair, one obtains a Frenkel exciton. This happens in insulators where the dielectric constant is small [**21**].

1.2.2 Excitons in 2D semiconductors

Now the case of 2D material will be considered[11]. The change of dimensionality bring with himself a change in the effective Hamiltonian with respect to the hydrogenic series used in the 3D case. This is because now the screened interaction in the Hamiltonian itself is not simply $1/\epsilon r$. Anyway, by means of an effective dielectric constant in case of 2D materials it is possible to recover a 2D Hydrogenic model as stated in [**23**]. To obtain the 2D excitons model we assume our system as composed by an electron hole pair in a thin quantum well [12]. This situation is characterized by the Hamiltonian (using radial coordinates):

$$H_{eh} = h_e(z_e) + h_h(z_h) + E_g - \frac{d^2}{dr^2} - \frac{1}{r}\frac{d}{dr} - \frac{1}{r^2}\frac{d^2}{d\theta} - \frac{2}{\sqrt{r^2 + (z_e - z_h)^2}} \tag{1.25}$$

Where $h_h(z_h) = -m_h^{-1}d^2/dz_h^2 + V_h(z_h)$ is the Hamiltonian for hole or electron in the quantum well. Due to the strong confinement, if we consider a very thin quantum well the following approximation is valid

$$\frac{2}{\sqrt{r^2 + (z_e - z_h)^2}} \simeq \frac{2}{r} \tag{1.26}$$

As a consequence the exciton wave function can be factorized as the product $\Psi_{exc}(r_e, r_h) = \phi_e(z_e)\phi_h(z_h)\Psi(r)$. The first three terms are the eigenstate of $h_e(z_e)$ and $h_h(z_h)$ and $\Psi(r)$ describes the in-plane relative motion. The in-plane motion is giving a purely 2D Wannier equation given by

$$\left(\tilde{E}_g - \frac{d^2}{dr^2} - \frac{1}{r}\frac{d}{dr} - \frac{1}{r^2}\frac{d^2}{d\theta}\right)\Psi(r) = E\Psi(r) \tag{1.27}$$

Where $\tilde{E}_g = E_g + E_1^e + E_1^h$ is the effective energy gap that considers the lowest energy levels for the z direction where the particles are frozen. The mathematical solution is similar to the one for 3D excitons. The s-type states ($l = 0$) can be written as

$$\Psi_n(r) = \frac{1}{\sqrt{\pi}(n + 1/2)^{3/2}L_n(2r/(n + 1/2))e^{-r/(n+1/2)}} \tag{1.28}$$

$$E_n = E_g - \frac{R_y^*}{\left(n + \frac{1}{2}\right)^2} \tag{1.29}$$

With $n = 0, 1, 2\ldots$ and L_n^m associated Laguerre polynomial. The direct manifestation of the increased electron hole overlap induced by confinement can be seen in the in the energy of the lowest exciton that is now (for $n = 0$) equal to $4R_y^*$ instead of R_y^*. The continuum states too are similar to the one found in case of 3D (bulk) excitons. It is possible, analogously to what has been done in the previous subsection, to calculate the optical susceptibility and therefore the optical absorption for a 2D semiconductor using

[11] The derivation of this model for excitons in 2D materials is taken from [**22**]

[12] It is assumed that light is polarized along the quantum well plane so that the motion perpendicular to the plane (z direction) is not excited.

the so called 2D Elliot formula[**22**]. The states that can be accessed experimentally are the s states that, in spite of p states with angular momentum different from zero, are predicted to be dipole allowed. An ideal absorption spectra of a 2D material can be seen in figure (1.8): here it is clear how excitons lead to a reorganization of the spectra. First of all, huge excitonic resonances appear below the bandgap at energies given by (1.29) but also the continuum part of the spectrum is changed: "the Coulomb interaction leads to the enhancement of the continuum absorption in the energy range" [**24**].

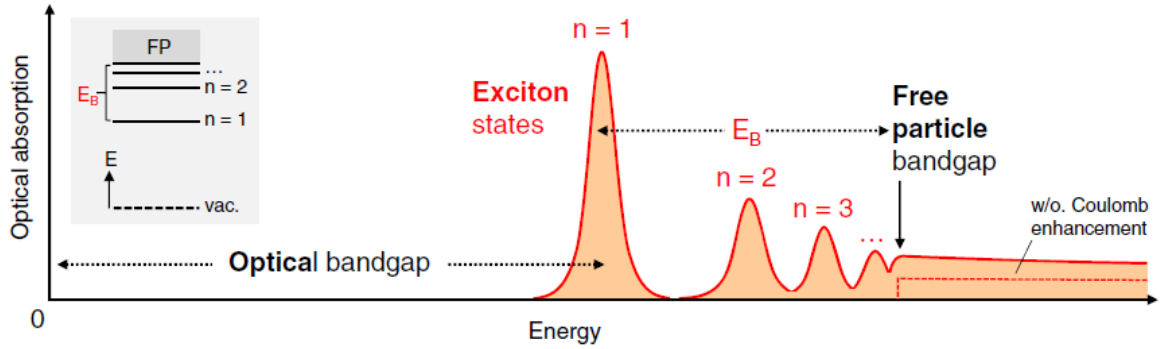

Figure 1.8: *Here is illustrated the optical absorption of an ideal 2D semiconductor. Coulomb interaction increases the continuum level above the free particle bandgap. The inset shows the atom-like energy level scheme of the exciton states where the ground state ($n = 1$) is denoted by E_B.* From [**24**]

This result gives us a mathematical expression for the energy levels of excitonic series in the shape of Rydberg series similar to 3D case. Nevertheless, in this model the environment of the thin material is not taken into account the 2D layer is considered to be an isolated free-standing layer. As one can imagine, in real applications monolayer TMDs are often embedded in a van der Waals heterostructure and the approximation of an uniform environment is no longer valid. The nonlocal nature of the effective dielectric screening, leads indeed to deviation from the model described above as experimentally observed in monolayers WS_2 in [**25**] and $MoSe_2$ in [**26**].

1.2.3 Dielectric screening and environment

An expression for the dielectric constant of a 2D material is difficult to be found. While in a bulk material the macroscopic dielectric constant is defined as the limit $\epsilon(k, \omega)$ as $k \to 0$, for a 2D material this definition cannot be used since $\epsilon_{2D}(k = 0, \omega) = 1$[**23**]. That means a more elaborate treatment is required. As is stated above, excitonic properties in 2D materials differ from the ones in the bulk. It was both theoretically and experimentally confirmed that the reduced screening characteristic of 2D TMDs has two implications: an increased bandgap in the monolayer (see figure 1.9 b)) and a larger exciton binding energy. This can be visualized by means of figure (1.9 a)) where the electric field lines of the electron hole dipole are extending outside the sample. This produces a strong Coulomb interaction (image charge effect) so that the screening is determined by the surrounding environment for the extent of few nm. The interaction between the

electron hole pair is therefore influenced by the dielectric environment and this can be measured by the distance between the charges (Bohr radius): the manifestation of that can be seen both in changes in the bandgap and in the excitonic peak position.

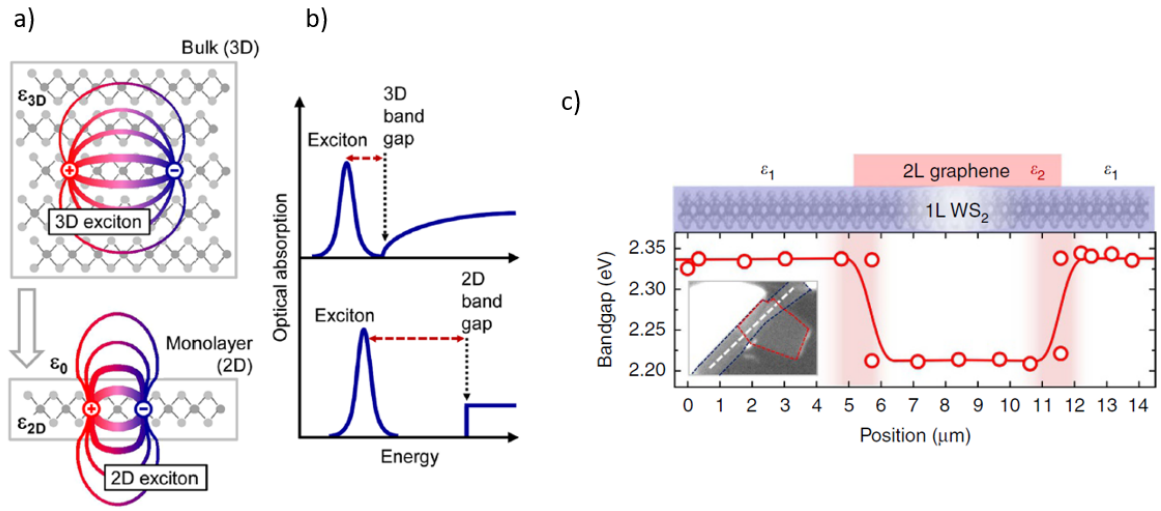

Figure 1.9: *a) Real-space representation of electrons and holes bound into excitons for the three-dimensional bulk and a quasi-two-dimensional monolayer. The different dielectric environment are indicated by the two different constants ϵ_{3D} and ϵ_{2D}. b) Influence of the dimensionality on the electronic and excitonic properties presented by the optical absorption. The transition from 3D to 2D is expected to lead to an increase of the band gap and the binding energy of excitons. c) Demonstration of the influence of the dielectric environment on the optical properties of a thin film. Here the bandgap has been spatially modulated by the presence of a graphene sheet on top of the heterostructure.* From [**25**] and [**27**].

The complexity of the situation described above is relevant but looks at the same time promising. A good understanding and description of the effect of the environment on the optical and electronic properties of monolayer TMDs might be useful in the so called "Coulomb engineering" of bandgap and excitonic processes. Indeed, both the optical bandgap and the exciton binding energies are expected to be tunable by local changes in the dielectric environment. The experimental work described in [**27**] shows the possibility of tuning the electronic bandgap and the exciton binding energy in monolayers of WS_2 and WSe_2 by hundreds of meV by using different heterostructures made by graphene and hBN. In figure (1.9) c), taken from [**27**], it is possible to visualize how a spatially dependent bandgap can be created leading to the first step in the creation of novel lateral junctions with a resolution down to the nanoscale.

As we have already stated, the 2D excitons transition energies are predicted at

$$E_{ex} = E_g - \frac{\mu e^4}{2\hbar^2 \epsilon^2 (n - 1/2)^2} \tag{1.30}$$

where $n = 1, 2, 3\ldots$, $\mu = (m_e^{-1} + m_h^{-1})^{-1}$ is the exciton reduced mass. Nevertheless, in [**25**] an agreement of the experimental data with this Rydberg series is obtained only

for the states $n = 3 - 5$ while the 1s and 2s deviates from this model. This deviation in the scaling can be observed in figure (1.10 a)) .

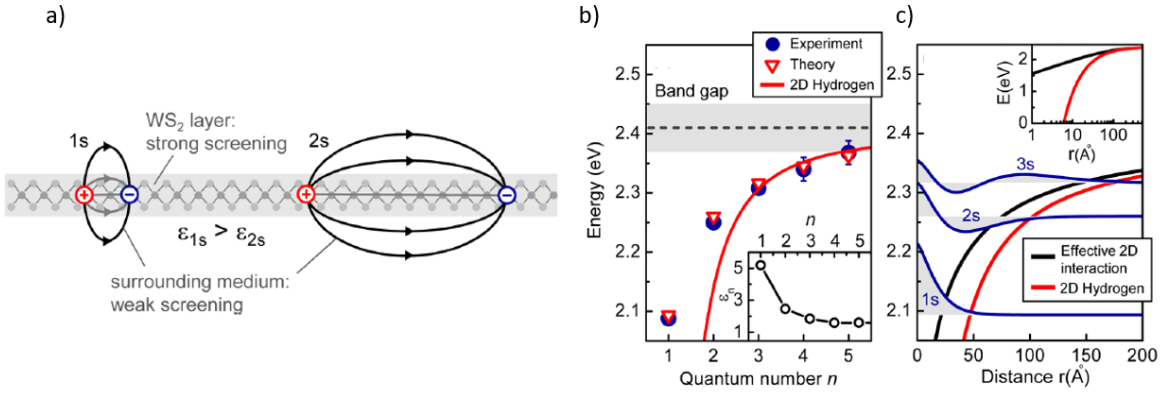

Figure 1.10: *a) Representation of electron-hole pairs forming 1s and 2s excitonic states in a nonuniform dielectric environment. b) Experimentally and theoretically obtained transition energies for the excited exciton states as a function of the quantum number n. For comparison, the fit of the $n = 3, 4, 5$ data to the 2D hydrogen model for Wannier excitons is shown. In the inset are shown the corresponding effective dielectric constants. c) Screened 2D interaction, eq. (1.31), used in the model Hamiltonian (black lines) is compared to the 2D hydrogen interaction scaling as $1/r$ (red lines) (semilogaritmic plot in the inset). The corresponding energy levels and radial wave functions up to $n = 3$ are plotted too.* From **[25]**.

As can be seen in this figure, the field lines of the electron hole dipole for excited state (with larger Bohr radius) extend for a larger portion in the surrounding medium and therefore are less screened. This explains the agreement of the hydrogenic 2D model for higher excited states that can be seen in figure (1.10 b)) by comparing the red line with the experimental points. One way to quantitatively account for this behavior is to modify the effective mass Hamiltonian presented in equation (1.20) using a nonlocally screened electron hole interaction described by the potential [13]

$$V_{eh}(r) = -\frac{e^2}{8\epsilon_0 r_0}\left[H_0\left(\frac{kr}{r_0}\right) - Y_0\left(\frac{kr}{r_0}\right)\right] \tag{1.31}$$

where H_0 and Y_0 are the Struve and Bessel functions, r is the electron-hole distance, r_0 is an effective screening length of monolayer and k is the effective static dielectric constant of the heterostructure. This describes the interaction of two charges in a 2D dielectric resulting in a $1/r$ coulomb interaction at large distances and a weaker $log(r)$ interaction at short separation. The effectiveness of this description can be observed in figure (1.10 c)) by looking at the black solid line.

[13] For a complete description of screening in 2D materials see *Dielectric screening in two-dimensional insulators: Implications for excitonic and impurity states in graphene.* P. Cudazzo et al. PHYSICAL REVIEW B 84, 085406 (2011).

This paragraph has presented and introduction to the phenomenon of non-uniform dielectric screening effects on excitonic properties of thin TMDs. Here the strength of the Coulomb forces is particularly large and is thus not only of fundamental importance, but also allows the tunability of electronic bandgap and excitons binding energy. The possibility of engineering the properties on these materials requires a good understanding of the relationship among the electron-hole pair, the monolayer and the surrounding material. Different corrections to the 2D hydrogen model can be included for this purpose.

1.2.4 The non-locally screened potential

As stated above, the simplest and most common model for excitonic interaction is the hydrogen model that uses the effective Hamiltonian

$$H = -\frac{\hbar^2 \nabla_r^2}{2\mu} + V_{eh}(r) \tag{1.32}$$

where the $V_{eh}(r) = -\frac{e^2}{\epsilon r}$ is a locally screened attractive electron hole potential, ϵ is the dielectric constant of the 2D material. This gives the result of equation 1.30 for the energy ladder, physically corrected description for a monolayer suspended in a medium with $\epsilon = 1$. Nevertheless, in a physically consistent system, the screening experienced by the Rydberg states is expected to be dependent on the quantum number n [**25**]. This is why the nonuniform screening of the environment is usually taken into account using as interaction potential, the Keldysh potential [**18**].

-	MoS_2	$MoSe_2$	WS_2	WSe_2	hBN
$1L$	6.4	7.4	6.3	7.5	3.29
$2L$	6.8	7.8	6.5	7.7	3.44
$Bulk$	7.2	8.3	6.6	7.8	3.76

Table 1.2: *Out-of-plane dielectric constant for different number of layers and for different materials. The values reported correspond to the static dielectric constant, which includes both the electronic and the ionic response.* From [**28**].

Let us consider a van der Waals heterostructure, made for example by a monolayer (two-dimensional) semiconductor embedded in a 3D medium, for example hBN with lower dielectric constant[14]. In this system, even if the electrons and holes are confined in the plane, the electric field lines between them extends in the surrounding medium. The portion of electric field outside the monolayer increases with the increasing separation between the charges leading to a weaker total screening. This nonlocal screening indicates a deviation from the previously considered Coulomb's law. In this context, the interaction between charges can be approximated by [**29**]

$$V_{eh}(r) = -\frac{e^2}{8\epsilon_0 r_0}\left[H_0\left(\frac{kr}{r_0}\right) - Y_0\left(\frac{kr}{r_0}\right)\right] \tag{1.33}$$

[14]The values of the dielectric constant are presented in table 1.2 and taken form [**28**].

which is the Keldysh potential, already presented in equation 1.31. Where, usually, k and r_0 are free parameters. This effective potential will be used in this report, for the data analysis of the absorption of 2D TMDs using differential reflectivity.

-	MoS_2	$MoSe_2$	WS_2	WSe_2
$\mu(m_0)$	0.25	0.27	0.16	0.17
$m_c^k(m_0)$	0.51	0.64	0.31	0.39
$m_v^k(m_0)$	0.58	0.71	0.42	0.51

Table 1.3: *Effective masses of excitons and particles in the conduction (c) and valence (v) bands of some TMDs monolayers. The effective masses are considered at the K point of the first Brillouin zone and are expressed in units of the free electron mass m_0. These results have been obtained using DFT calculations.* From [**30**] and [**31**].

We consider the band structure of the monolayers TMDs, it can be assumed parabolic around the *K(-K)* points of the first Brillouin zone and the effective masses can be calculated by density functional theory (DFT) and are reported in table 1.3. Using the quasi-2D potential in equation 1.33, the Hamiltonian for the electron hole relative motion can be written as

$$H = -\frac{\hbar^2 \nabla_r^2}{2\mu} - \frac{e^2}{8\epsilon_0 r_0}\left[H_0\left(\frac{kr}{r_0}\right) - Y_0\left(\frac{kr}{r_0}\right)\right] \tag{1.34}$$

The eigenvalues for this problem of the low lying s-states can be expressed in the exponential form[**18**]

$$f_n(r) = C_n e^{-\alpha_n r} \tag{1.35}$$

where $\alpha_n = \alpha g^n$, $C_n = 2\alpha_n/\sqrt{2\pi}$, $n = 0, ..N-1$ and the problem can be solved using variational procedure to find α and g and orthogonalized using the Gram-Schmid method. After the diagonalization, lowest lying eigenstates can be found and compared with the exact values of 1.30 and with the experimental results obtained for the excitonic peaks.

The necessity of the described approach, and the employment of the Keldysh potential, can be justified by the non-hydrogenic physics of the low lying excitons states as reported for WS_2 monolayer in [**25**]. One possibility to verify this is to use in the 2D Hydrogenic model an effective dielectric constant that accounts for the environment being in particular n-dependent, where n is the quantum number. From equation 1.30 one can invert the relation to determine the dielectric constant ϵ_n required to reproduce the experimental binding energy of the nth exciton

$$\epsilon_n = \left[2\hbar^2 E_{b,exp}^{(n)} \frac{(n-1/2)^2}{\mu e^4}\right]^{-1/2}. \tag{1.36}$$

Two possibilities can manifest themselves. If the function ϵ_n results to be a constant, the 2D hydrogenic model, that assumes a locally screened electron-hole interaction, can be assumed as valid. On the other hand, if ϵ_n shows a dependence on the quantum

number n, one can conclude that, due to the increase of the exciton radius with n, the screening in non-uniform. If the dielectric constant decreases with n, a correspondent decrease in the screening of the electron-hole interaction can be inferred and this can justify a deviation from the 2D hydrogenic model.

1.3 Applications of excitons in TMDs and tunability

Excitons in 2D semiconductor have several technological applications in optoelectronics and photonics. Different photonic devices based on excitons in thin TMDs have been realized [**5**] in the last years. This was possible due to the ability to control the desired parameters, a fundamental requirement for all kind of devices. One has indeed different ways to manipulate the excitonic emission in a 2D semiconductor due to the reduced dimensionality. As will be described in this section, excitons result to be tunable using an external magnetic or electric field or applying strain to the TMDs. The dependence of the optical properties with respect to the environment, is a remarkable feature of these novel materials.

1.3.1 Electrical tuning

The first possibility that one has to tune excitons is the application of a bias to the 2D material. This can be done using field effect to dope electrostatically the carriers in the semiconductor. In [**32**] the application of a voltage to a MoS_2 monolayer transistor has been observed to change the absorption spectra of the TMDs (figure 1.11 a)). The peaks that can be observed in this picture correspond to the A and B excitons and their intensity changes if the electron population is changing itself.

Further studies[**33**] have demonstrated how a bias can continuously tune the exciton binding energy of a monolayer WS_2. In this paper, by injecting a free carrier density of $8 \times 10^{12} cm^{-2}$ a decrease in the exciton binding energy of $100meV$ was observed. The ionization of exciton might be possible at higher carrier densities.

All these experimental observations are caused by the increased many-body screening of the Coulomb interaction, dependent on the carrier density. This effect is particularly strong and remarkable in 2D materials due to the enhanced Coulomb interaction and strong confinement. The electric field indeed was not found to significantly modulate the dielectric function of the thin TMDs, thus the excitons dependence on the carrier density can lead to optoelectronic application in the 2D limit.

1.3.2 Magnetic tuning

As previously stated in this report, monolayer TMDs have energetically degenerate excitons in the valleys K, K', accessed with circular dichroism. A further degree of freedom to control exciton energies is given by the application of a magnetic field using the Zeeman effect for spintronic applications.

The Zeeman shift, due to spin magnetic moment, does not affect optical resonances[15] but a significant contribution comes from the atomic orbital. The conduction band, composed by electrons on d_z^2 orbitals with $m = 0$, do not change under magnetic field. The valence band on the other hand, made by electrons in d orbital with $m = -2$ and p orbitals with $m = -1$ [16], shifts[**34**]. This therefore causes an excitonic shift of around $\simeq 0.1meV/T$ as is shown using polarization resolved magneto PL in figure 1.11 b). In

[15] In optical transitions indeed spin is conserved [**5**].

[16] This is valid for the K valley, opposite sign for K'.

the experimental results of chapter 3 of this report, the linear shift of neutral exciton in WSe_2 and $MoSe_2$ is reported in presence of strong magnetic field. This shows the lifting of the valley degeneracy and the tunability of excitons under external magnetic field.

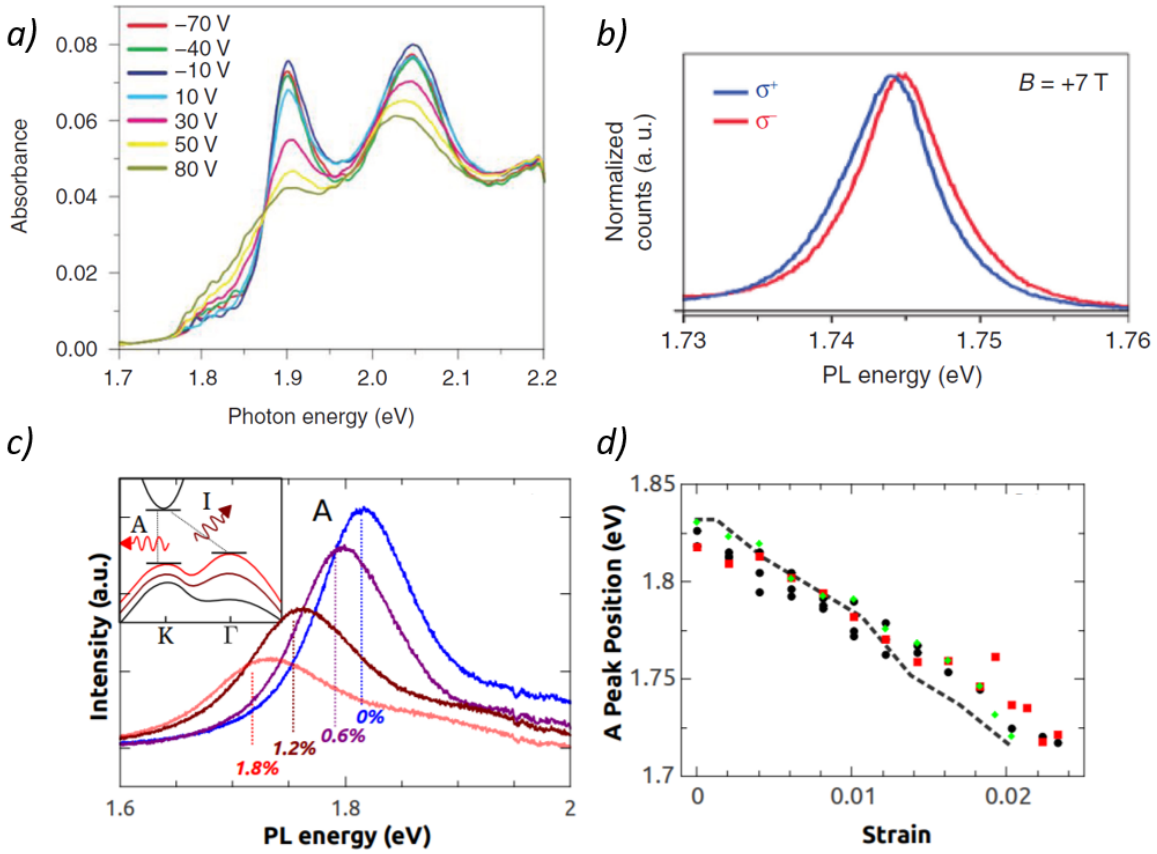

Figure 1.11: *a) Monolayer MoS2 absorption spectra at different back-gate voltages in a field effect transistor device. The global absorption with significant A exciton and B exciton shows amplitude variation, peak shift, and linewidth change under different gate bias voltages.* From [**32**]. *b) Valley exciton PL with a magnetic field applied. K and -K valley energy degeneracy lifts in the presence of a magnetic field, the two spin populations can be accessed with circularly polarized light (blue and red curves respectively).* From [**34**]. *c) PL spectra of a representative monolayer device as it is strained from 0 to 1.8%. d)Evolution of the position of the A peak of the PL spectrum with strain. Inset in c) contains schematic representations of the band structure for monolayer MoS2 devices that are progressively strained from 0% (black) to 5% (maroon) and 8% (red).* From [**35**].

1.3.3 Mechanical tuning

Among others, 2D materials possess the distinctive advantage of mechanical flexibility. If a mechanical strain is applied to a crystal, the lattice structure is expected to change as well. In TMDs the electronic band structure is linked to the lattice constant

which is expected eventually to change under applied strain. That means, also inter-band optical transitions are expected to change. In the work of [**35**] it is demonstrated that the electronic structure of MoS_2 monolayer can be modified under axial tensile strain. This results in a modification of the exciton photoluminescence spectrum as can be seen in figure 1.11 c). The tunability of the direct band-gap transition is of $70meV$ per % strain and has a linear response of peak position vs. strain.

An interesting fact is that the response to strain is different for particle with different effective masses. This leads to the transformation of the band structure that changes from direct to indirect as can be seen by the inset of figure 1.11 c). This causes a drop in the photoluminescence intensity. To summarize, the change in the lattice constant, modifies multiple aspects as the band structure, phonon spectrum and excitons exchange interaction [**5**]: the complexity of this phenomena is still under investigation of great interest.

1.3.4 Photonic devices based on 2D excitons

As a conclusion for this first chapter, some devices exploiting 2D excitons will be introduced. This done to draw the framework where the fundamental research of this report is embedded in and to present future perspectives and possible application of excitons in science and technology.

It is known that 2D materials are suitable for optoelectronic and photonic applications due to their efficient light-matter interaction. First of all, as described above, the 2D nature of TMDs make excitons tunable and controllable using different parameters. The possibility of realizing van der Waals heterostructures allows the fabrication of an infinite number of devices whose properties can be engineered by means of monolayer environment. Moreover, many TMDs semiconductors have direct bandgap resulting in strong absorption/emission of light.

The first device reviewed is an *Excitonic light emitting diode* (LED), where light emission is due to the recombination of electrons and holes injected in a p-n junction. These light sources have a wide range of utilization especially for their efficiency and fast switching. That is why a straightforward application of direct bandgap 2D materials is the development of bright and ultra-thin LEDs.

In the work of [**36**] $MoSe_2$ has been embedded in a device with metal contacts for doping (carrier injection) and multiple electrical gates. The scheme of this device can be seen in figure (1.12 a)) along with the exciton dominant electroluminescence (EL) in the junction. The monolayer can be tuned using gates in order to make one side p-doped and one side n-doped. The efficient injection of electrons and holes is provided by the in-plane junction. It is also possible, in this case, to tune the emission using the injection current bias. This is an example of a fully 2D LED. Moreover, the control of the valley polarization in TMDs using light, can be exploited by the fabrication of a chiral LED emitting σ^+ circularly polarized light under forward bias and σ^- in the reverse. Electrical generation of valley carriers can be used for manipulation and detection of valley polarization in the development of valleytronics.

Another interesting result obtained in the realization of exciton-based devices is the integration of the TMD with a photonic crystal cavity. This naturally arises by the

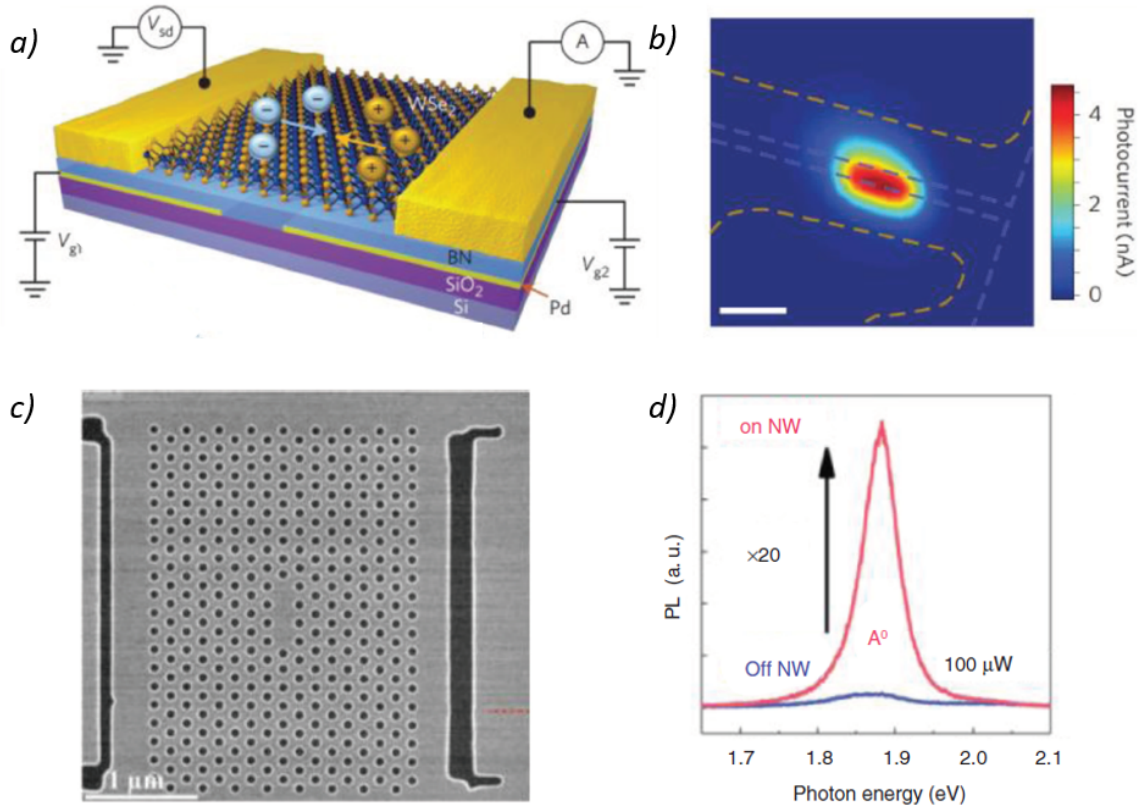

Figure 1.12: *a) Schematic of a monolayer WSe_2 LED based on p-n junction. Two back gates can separately tune the doping level at the two regions. Under a source drain voltage the carriers recombine producing electroluminescence. b) Photocurrent of the LED mainly generated in the junction. Excitons can be enhanced using Purcell effect, this is done using a photonic crystal as the one displayed in c). If the polarization condition in the cavity is respected, an enhancement in the photon emission can be seen d).*From [**36**] and [**37**].

atomic thickness of 2D semiconductors that allows embedding in photonic structures like the one shown in figure (1.12). When a photon emitter is coupled to a cavity, in weak coupling regime, the so-called Purcell effect [17] influences the exciton decay rate increasing the emission consequently[**38**]. In particular are affected the PL intensity and the valley polarization [**5**].

In the work of [**37**] a photonic crystal cavity was designed with a resonance matching the 1s exciton resonance in MoS_2 exfoliated and transfer onto the cavity. An enhancement in this case of almost 5 times with respect to the sample has been observed in the PL emission. The Purcell factor of the cavity was deduced to be over 70. It is also possible to fabricate electrical contacts and gates on 2D photonic crystals. This allows to electrically manipulate the coupling between the cavity and the exciton emitter in the

[17] The Purcell factor is the enhancement of a quantum system's spontaneous emission rate caused by its environment. It can be written as $F_p = \frac{2}{4\pi^2}\left(\frac{\lambda}{n}\right)^3\left(\frac{Q}{V}\right)$, where n is the refractive index, Q and V are the cavity quality factor and mode volume.

2D TMD.

To conclude, excitons in 2D materials offer the opportunity to explore a novel physics and allow diverse photonic application of TMDs. First of all, confinement enhances coulomb effects and reduces the screening, this is why excitons have such strong effects in 2D limit. Their binding energy is therefore hundreds of meV allowing their investigation even at room temperature. The possibility of having tunable parameters, inspires the development of functional optoelectronic and photonic devices such as LEDs, and lasers based on 2D semiconductor. At last, the assembly of 2D van der Waals heterostructures opens the gates to the exploration of exciton physics and application by means of dielectric engineering of the environment.

Chapter 2

Experimental techniques

In this section the experimental techniques used in this research project, will be introduced and described. I will not just present the working principle, the potential application and advantages of each technique but I will also explain why and how I have used them for the research project itself. The techniques employed in this work were two: imaging spectroscopic ellipsometry and confocal microscopy. Imaging spectroscopic ellipsometry is a technique that exploits polarized light to obtain information about the sample such as thickness and dielectric function. It is used in thin film analysis due to its ability to effectively characterize a van der Waals heterostructure. Confocal microscopy, known for its improved resolution with respect with a standard microscope, allows the reduction of the focal volume in the sample. The setup has been adapted to perform broadband reflectivity: in this way one can investigate optical properties of the sample with good spatial and spectral resolution (the latter imposed by the spectrometer). Moreover the setup of the confocal microscope allows us to perform a measurement at temperature around 4 K by placing the sample in a cryostat. By lowering the temperature of the sample, one expects to reduce phonos (that can dissociate the electron-hole pair) and to obtain a sharper linewidth of the excitonic transitions. The cryostat used, Attocube Attodry, is equipped with superconducting magnets to investigate the effects of magnetic fields on the 2D heterostructure.

2.1 Ellipsometry

Spectroscopic Ellipsometry is an experimental technique to measure with high sensitivity the thickness of a thin film and its complex refractive index. The typical thickness resolution that can be achieved, depending on the wavelength used and the homogeneity of the material, ranges from 0.1 nm to 100 μm. For layers of few nm thick the resolution is better than 0.01 nm [**39**]. The sensitivity that one can achieve when measuring the refractive index is in the order of $5 * 10^{-}5$: one of the best resolutions in the analysis of thin films. Limitations are present in the number of layers in a layer stack that can be individually characterized. Depending on the contrast of the stacked materials, a measurement of 10 layers is doable. The measurement can be repeated for an arbitrary range of wavelengths in order to obtain a photon energy dependence of the property to be analyzed e.g. the refractive index $n(\lambda)$. This is called spectroscopic ellipsometry.

The main advantages of this technique are related to the optical method used during the experiment. The visible light shined on the sample is non-invasive and non-damaging, the intensity is low indeed and one can directly measure the refractive index even of a sample inside a transparent environment. In an ellipsometer, the transverse electro magnetic (TEM) mode of the light is generated and polarized in a known state. After being shined on the sample it is reflected and, in general, will have a different polarization state and different spectral intensity: the 'ellipse' i.e. the state of polarization is measured in a fixed point and analyzed. Here a scheme of a generic ellipsometer is drawn but will be described into detail later in chapter 2.1.2. Before doing so it is important to present the formalism used when dealing with optical properties of a multilayer structure such as the van der Waals heterostructure investigated in this research project, the so-called transfer matrix method.

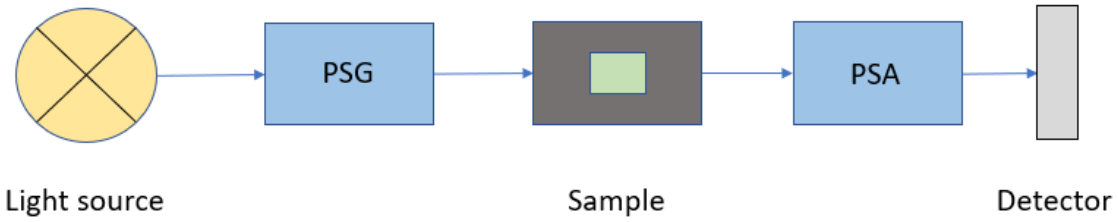

Figure 2.1: *Working principle of ellipsometric techniques. The Polarization State Generator (PSG) and Polarization State Analyzer (PSA) may consist of a polarizer or a combination of a polarizer and retarder.*

2.1.1 Transfer matrix method

The transfer matrix method is a really flexible formalism that can be used to simulate the reflection, transmission and absorption of a planar layered structure making it widely used in the optical characterization of thin films. The derivation presented here is based on the boundary conditions imposed by Maxwell's equations at the interface of two materials with different refractive index. A similar derivation can be found in [**40**]. The layers are supposed to be homogeneous and isotropic with a film thickness of the order of

the wavelength of light. Moreover, we consider TE electromagnetic waves i.e. with the electric field tangent to the layer interface (s-polarization) but an analogue derivation can be performed in the case of TM waves[1].

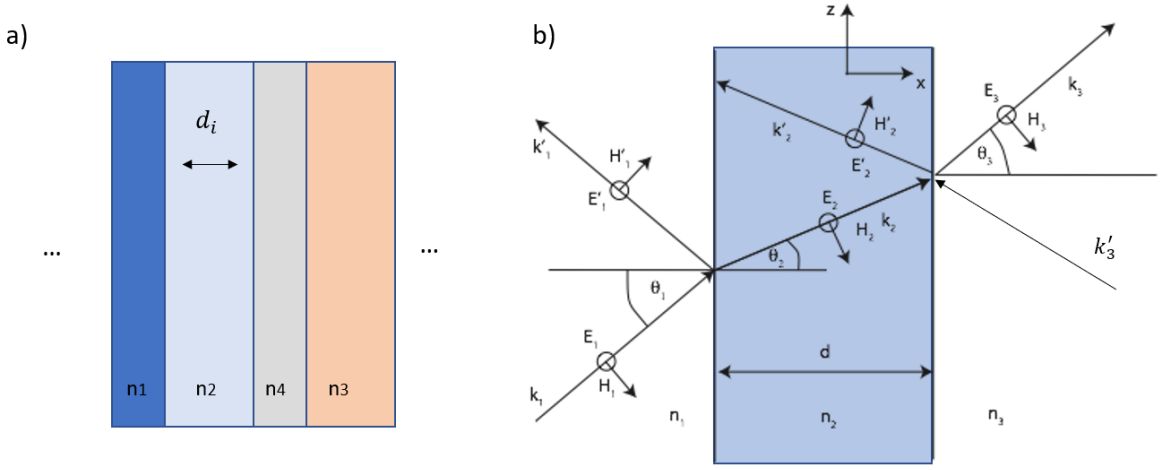

Figure 2.2: *a) Example of a layer stack whose optical properties (transmission, reflection...) can be investigated using the transfer matrix method; b) scheme used during the derivation of the transfer matrix, the wavevector of the forward and backward propagating rays are depicted. This is the case of a TE electromagnetic wave. Note how the symbol ′ (prime) indicates a wavevector or a field propagating in the negative x direction.*

From figure (2.2 b)) consider the first dielectric interface and assume light incident from left, the incidence plane is placed at $x = 0$ and the same wavelength on the two sides is maintained. By considering the complex representation of a wave, the electric field can be written as[2]

$$\mathbf{E} = \begin{cases} (E_1 e^{-ik_1 \cdot r} + E'_1 e^{-ik'_1 \cdot r}) e^{i\omega t}, & \text{if } x < 0 \\ (E_2 e^{-ik_2 \cdot r} + E'_2 e^{-ik'_2 \cdot r}) e^{i\omega t}, & \text{if } x > 0 \end{cases} \tag{2.1}$$

By using the Stokes's theorem into Maxwell's equations involving the curl, and divergence theorem in those involving the divergence, one can derive the boundary conditions for the fields in media with no free charges. The result is that the tangential components of the **E**,**H** fields are continuous across the interface. At $x = 0$ for the electric field

$$E_{1s} e^{-ik_1 z sin\theta_1} + E'_{1s} e^{-ik'_1 z sin\theta'_1} = E_{2s} e^{-ik_2 z sin\theta_2} + E'_{2s} e^{-ik_2 z sin\theta'_2} \tag{2.2}$$

Where $k_i = \omega/(c/n_i)$, due to the law of reflection $\theta_1 = \theta'_1$, $\theta_1 = \theta'_1$ and due to Snell's law $\frac{sin\theta_1}{sin\theta_2} = \frac{n_2}{n_1}$. So the **E** boundary condition becomes:

$$E_{1s} + E'_{1s} = E_{2s} + E'_{2s} \tag{2.3}$$

[1] The ellipsometry analysis depends on both the s- and p-polarization, and the transfer matrix method applies to both the polarization cases.

[2] The symbol ′ (prime) indicates a wavevector or a field propagating in the negative x direction.

Proceeding in the same way for **H** and using the relation $|\mathbf{E}| = \sqrt{\mu/\epsilon}|\mathbf{H}|$ the **H** boundary condition becomes:

$$n_1(E_{1s} - E'_{1s})cos\theta_1 = n_2(E_{2s} - E'_{2s})cos\theta_2 \tag{2.4}$$

Writing (2.3) and (2.4) in a matrix form, the result is:

$$D(1)\begin{pmatrix} E_{1s} \\ E'_{1s} \end{pmatrix} = D(2)\begin{pmatrix} E_{2s} \\ E'_{2s} \end{pmatrix} \tag{2.5}$$

Where $D(i) = \begin{pmatrix} 1 & 1 \\ n_i cos\theta_i & -n_i cos\theta_i \end{pmatrix}$. The quantity $S_{i\to j} = D(i)^{-1}D(j)$ is defined and is the transfer matrix at the boundary of a dielectric i.e. relates the forward and backward propagating electric field on one side and the other of the interface. At this point, it is possible to see the use of the transfer matrix at a boundary between two dielectrics. By taking into account the case of light impinging on the interface from the left only, $E'_{2s} = 0$. The reflection coefficient is:

$$r_s = \begin{pmatrix} E'_{1s} \\ E_{1s} \end{pmatrix}_{x=0} = \frac{S_{1\to 2}|_{21}}{S_{1\to 2}|_{11}} \tag{2.6}$$

The transmission coefficient instead is

$$t_s = \begin{pmatrix} E_{2s} \\ E_{1s} \end{pmatrix}_{x=0} = \frac{1}{S_{1\to 2}|_{11}} \tag{2.7}$$

Therefore amplitudes are related by the so-called Fresnel coefficients:

$$r_s = \frac{n_1 cos\theta_1 - n_2 cos\theta_2}{n_1 cos\theta_1 + n_2 cos\theta_2} \tag{2.8}$$

$$t_s = \frac{2n_1 cos\theta_1}{n_1 cos\theta_1 + n_2 cos\theta_2} \tag{2.9}$$

An analogous derivation can be done for TM waves (or p-polarization) where the magnetic field is polarized transverse to boundary giving the result:

$$r_p = \frac{n_1 cos\theta_2 - n_2 cos\theta_1}{n_1 cos\theta_2 + n_2 cos\theta_1} \tag{2.10}$$

$$t_p = \frac{2n_1 cos\theta_2}{n_1 cos\theta_1 + n_2 cos\theta_1} \tag{2.11}$$

We know how to get relationships between fields at either side of each interface: after crossing a boundary, the light travels the medium and is subject to a phase shift. Considering the fields at $x = 0^+$ and $x = d^-$ the following relation is valid

$$\begin{pmatrix} E_{2s}(0^+) \\ E'_{2s}(0^+) \end{pmatrix} = \begin{pmatrix} e^{ik_2 cos\theta_2 d} & 0 \\ 0 & e^{-ik_2 cos\theta_2 d} \end{pmatrix} \begin{pmatrix} E_{2s}(d^-) \\ E'_{2s}(d^-) \end{pmatrix} \tag{2.12}$$

So in general the matrix relating the electric component of the field before and after the propagation in a layer is $G(d)_i = \begin{pmatrix} e^{i\phi_i} & 0 \\ 0 & e^{-i\phi_i} \end{pmatrix}$ where $\phi_i = 2\pi/\lambda n_i d_i cos\theta_i$ is the phase change in a snapshot of the field at 0 to the field at d, at a constant value of z.

Now the traveling of the light in a layered structure is just a repetition of interfaces and slab of materials, therefore, by considering the case in figure (ref02 a)) the transfer matrix can be obtained by a multiplications of the matrices of refraction/reflection and propagation of all the layers composing the structure from left to right (according to the direction of the incoming light). The result is:

$$\begin{pmatrix} E_{2s}(0^+) \\ E'_{2s}(0^+) \end{pmatrix} = S_{0\to1}G_1S_{1\to2}G_2...G_nS_{n\to0}\begin{pmatrix} E_{2s}(d^-) \\ E'_{2s}(d^-) \end{pmatrix} \tag{2.13}$$

Where n is the number of layers composing the structure and 0 refers to air. We call $T_{0\to n} = S_{0\to1}G_1S_{1\to2}G_2....G_nS_{n\to0}$. Therefore, the propagation of light, even through a complex structure made by different materials, can be described by a simple matrix called 'transfer matrix' in the form

$$T_{0\to n} = \begin{matrix} A(\omega) & B(\omega) \\ C(\omega) & D(\omega) \end{matrix}. \tag{2.14}$$

Equations (2.6) and (2.7) can be used again on the transfer matrix T to obtain the reflection and transmission coefficients in amplitude. To extend this to the case of power, it is sufficient to consider the obliqueness factors which are different for TE and TM polarization.

The result is, for s-polarization:

$$R_s = |r_s|^2 \tag{2.15}$$

$$T_s = Re\left(\frac{n_n cos\theta_n}{n_0 cos\theta_0}\right)|t_s|^2 \tag{2.16}$$

And for p-polarization:

$$R_p = |r_p|^2 \tag{2.17}$$

$$T_p = Re\left(\frac{n_n^* cos\theta_n}{n_0^* cos\theta_0}\right)|t_s|^2 \tag{2.18}$$

2.1.2 Ellipsometry

In this section the working principle and the experimental setup of an ellipsometer will be described. The most general state of polarization of (monochromatic) light is elliptical; in this case a vector field at a fixed point in space draws in time an ellipse perpendicular to the propagation vector. When the light interacts with a sample, in general, it changes its polarization state. Therefore, if the initial polarization state of the light is known, by measuring the outcoming light it is possible to retrieve information about the shined object. The probability of the sample to change the polarization state of a monochromatic radiation can be described by two parameters (figure 2.3) as stated in [**41**]. These are called ellipsometric angles Ψ and Δ.

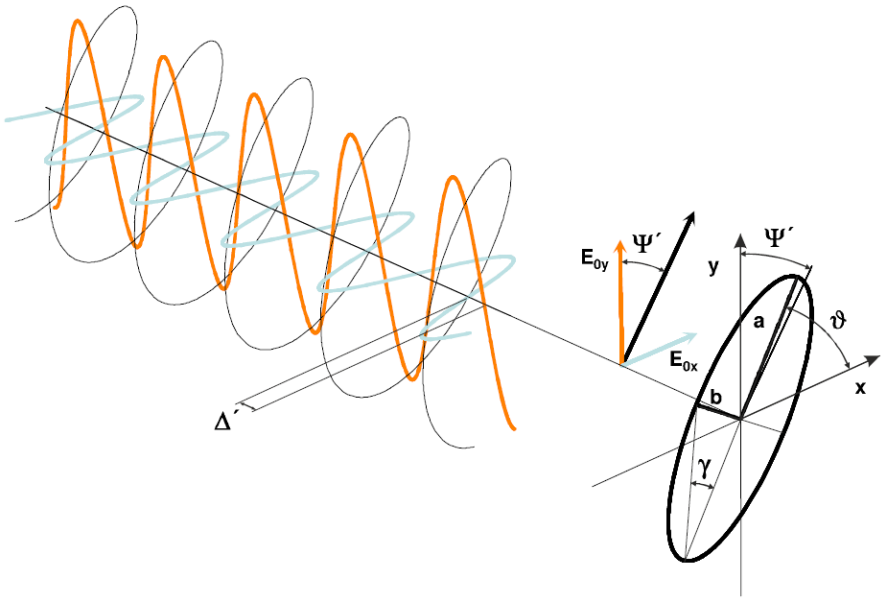

Figure 2.3: *Elliptically polarized light and the projected polarization ellipse. Here a and b are, respectively, the semi-major and semi-minor axes of the ellipse and* Ψ *and* Θ *are the angles that a forms with the x and y axes. Finally,* Δ *is the relative phase difference between the p and s component of the light. Mathematically the polarization state is defined by the parameter* $tan\Psi e^{i\Delta}$. Taken from [**41**]

In order to obtain physical quantities about a planar multilayer sample, one needs to relate the polarization change with the intrinsic sample properties e.g. thickness and dielectric function. The light reflected by an object in the simple case of an abrupt surface of each layer or infinitely thick medium can be quantified by the Fresnel equations presented in the previous section. The reflection coefficients r_s (2.8) and r_p (2.10) for polarizations parallel and perpendicular to the plane of incidence define the ellipsometric angles according to the complex ratio:

$$\frac{r_p}{r_s} = tan\Psi e^{i\Delta} \tag{2.19}$$

The ellipsometer photodetector measures both the ratio of the reflectivity and the relative phase change of the p- and s-components $R_p/R_s = tan\Psi$ and $\Delta = \delta_p - \delta_s$ allowing to estimate the ellipsometric angles. It is worth to mention that, even if the studied sample is a complex optical system with various layers of different materials, e.g. a van der Waals heterostructure, multiple reflections and phase shifts are simulated using the transfer matrix formalism.

To perform this measurement, an ellipsometer uses a monochromatic light source, a Polarization State Generator (PSG), an objective, a Polarization State Analyzer (PSA) in the path between the sample and a photodetector. The PSG changes the polarization state of the incident beam, while the PSA analyses the polarization of the reflected beam. The photodetector is used to image the sample. Different configurations of PSG and PSA can be implemented; in the common case presented in figure 2.4 the PSG is made by a linear polarizer and a retarder ($\lambda/4$ wave plate) while the PSA is composed by a single

linear polarizer. A linear polarizer is a simple device commonly used in optics; it is able to suppress the optical component of the electric field that oscillates perpendicular to its polarization axis while the component parallel to its axis is free to pass. Note that, since we have two linear polarizers in this configuration, if their polarization axes are at 90° one with respect to the other, the transmitted light is suppressed (with a reduction of 10^{-6}). Retarders instead are used to introduce a phase delay between the two perpendicular components of the incident electric field. The one used here is a "quarter wave plate". It has a faster and slower axis leading to a phase shift of 90° in the components of the electric field along these axes. Note that using a linear polarizer and a retarder it is possible to obtain any elliptically polarized state. By considering the configuration mentioned just above, the measurement of the ellipsometric angles Ψ, Δ is done by rotating the angles of polarization optics placed in the beam path.

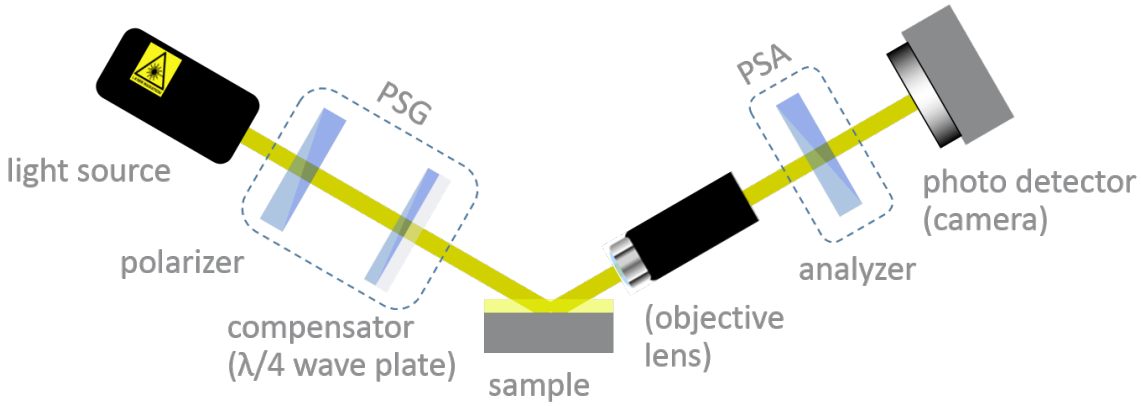

Figure 2.4: *A scheme of the most common configuration for an ellipsometer (PSG - PSA) adopted by the Accurion EP4 used in our measurements. By following the light path one can see a polarizer, a compensator, the sample, a second polarizer and the photodetector. This configuration is used in nulling ellipsometry.*From *accurion.com/ellipsometry.*

The ellipsometer used in the experiments presented in this report is the "Accurion EP4" from Accurion GmbH. This state-of-the-art instrument bases the measurement on the principle of nulling ellipsometry, i.e. finding the right-angle settings for Polarizer, Compensator and Analyzer in order to minimize the intensity on the photodetector. This is equivalent to finding a minimum on the signal on the photodetector. This minimum can be found because a properly elliptically polarized beam (generated by the pair Polarizer and Retarder), when reflected by the sample, becomes linearly polarized. Using the Analyzer it is possible to know the polarization direction of the reflected beam, indeed using a second polarizer at 90° from the polarization axis the light beam is (almost) extinguished.

The procedure described above is iterative, and is performed until the minimum of intensity is found with the accuracy desired before the measurement. First the light passes through the PC couple and the P, C angles are changed in such a way that the reflected light is linearly polarized. Then a photodetector is used behind the analyzer A to detect this as a minimum of the signal. The main advantage of this method is the fact that one is measuring angles instead of light flux on a photodiode so non

idealities from the lamp and non-linearities of the detector are avoided leading to a more accurate measurement [**42**]. Up to now, a monochromatic excitation power has been considered. By repeating the previous measurement for different wavelengths, it is possible to determine the spectral dependence of the ellipsometric angles delta and psi (the so called spectroscopic ellipsometry).

After the ellipsometer provides the ellipsometric angles spectra, one needs to relate them to the physical quantities to be measured i.e. the characteristics of the sample. Suppose to have a sample composed by a substrate, a layer of known material and thickness and a second layer on top made by a material whose dielectric function needs to be investigated figure (2.5 a)) . The measured Δ and Ψ values will depend on the layer thickness d and of its refractive index n, as previously discussed in Section 2.1.1. Therefore a particular structure will produce a specific curve of the ellipsometric angles and vice versa, a particular curve is the fingerprint of the sample the light was reflected from. In general (except for trivial cases) it is difficult to analytically calculate the refractive index or the thickness from the ellipsometric angles just because the functional form is too complicated. That is why one has to develop an optical model. This is a mathematical expression of Ψ, Δ as a function of the parameters.

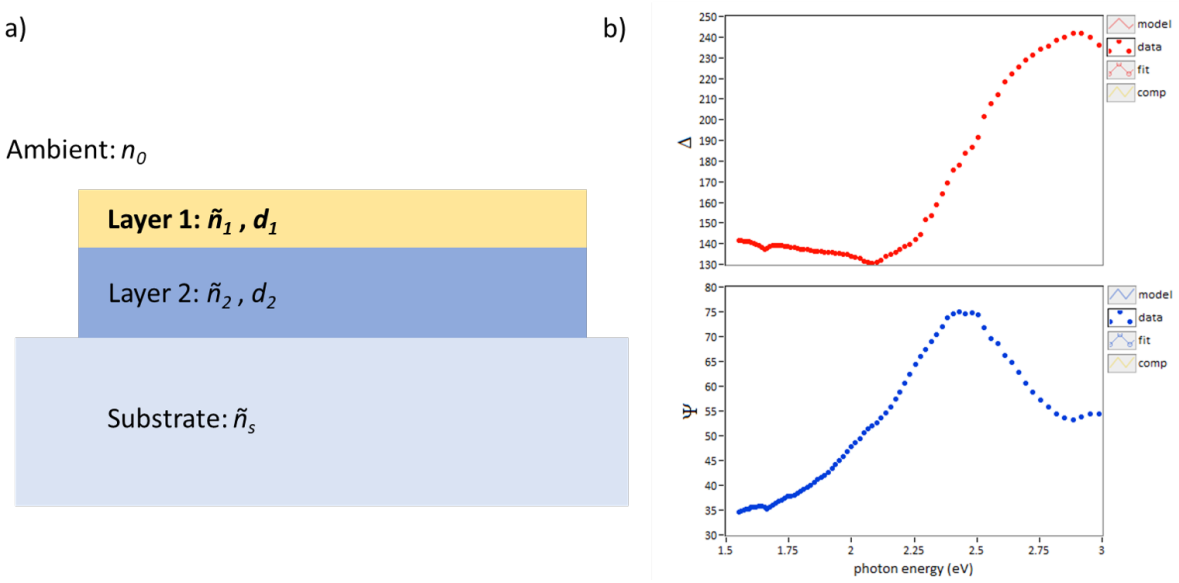

Figure 2.5: *a) A typical heterostructure that can be characterized using ellipsometry. In this case the layer to be analyzed is the upper one, while the other parameters are known. b) Ellipsometric angles for WSe_2 monolayer on SiO_2 substrate as a function of the photon energy of the impinging light. The experimental data are taken at an angle of incidence of* 50°.

By fitting the calculated $\Psi(n,d)$, $\Delta(n,d)$ to the experimental Δ and Ψ it is possible to estimate the physical quantities of the layer. The accuracy of the results partly relies on the accuracy of the rest of parameters considered in the theoretical model. In our case n_0, d_2, n_2 and n_s. That is why the optical model is the most critical point in ellipsometry. In principle, since the ellipsometer gives two measurable real quantities, only two parameters can be retrieved about the sample. To increase the number of independently

measurable quantities one can repeat the measurement at different wavelengths (spectroscopic ellipsometry) or at different angles of incidence. Nevertheless, finding a value for multiple parameters requires a long computational time and a powerful numerical computation as well as experimental obstacles. The importance of an accurate model might cause some limitations in the determination of more complicated properties as the exciton binding energy and their environmental shift. This will be more deeply discussed later.

To conclude this section, I present the content of the appendix A of this publication. A simple Matlab code has been written to simulate the ellipsometric parameters generated by a slab of silicon on silicon dioxide substrate for different angles of incidence. This can be perhaps useful to understand the working principle of ellipsometry and how the thickness and refractive index of the material influence the values of Ψ and Δ.

Experimental setup: Accurion EP4

The experiments described in chapter 3 were performed using the "Ellipsometer EP4" from Accurion GmbH. The machine is shown in the figure (2.6) and is located in the clean room of the nanofabrication facility of Heriot Watt University. The setup is composed by the ellipsometer, by a light source, and by the computer to control the measurement and to analyze the data. This ellipsometer was used to perform spectroscopic ellipsometry inside an inert atmosphere kept in a glovebox. The light source is a collimated white light followed by a monochromator i.e. a diffraction grating able to provide a monochromatic radiation to be shined on the sample. The most powerful part of this instrument is indeed the software both for experiment setup and for data analysis. One can select a region of interest on the sample imaged on the microscope but is also possible to perform a so called "Δ, Ψ map" that means measuring the ellipsometric angles for an area of 100 by 100 μm on the sample. This allows with only one measurement to have an image of the surface of the sample itself and to characterize and investigate different regions of the sample. This is useful especially with complex TMDs heterostructures.

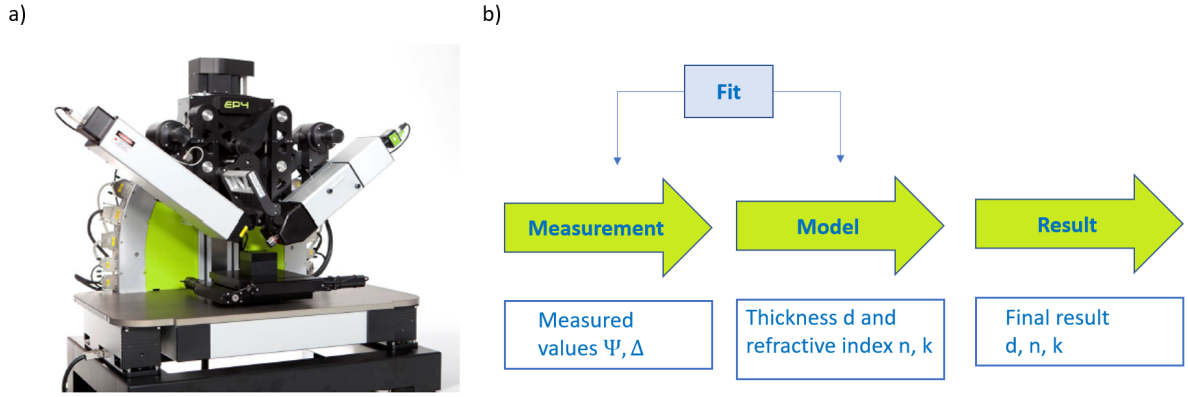

Figure 2.6: *a) The Accurion EP4 ellipsometer ;b) flow chart of ellipsometric measurement and data analysis. From accurion.com*

The analysis of data is done using the software "EP4 Model" by Accurion. As was described before, the working principle of this ellipsometer is based on the numerical fit

between experimental ellipsometric angles and the mathematical model (see appendix A). A list of dispersion of different materials can be imported and the layer stack composing the sample is built. The number of parameters used in the optical model of the unknown material can be decided: the thicknesses and the oscillators strength, damping and resonance frequency of Lorentz oscillators are the most widely used. The parameter to be fit can be arbitrary chosen so that is possible to perform a numerical minimization problem for one unknown at the time.

To conclude, ellipsometry is a non-invasive, and fast technique to characterize thin layers, even in case of a complex heterostructure. Nevertheless, as it will be explained in more details in chapter 3, an accurate model for the dielectric function of a material in presence of different environments is difficult to be realized. Moreover the number of free parameters is usually large and it is difficult to estimate the error on the measurement.

2.1.3 Dielectric function using ellipsometry

Ellipsometry allows to determine the thickness and/or the dielectric function of a single film or a complex multilayer stack. In the second case, knowledge of the dispersion model of the materials composing the stack is fundamental to reduce the number of unknowns. Moreover, in the framework of the investigation of 2D excitons, the measurement and determination of the model is the first step in the determination of the exciton binding energies as will be illustrated in the following sections along with the experimental results. The dispersion model should be physically significant, able to reproduce mathematically the dielectric function line shape (real and imaginary part) and finally should possess a reasonably small number of parameters. The numerical fit between experimental data and mathematical model should be indeed not too expensive in terms of computational resources. A possible approach to describe the dielectric properties of an inorganic material can be derived classically by considering the polarization of a material when irradiated in the UV and visible range. In the Fourier representation a material is described by

$$D(\omega) = \epsilon_0 E(\omega) + P(\omega) = \tilde{\epsilon}(\omega) E(\omega) \tag{2.20}$$

and the refractive index is related to the dielectric function

$$\tilde{n} = \sqrt{\epsilon_1 + i\epsilon_2} \tag{2.21}$$

The dielectric function physically describes the polarizability of the material and is a complex tensor whose imaginary part is proportional to the energy absorbed from the radiation.

In the visible and UV range the polarization involves mainly excitations of electrons (excitons) that generates an electric dipole, i.e. a dipole moment, while in the IR excitations can be associated to phonons, vibrations of ions in the lattice. Using a classical model, one can describe the motion of a negative and positive charge as a mechanical harmonic oscillator with the motional equations. Electrons are seen as ensemble of uncoupled harmonic oscillators due to localization of charges.

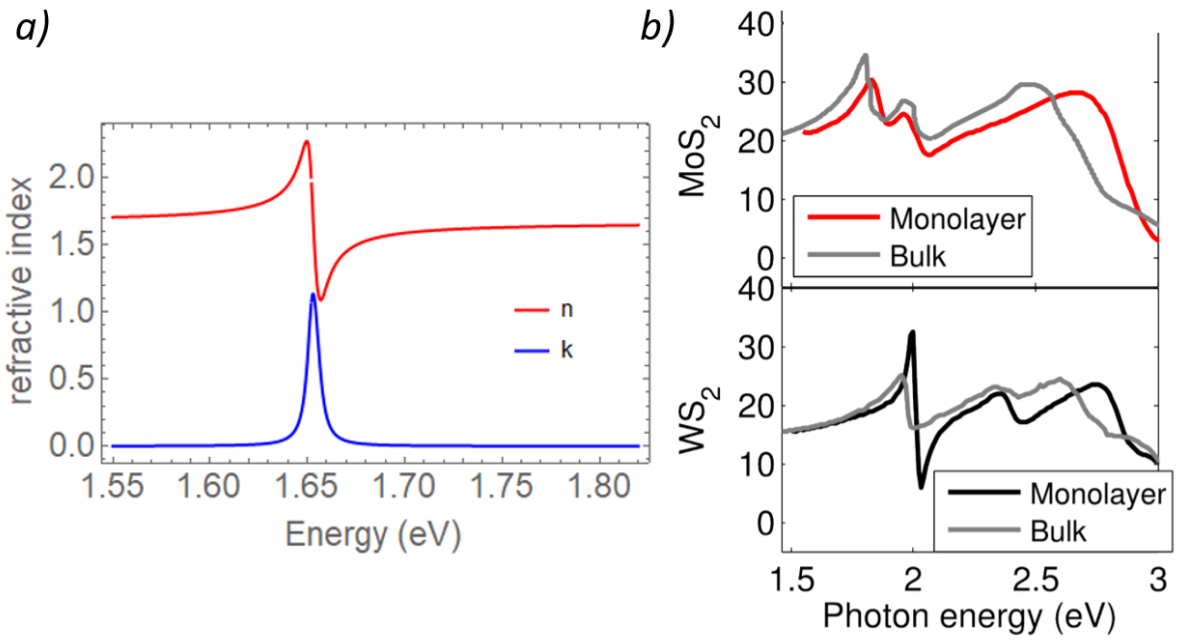

Figure 2.7: *a) Real and imaginary part of the refractive index calculated within the classical Lorentz oscillator model for a single resonance. b) Comparison of the dielectric function of monolayer TMDC crystals with that of the corresponding bulk material.* From [**15**].

The time dependent dipole moment is translated into an expression for the dielectric function of one single oscillator using the Lorentz oscillator model [**15**]:

$$\epsilon(\omega) = 1 + \frac{f}{\omega_0^2 - \omega^2 - i\gamma\omega} \tag{2.22}$$

Here ω_0 is the oscillator resonance frequency, γ is the damping factor due to the energy dissipation occurring in scattering processes. f is the oscillator strength and is proportional to the density of oscillators (atoms). Both organic and inorganic materials have of course more than one oscillator, caused by different phonon and exciton excitations. The correct dielectric function indeed can be written as a sum of oscillators with different resonance frequencies[**15**]:

$$\epsilon(\omega) = 1 + \sum_i \frac{f_i}{\omega_i^2 - \omega^2 - i\gamma_i\omega}. \tag{2.23}$$

Alternative dispersion relations can be found in literature and can be derived by classical electrodynamics, quantum mechanics or empirical considerations. Moreover the real and imaginary part of the dielectric function are related by the Kramer-Koenig relations. Therefore, once one of the two is known, the other one can be analytically obtained.

2.2 Confocal microscopy

It is known that the spectroscopy of micro and nano objects requires high spatial resolution and often low temperature conditions. Indeed, as it will be described in chapter 3, excited exciton states in the 2D semiconductors studied in this report present binding energies of the order of the thermal energy at room temperature $\simeq 25meV$. Therefore, a spectral determination of these features is hopeless if the couple electron hole is thermally dissociated. On the other hand, an experiment performed at cryogenic temperature (of the order of liquid He temperature, i.e. $4K$) would in principle allow the investigation of excitons excited states. The cost is the utilization of a different technique with a more complex apparatus: reflectivity of a broadband light source using a confocal microscope at cryogenic temperatures. In this section the principles of a confocal microscope, the experimental setup used and the broadband light reflectivity experiment will be presented.

2.2.1 Confocal microscope

The confocal microscope has the advantage of having a reduced focal volume in the sample therefore producing a better contrast imaging. The main difference with a standard optical microscope is the presence of a "pinhole" that allows the collection of light reflected by the sample from the focused point only: the core of an optical fiber can be used to collect the light. As it is possible to see in figure (2.8 a)), the light coming from optical planes different from the object plane, are filtered out by the pinhole.

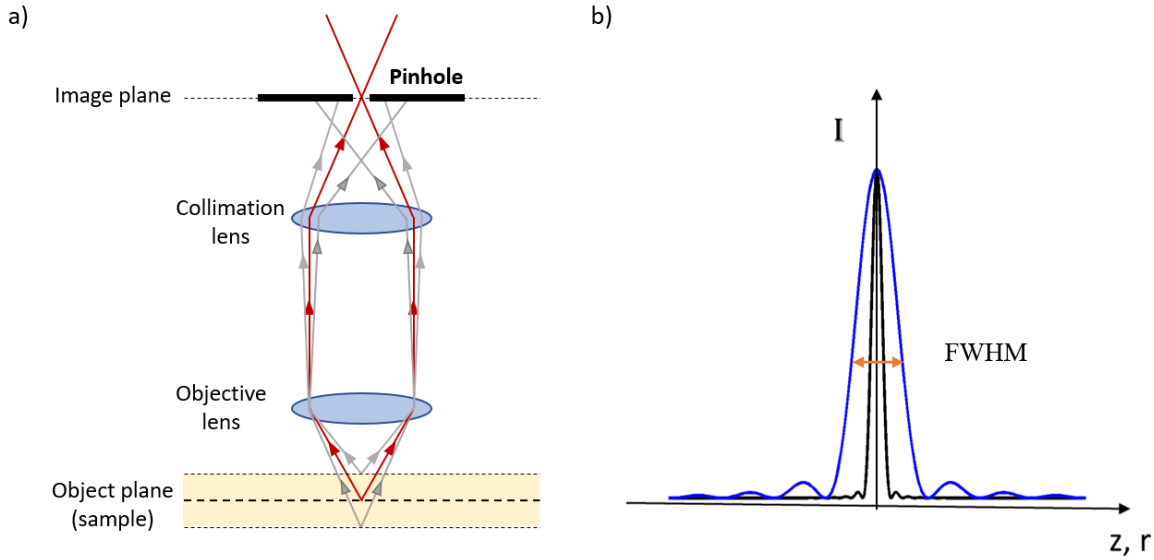

Figure 2.8: *a) Scheme of a confocal microscope: it is possible to visualize how the pinhole rejects the light coming from the vertical planes out of focus. b) Intensity distribution of a focused beam as a function of the radial coordinate (black) the Airy circle and the axial coordinate (blue).*

The name of this technique is originated by the fact that the pinhole is "confocal"

with the focal plane in the sample: this gets rid of light coming from all depths in the sample avoiding poor depth discrimination and low contrast. The image is formed by moving the beam across the sample: this *object plane scanning* consist of a spatial map of detector intensity vs. scan position.

As it is possible to see in figure (2.8) the optical system of a confocal microscope is rather simple and is composed by a collimation lens and an objective lens in an infinite conjugate design. To briefly analyze the improvements to the resolution for a confocal microscope one can consider the scalar theory that does not consider the polarization of light. At the focal plane, identified at $z = 0$ for a focused beam propagating in the z direction, the point spread function (i.e. the intensity distribution resulting from illumination with a plane wave) can be expressed in the radial (r) and axial (z) directions respectively by [**43**]

$$I(0,r) = \left[\frac{2J_1(2\pi/\lambda NAr)}{2\pi/\lambda NAr}\right]^2 I_0 \tag{2.24}$$

and

$$I(z,0) = sinc\left(2\pi/\lambda NA^2 z/4\right) I_0, \tag{2.25}$$

that indicates the distribution of intensity. Here, I_0 is the maximum intensity, NA is the numerical aperture of the objective, J_1 is the Bessel function of first order. The FWHM of these two functions is calculated as

$$\Gamma_r = 0.52\frac{\lambda}{NA}, \tag{2.26}$$

$$\Gamma_z = 1.77\frac{\lambda}{NA^2}. \tag{2.27}$$

The effect of a confocal microscope is to reduce the axial and radial spot size of a factor 1.4 comparing to wide field microscopy. Therefore 2.26 and 2.27 become

$$\Gamma_r = 0.52\frac{\lambda}{NA\sqrt{2}}, \tag{2.28}$$

$$\Gamma_z = 1.77\frac{\lambda}{NA^2\sqrt{2}}. \tag{2.29}$$

In this way the resolution is improved using objectives with high numerical aperture.

This rather simple setup should now be adapted to excite the sample at a temperature of 4K. In [**44**], the authors describe the design and performance of a fiber-based confocal microscope for cryogenic operation.

A desirable setup would provide precise and reliable sample scan and focus without occurring into drift even after many days of operation so that re-alignment is not required even after temperature changes or applied magnetic fields. The relative position of the sample and lenses has to be fixed and are therefore placed in a monolithic unit ("microscope stick") together with the nano-positioners for x, y and z directions. In this way the sample is placed in the focal plane of the two-lens microscope. The positioning system is made by three independent piezo-electric motors capable of working

at cryogenic temperatures. Moreover, titanium is used as nonmagnetic material for the realization of the microscope head that will be inserted into the cryostat. For operation at cryogenic conditions, the stick has to be placed into a non-magnetic stainless-steel tube where vacuum is created. Some exchange gas is later pumped inside to provide thermal exchange between the sample and the Helium bath in the cryostat itself. In this way the microscope is robust against gradient of temperature and magnetic fields and capable of scanning the sample with nanometer precision in the three directions over a range of approximately 5 millimeters.

2.2.2 Broadband differential reflectivity

A confocal microscope can be used for different purposes: form photoluminescence to high contrast microscopy of semiconductor structures and optical sectioning of transparent samples e.g. cells in biology. In the frame of the project described in this work, the confocal microscope was used to measure the reflected light from a van der Waals heterostructure in order to investigate the spatial and spectral position of excitonic emission peaks of these 2D materials.

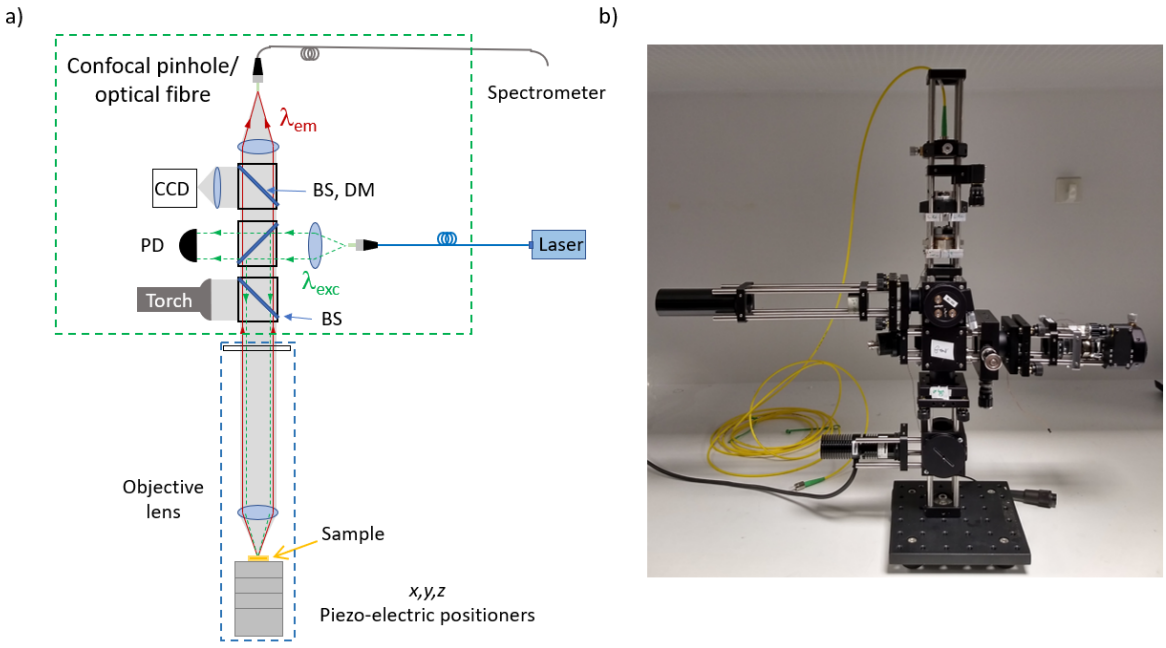

Figure 2.9: *Detailed scheme a) and picture b)of a confocal microscope used for experiments at cryogenic temperature. The drawing is based on the experimental setup used in the Quantum Photonics Lab at the Department of Physics of Heriot Watt University (UK).*

In figure (2.10) the scheme of the setup used for cryogenic measurements is shown. The lower part is immersed in the cryostat. The sample is mounted over piezo electric motors: these will move in the plane to provide a spatial image of the sample. The objective lens collects the light coming from the sample and focuses the excitation beam. The upper part is the microscope head and it is placed outside the cryostat. On the top

a collection fiber acts as a confocal pinhole while on the beam path three beam splitters allows part of the traveling light (up or downward) to follow different directions. In particular, a laser and a photodetector are used to align the optics and optimize the collection from the sample, while a CCD camera is used to image the sample. In our case (WL reflectivity) the sample was excited by the broadband white light produced by a tungsten halogen lamp from Newport. The WL travels to the sample and is reflected in the direction of the collection fiber going to the spectrometer. With this configuration it is possible to analyze the reflectance spectrum from a spatial region of the sample. What we are interested in is the differential reflectivity of the sample with respect to a reference point; usually the substrate i.e. a region with absence of spectral features typical of excitonic peaks. The differential reflectivity is defined as

$$\Delta R(\lambda, x, y) = \frac{R(\lambda, x, y) - R_0(\lambda, x_0, y_0)}{R_0(\lambda, x_0, y_0)} \tag{2.30}$$

Where $R_0(\lambda)$ is the reflectivity spectrum of the reference point $x = x_0, y = y_0$. The spectral dependence of the reflected light is measured by the spectrometer and expressed in arbitrary units, usually counts of the detector. The presence of sudden changes in the differential reflectivity spectrum indicates the spectral position of 2D excitons, while the information on the position on the sample comes from the spatial coordinates provided in the spectral map.

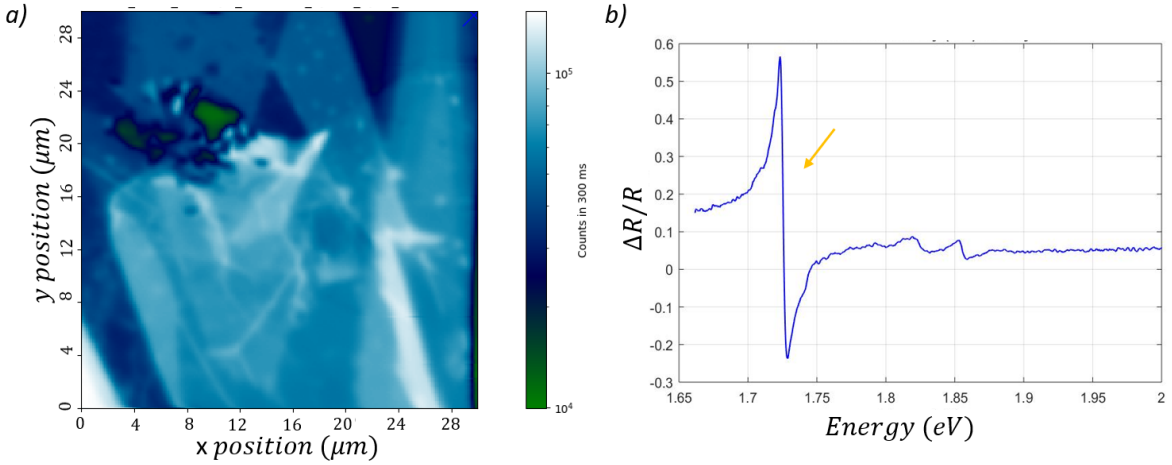

Figure 2.10: *a) Example of a WL spatial map obtained with the setup described above. The color scale is based on the integration of the spectrum over a specific interval. b) Differential reflectivity spectrum of a point on the sample to the left. The features are WSe_2 excitonic peaks of the excited states of the A exciton.*

2.3 Experimental setup for magnetic field measurements

As was mentioned in chapter 1, transition metal dichalcogenides are materials suitable for the so-called valley polarization. If time reversal symmetry is broken and a magnetic field is applied, the excitons in the K, K' valleys are no more degenerate in energy and it is possible to control further the electronic population in these particular points of the first Brillouin zone. Moreover, single spin population can be accessed by circularly polarized light. This is because the particular band structure of TMDs, where bands are splitted with opposite spins at the K, K' points, allows photo excitation to selectively energize electrons in one of the two valleys using circularly polarized light. In this section the experimental setup utilized during the broadband spectroscopy of excitons in presence of magnetic field will be described.

The experiment has been performed using the confocal microscope described in the previous section, the sample were mounted in a 4K temperature exchange gas inside the cryogen free cryostat (Attocube AttoDRY100). The top-loading, closed-circuit cryostat itself is in the bore of superconducting magnets capable of generating static magnetic fields up to $7T$. The superconducting magnets have the shape of a cylinder surrounding the sample, the latter is placed perpendicularly to the central axis of the cylinder itself. In this way, the magnetic field is pointing out of the plane of the 2D heterostructure, this is the so-called Faraday configuration, figure (2.11 b)). This is required because also the magnetic moment of excitons (confined in the plane of the 2D material) points out of the plane[3]. The application of a strong magnetic field is required since the g factor of Zeeman shifted excitons induces small variation in the spectral position of the peak, in the order of $0.1meV/T$. It is also possible to reverse the direction of the magnetic field. The measurement will consist therefore, in the swipe of magnetic field applied to the sample and the recording of the broadband reflected light spectrum as a function of B_{ext}. Access to both σ^+ and σ^- circularly polarized transitions is achieved by reversing the direction of the magnetic field or changing the angle of the $\lambda/4$ wave plate. This corresponds, respectively, to the interband optical transitions in the K and K' valley of the TMD.

2.3.1 Circularly polarized light

Circular polarization of electromagnetic wave is a polarization state in which the magnitude of the electric field is constant, but its direction rotates at a constant rate in time. Depending on the direction of the rotation with respect to the wave propagation, circular polarization is called left or right. The experimental setup to generate this polarization state, is presented in this paragraph.

[3]This can be seen by the expression of the Zeeman effect $E_Z = -\mu \cdot B_{ext}$

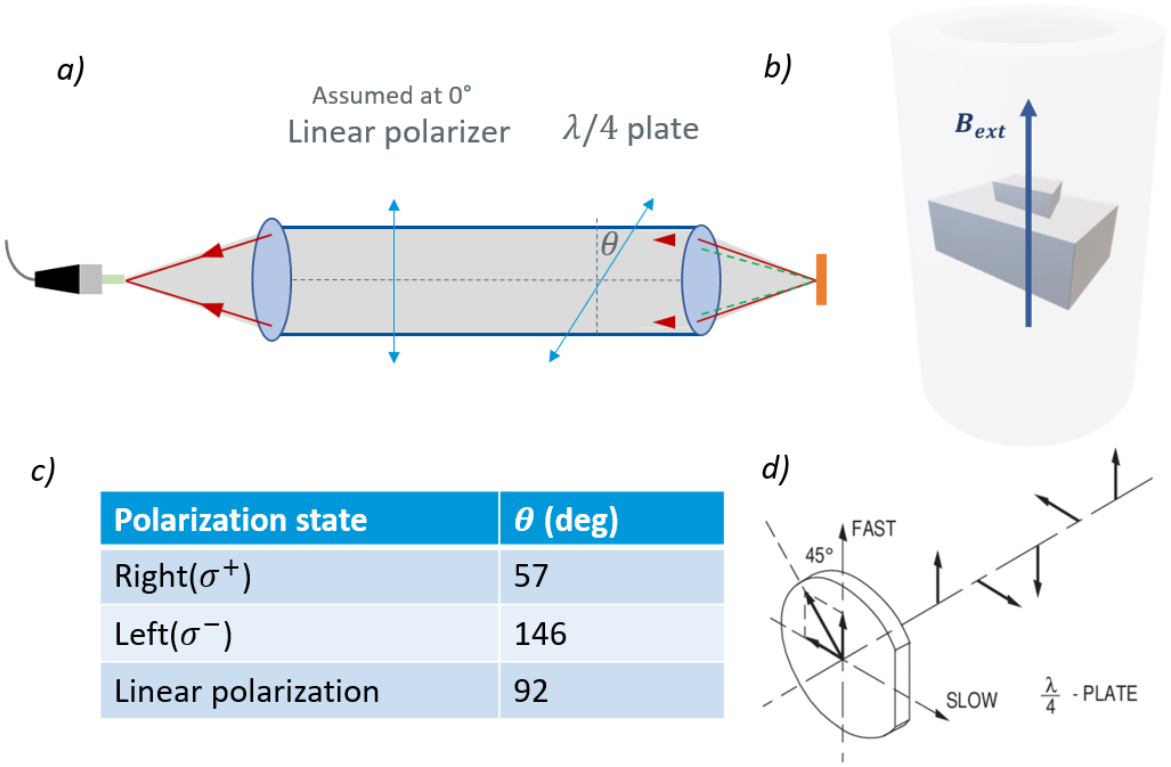

Polarization state	θ (deg)
Right(σ^+)	57
Left(σ^-)	146
Linear polarization	92

Figure 2.11: *a) Experimental setup for the production of circularly polarized light. The collection arm of the confocal microscope has, between the pinhole (left) and the sample (right), a linear polarizer and a $\lambda/4$ plate whose fast axis can be rotated by an angle θ with respect to the linear polarizer. b) Scheme of the Faraday configuration for the application of a magnetic field perpendicular to the plane of the sample. c) Table containing the values of the angle θ of the plate that produces left or right circularly polarized light. d) Representation of right hand circularly polarized light, the arrow indicates the direction of the electric field component of the wave. From newport.com*

The broadband unpolarized light is reflected back by the sample and travels in the collection arm shown in figure (2.11 a)). To turn linearly polarized light into circularly polarized light one can use a quarter wave plate, an optical component made by birefringent material. The light will travel in this case with two different refractive indices on the fast and slow axis depending on the orientation of the birefringent crystal. To do this effectively, one needs to orient the polarization axis at 45° to the fast axis as shown in figure (2.11 d)). This is the case of right hand circularly polarized light (RHCP), to obtain polarization in the other direction by rotating the $\lambda/4$ wave plate by 90°. As it is possible to see from figure (2.11 a)), the $\lambda/4$ plate and the linear polarizer are placed in the collection arm of the confocal microscope.

The table in figure figure (2.11 c)) instead contains the angles, with respect to the linear polarizer axis, that the plate should have to produce a left hand, right hand or linearly polarized light. These were experimentally determined placing the birefringent plate between two linear polarizers and by measuring the intensity passing through the

optical setup on a photodiode [4].

[4] Further information can be found on the website *www.newport.com/n/polarization*.

Chapter 3

Discussion

The aim of the following section is to present the experimental results obtained from our experiments. As mentioned in section 2 the adopted techniques are two: ellipsometry and broadband light reflectivity at low temperature. Therefore the data obtained using the two methods will be individually discussed and later compared. This can either increase the confidence on the obtained experimental results and underline different advantages and limitation of ellipsometry and confocal microscopy. The reason why the project evolved to white light reflectivity is the change from room to cryogenic temperature; liquid He at $\simeq 4K$. To correctly investigate the influence of environment on excitons, a physical model for the excitons binding energy is necessary. This requires the excited states $n = 3, 4, 5\ldots$ to be experimentally accessed. As it will be discussed below, a room temperature technique as ellipsometry does not allow this. To reduce thermal excitation we therefore decided to perform the experiment in a cryostat.

To further explore the A-exciton Rydberg states, a strong out of plane magnetic field has been applied on the sample. The results obtained using circularly polarized light are reported in the last section of this chapter.

3.1 Experimental results using ellipsometry

The investigation of the optical properties of thin TMDs carried out in this report is focused on two different 2D materials: WSe_2 and $MoSe_2$. In particular, the first technique used to characterize the sample has been Ellipsometry using the *Accurion EP4* described in the previous section. The first application of this technique is the measurement of thicknesses of thin materials but we are interested in the experimental dispersion of these material i.e. their complex dielectric function $\epsilon(\omega) = \epsilon_1(\omega) + i\epsilon_2(\omega)$ and its mathematical model. The change of dimensionality (from 3D to 2D) predicts notable new properties regarding bandgap and excitons: for this reason, the investigation focuses on monolayers of TMDs.

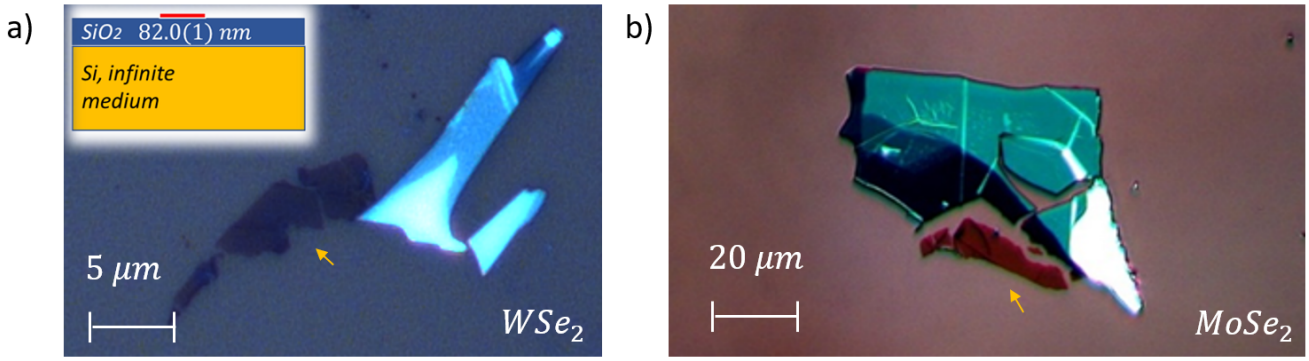

Figure 3.1: *Optical microscope images (magn. 50x) of the samples analyzed using ellipsometry. a) The mechanically exfoliated monolayer of the TMD WSe_2 is indicated by the arrow and has been transferred on SiO_2. In the inset it is possible to visualize the scheme of the (simple) layer stack. b) Monolayer of $MoSe_2$ obtained via mechanical exfoliation. The substrate is again SiO_2.*

We started with the simplest layer stack: a monolayer on *Si* substrate. In this way the effect of the environment on the optical properties is minimized. In figure (3.1) is possible to see the flakes at the optical microscope (magnification $50x$). The monolayers of WSe_2 and $MoSe_2$ have been obtained using mechanical exfoliation in an *Ar* atmosphere. The transfer from the tape to the substrate has been made using transparent *Polydimethylsiloxane* (PDMS). The substrate is made by *Si*, that can be treated as infinite thick medium, and SiO_2 whose thickness has been measured using ellipsometry resulting equal to $82.0(1)nm$ in the WSe_2 sample and $82.5(1)nm$ in the $MoSe_2$ sample. The thickness of the monolayers can be measured, e.g. with atomic force microscope (AFM), and its value is available in literature: we have used the value of $0.65nm$ that can be assumed constant for all the TMDs monolayers since their crystalline structure is identical [**45**]. Moreover, the dimension of the flakes is approximately 8 by $20\mu m$ for WSe_2 monolayer and 40 by $10\mu m$ for $MoSe_2$.

To investigate how the dielectric environment affects the excitons in our samples, the monolayer of WSe_2 has been encapsulated in hexagonal boron nitride (hBN). Optical microscopy images of the two samples fabricated in the cleanroom facilities and characterized with ellipsometry are shown in figure (3.2).

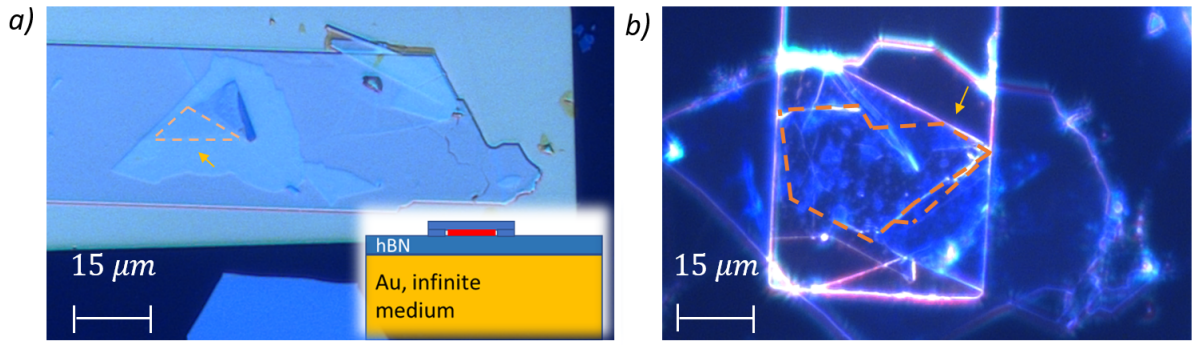

Figure 3.2: *Optical microscope images (magn. 50x) of the encapsulated monolayers analyzed using ellipsometry. Here the WSe_2 monolayer has been encapsulated in hBN after exfoliation. The layer stack is placed upon thick gold: in the inset it is possible to visualize the sample scheme. a) sample "A01" and b) sample "A02" (image obtained with dark field filter), the monolayers are indicated by the dashed orange lines.*

Since the sample was fabricated to allow the application of an electric field, the layer stack is composed as follows: the substrate is now an evaporated gold contact electrode with thickness of $\simeq 90nm$ [1] and upon it the WSe_2 monolayer is encapsulated between two layer of hBN. For the sample "A01", fig. (3.2 a)), the thickness of the bottom hBN is $50.1(1)nm$ while the upper one is $12.1(1)nm$ thick[2]. The sample "A02" instead, fig. (3.2 b)), has hBN thicknesses of $60(1)nm$ and $11.0(1)nm$.

In literature the dielectric function of thin TMDs is usually modelled as a sum of Lorentzian oscillators plus a constant term according to equation (2.23) here reported for reference:

$$\epsilon(\omega) = 1 + \sum_i \frac{f_i}{\omega_i^2 - \omega^2 - i\gamma_i\omega}, \tag{3.1}$$

and it is usually experimentally accessed using white light reflectivity [**15**]. The approach followed in this project is exploiting the powerful fitting program provided by the ellipsometer *Accurion EP4*. Using the expression (3.1) the parameters in our mathematical expression are: the real and imaginary part n and k of the complex dielectric function, and then the strength, damping and resonance energy of each oscillator. These will give us the frequency dependence in the expression $\epsilon(\omega)$.The parameters of a finite number of oscillators (usually 5 or 6), determine the shape of the dielectric function and therefore the change in the polarization state of the light reflected by the sample and detected by the ellipsometer. A correspondence between the experimental Ψ and Δ angles and the excitonic peaks intensity position and width can be obtained minimizing the difference of the calculated and experimental ellipsometric curves. The next section contains the experimental results obtained from the sample mentioned above.

[1] Due to the large thickness of this metal, this layer can be treated as infinite and therefore the SiO_2 below it can be neglected. This is justified by the fact that the Ψ and Δ angles do not change by varying the SiO_2 thickness in the model.

[2] These number have been obtained by the measurement using ellipsometry.

3.1.1 Exciton energies and dielectric function

The function $\epsilon(\omega)$ can be in principle accessed using ellipsometry exploiting the numerical fit of the measured ellipsometric angles Ψ and Δ. This requires a mathematical modelling of the dispersion of a material. We use the sum of Lorentzian oscillators to represent the excitonic absorption peaks and a constant term. Since the used mathematical expression is complex, the result will be a refractive index with a real (associated to the propagation) and an imaginary part (associated to the absorption). The ellipsometric angles were obtained experimentally for a wavelength range $\lambda = 400 - 800nm$ corresponding to, approximately, $1.4 - 3eV$ using nulling ellipsometry. After that, the data analysis consists in the building of the sample layer stack and of the Lorentzian parameters that form the WSe_2 refractive index. The parameters are then fitted and a result for the oscillators strength, damping and resonance energy is provided with the related standard error. To visualize the result obtained by the fit, it is possible to plot both the experimental Ψ and Δ angles and the one expected by the just-found model. In figure (3.3) it is possible to see this result in the case of our sample of WSe_2. As one can see the fitted model follows the experimental data and allows us to identify the features (indicated by the blue arrows) introduced by the excitons [3].

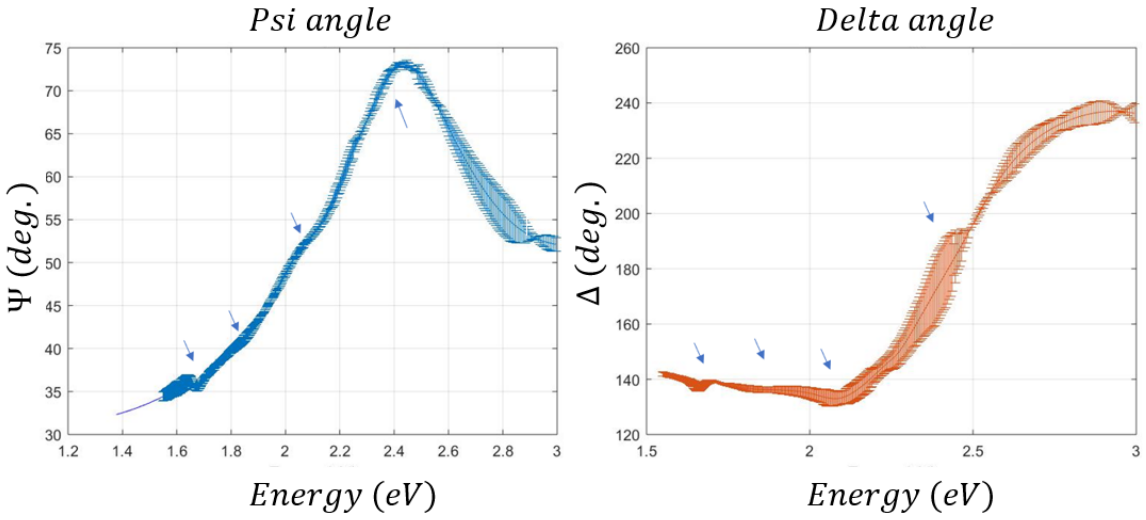

Figure 3.3: *Psi and Delta angles obtained measuring a WSe_2 monolayer with ellipsometry. The solid line represent the fitted model while the vertical bars represent the difference between experimental values and the fit itself. The arrows are indicating the features corresponding to the exciton resonances.*

The Accurion software provides a calculation for the ellipsometric angles using its estimation of the WSe_2 dielectric function. In chapter 2 it is shown how to obtain the dielectric function starting from the mathematical model of Lorentzian oscillators. The result for WSe_2 is shown in figure (3.4 a)) where the experimental refractive index of the monolayer is plotted as a function of the incoming photon energy. Note how the

[3] As one can expect indeed, the transfer matrix determines the ellipsometric angles, and it is modified by the dispersion of the materials composing the stack.

imaginary part, corresponding to the optical absorption of a material, present a series of peaks: this is what one expects at the energy corresponding to the creation of the bounded electron-hole pair (exciton). In figure (3.4 b)) instead the real part of a single Lorentzian is displayed together with the total imaginary part of the refractive index arising from the sum of equation (3.1). The peak located at low energy is the strongest and corresponds to the 1s state of the A exciton.

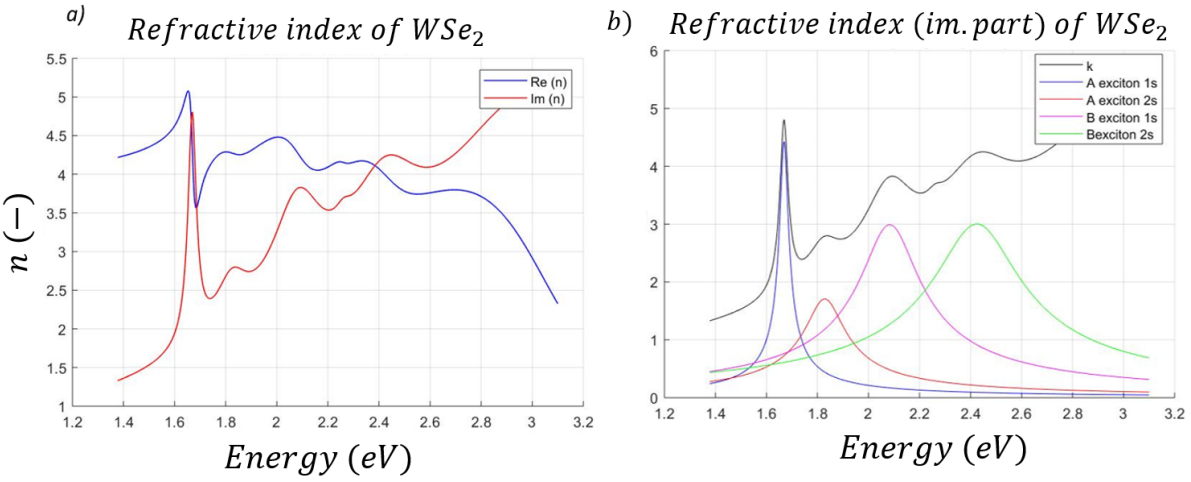

Figure 3.4: *Experimental dispersion of the WSe_2 monolayer on SiO_2 substrate. a) Real (blue) and imaginary part (red) of the refractive index $n(\omega)$ of WSe_2. This result has been obtained fitting the experimental data to the mathematical model. In b) it is possible to see how the sum of Lorentzian, centered at exciton resonance frequency, gives the final result.*

While the oscillators damping and strength determine how strong and sharp is an absorption peak, the resonance frequency, ω_0 indicates where the peak is spectrally located. This is, in this report, the most significant parameter since it allows us to investigate the excitonic properties of the material and to characterize them. The simplest and most common physical model for a 2D intralayer exciton is the Rydberg model described in chapter 1. The reduced dimensionality of the system predicts a series of spectral lines according to equation (1.29), here reported for sake of clarity:

$$E_n = E_g - \frac{R_y^*}{\left(n - \frac{1}{2}\right)^2}. \tag{3.2}$$

In table 3.1 the characterization of the excitons in WSe_2 on SiO_2 substrate is presented.

The experimental values of the energies have been obtained by the fit and the standard error is reported along with the mean value. Two different series of energy have been identified with the name A and B and for each of them only two experimental points have been accessed for $n = 1, 2$. If n increases indeed, the exciton is located closer to the gap energy E_g and therefore the binding energy E_b defined as $E_b = E_g - E_n$ becomes smaller. It is possible to see for $n = 2$ the E_b is comparable with the thermal excitation $k_bT \simeq 25meV$ at room temperature. Therefore further excited states might be thermally

Exciton	n	$E_n(eV)$	$E_g(eV)$	$Ry^*(eV)$	$E_b(eV)$
A	1	1.669(1)	1.850	0.045	0.181
	2	1.83(1)	1.850	0.045	0.020
B	1	2.086(5)	2.473	0.097	0.387
	2	2.43(1)	2.473	0.097	0.043

Table 3.1: *Exciton peaks resonance energies for WSe_2 monolayer on SiO_2 at 300 K obtained by fitting the ellipsometric angles with the Lorentz model. The gap energy, reduced Rydberg constant and exciton binding energy have been calculated using the Rydberg model for intralayer excitons using equation (1.29).*

separated and not accessible using this optical analysis. All these quantities have been obtained by equation (3.2) . It is important to remind that, in low dimensional systems as for example a monolayer TMDs, the exciton binding energy is predicted to be 4 times larger than the 3D (bulk) case making it easier to identify excitonic peaks in the optical spectrum.

The same analysis applies to the second material characterized: $MoSe_2$ monolayer on SiO_2 whose optical microscope image is shown in figure (3.1 b)). In table (3.2) the experimental values for the $MoSe_2$ excitons resonance energies are reported along with the standard error arise from the numerical fit. It is possible to see that the 1s state of the A exciton is at lower energy with respect to the WSe_2 ML, this results in a larger binding energy for this state. The result of the fitting in this case is slightly worser than the previous material with an error on the second decimal (tens of meV) for the resonance energies. The 2D Rydberg model for excitons has been used also in this case to calculate E_b, E_g and R_y^*.

Exciton	n	$E_n(eV)$	$E_g(eV)$	$Ry^*(eV)$	$E_b(eV)$
A	1	1.56(1)	1.83	0.067	0.267
	2	1.79(1)	1.827	0.067	0.030
B	1	1.79(1)	2.138	0.085	0.341
	2	2.10(5)	2.138	0.085	0.038

Table 3.2: *Exciton peaks resonance energies for $MoSe_2$ monolayer on SiO_2 at 300 K obtained by fitting the ellipsometric angles with the Lorentz model. The gap energy, reduced Rydberg constant and exciton binding energy have been calculated using the Rydberg model for intralayer excitons using equation (1.29).*

For sake of completeness our experimental data will be compared with the one present in literature in order to understand the reliability of the method followed in this report. The excitons in thin TMDs can be investigated with different techniques. In the work of [**46**] the exciton binding energy of WSe_2 is determined to be $0.37eV$ and the resonance energy of the A exciton (*1s* and *2s*) are $1.65eV$ and $1.83eV$. The B exciton is instead at $2.08eV$. These peaks, A and B, correspond to the lowest energy exciton states originated from transitions from the two highest energy spin-orbit split valence bands to the conduction band around the K point in the Brillouin zone. Also the experimental

results in [**47**] agree with the data contained in table 3.1 . For what concerns the $MoSe_2$ [**26**] reports an experimental energy for the A exciton of $1.55eV$. Nevertheless for the calculation of the exciton binding energy, the authors do not use the pure 2D Rydberg hydrogenic model, but use instead the calculated electronic bandgap. In this case the binding energy is simply calculated by performing the difference between the electronic bandgap and the excitonic peak. This results in a larger binding energy than the one reported in table 3.2.

To illustrate the 2D exciton model it is possible to plot the numerical values in tables 3.1 and 3.2. Figure (3.5) helps to visualize the Rydberg series of the excitonic energies of monolayer WSe_2 a) and $MoSe_2$ b). The circles represent the experimental points (energies) as a function of the integer n. The solid lines are the line shape of equation (3.2): there is one line for the A and for the B excitons respectively. The dashed line is the gap energy E_g and corresponds to the limit for $n \to \infty$ of equation (3.2). Moreover, the difference in energy between the experimental point and the corresponding gap energy is the binding energy of the exciton. Only two experimental points have been found using ellipsometry. Nevertheless the large energy separation between the A and B 1s excitons, especially in WSe_2[4], opens the window for the observation of the excited states. Unfortunately, the excited states above the *2s* cannot be clearly identified with ellipsometry at room temperature: this is probably due to the weakness of these transitions compared to the ground state ones and to the thermal excitations in the dielectric, that might dissociate the e-h couple.

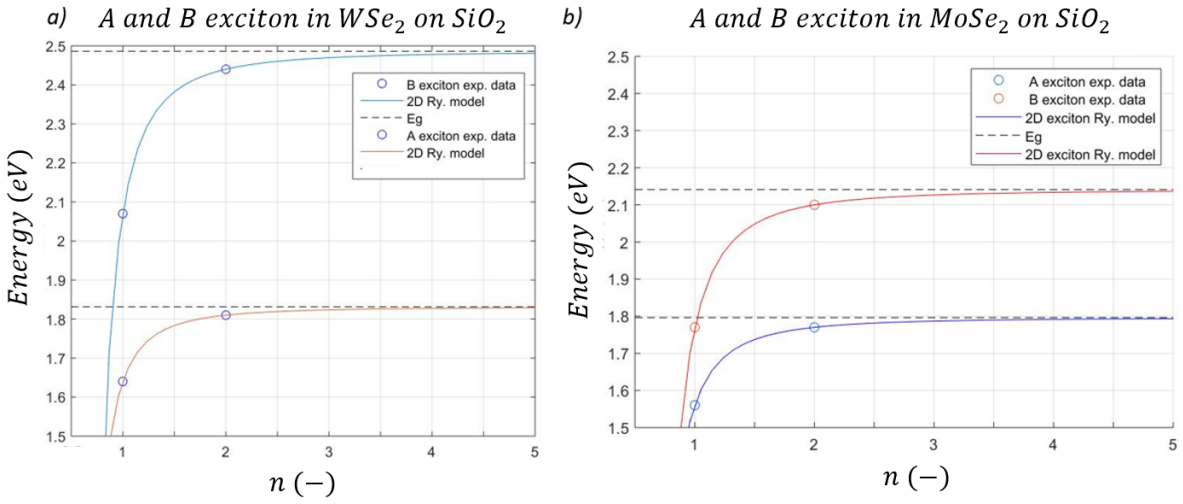

Figure 3.5: *Representation of the resonance energies for excitons experimentally determined at room temperature. a) Rydberg series of the A and B excitons in WSe_2 monolayer: the energy is plotted as a function of the "quantum number" $n = 1, 2, 3...$ b) Excitons in $MoSe_2$ monolayer. The solid lines represent the line shape of (1.29) while the dashed line corresponds to the excitonic bandgap i.e. the energy that separate the electron hole pair.*

As previously mentioned, a third layer stack has been measured. The samples “A01”

[4]This is due to the strong spin orbit coupling in monolayer WSe_2: more details can be found in chapter 1 of this report.

and "A02", shown in figure (3.2), have the monolayer of WSe_2 encapsulated in hBN. The different dielectric environment in which the monolayer is embedded is expected to affect the exciton binding energy as predicted in [**27**]. In particular, for distances exceeding nanometers the screening is determined by the surrounding material: therefore, with respect to the case of monolayer on bare SiO_2, the hBN is expected to both red-shift the excitonic resonances of the thin TMD and to reduce its bandgap. Moreover, the excited states ($n > 1$) are expected to have a larger shift due to larger Bohr radius. The new layer stack has been used for a numerical fit similar to the previous case. The dielectric function of the encapsulated WSe_2 has been found to be different from the previous case and the excitonic resonances are reported in table 3.3.

As expected, the binding energy of the A excitons is reduced by $\simeq 20meV$ for the 1s and the excitonic resonances are red shifted by $\Delta_{A,1} = 30meV$ and $\Delta_{A,2} = 40meV$.

Due to the increased complexity of the layer stack, the numerical fit did not allow us to investigate the excited states of the B exciton when the ML was encapsulated. This can be seen in figure (3.6 b)) where the real and imaginary parts of the calculated refractive indices $n(\omega)$ have been plotted in the case of WSe_2 on bare substrate (red lines) and encapsulated in hBN (blue lines).

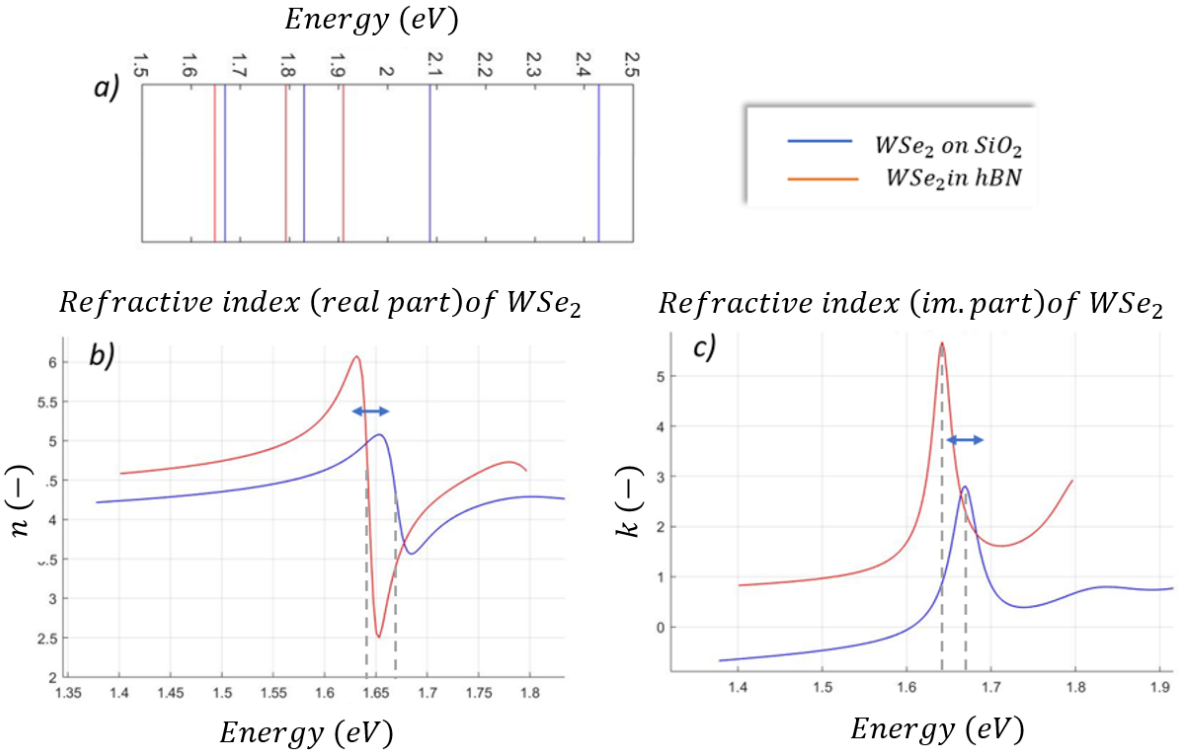

Figure 3.6: *Here the influence of the dielectric environment on the position of the excitonic peaks is demonstrated. The exciton energy is red-shifted when the monolayer is encapsulated in hBN due to the larger screening and the exciton binding energy E_b is reduced. In a) is possible to see the difference in energy for the A exciton (n=1,2) and B exciton (n=1). In b) and c) the refractive index of the WSe_2 monolayer is compared in the two cases: when encapsulated (red) and when deposited on SiO_2.*

After presenting our experimental data and analyzing them in the frame of the simple 2D Rydberg model, it is worth to introduce in the description of our physical system the influence of the surrounding environment in a quantitative and physically significant way. In chapter 1 it has been pointed out the experimental observation of a deviation from the Rydberg energy ladder of the 1s and 2s exciton states in TMDs. This is due to the dielectric inhomogeneity of these 2D structures when deposited on a substrate or incapsulated in a different material. The charged particles composing excitons experience a coulomb interaction with a non-uniform environment: for large e-h distance (excited states) the electrostatic interaction scales with the dielectric constant of the surrounding medium while at short distances the in plane screening weaken this force [**48**].

Exciton	n	$E_n(eV)$	$E_g(eV)$	$Ry^*(eV)$	$E_b(eV)$
A	1	1.64(1)	1.811	0.041	0.163
	2	1.79(1)	1.811	0.041	0.018
B	1/2	1.91(5)	-	-	-

Table 3.3: *Exciton peaks resonance energies for WSe_2 monolayer encapsulated in hBN at 300 k obtained by fitting the ellipsometric angles with the Lorentz model. The gap energy, reduced Rydberg constant and exciton binding energy have been calculated using the Rydberg model for intralayer excitons using equation* (1.29).

To accurately investigate the excitonic properties of TMDs in Van der Waals heterostructures one needs to access experimentally the higher excited states $n = 3, 4 \ldots$. To do so, a different technique has been employed: the results obtained with white light reflectivity at low temperature are presented in the following section.

3.2 Experimental results using broadband reflectivity

As explained in the previous section, to thoroughly characterize the excitonic transitions of TMDs, we want to perform experiments at low temperature. This will help us getting sharper transition linewidth and minimize phononic effects (thermal excitations in the material): in this way the weakly bounded ($E_b \simeq 20meV$) excited states of excitons will not be found to be thermally dissociated.

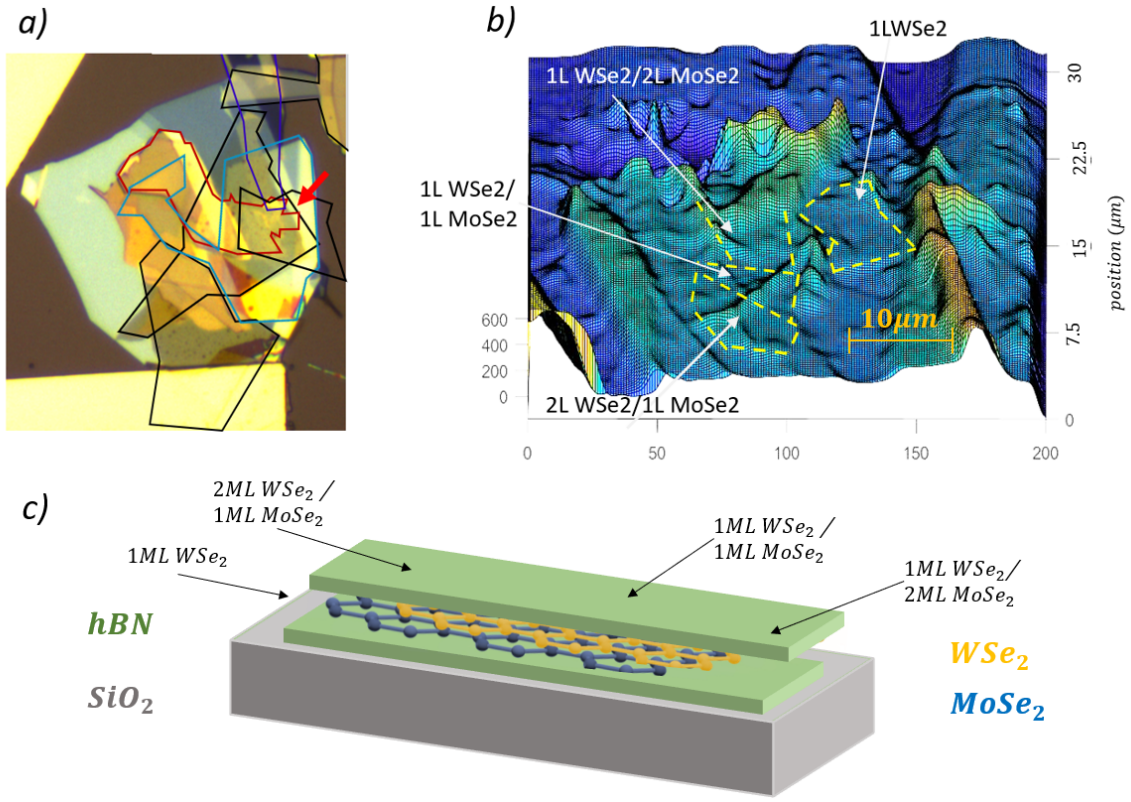

Figure 3.7: *Description and topography of the sample investigated with the confocal microscope. a) Optical microscope image of the vdW heterostructure (top view). The solid lines traced indicate a specific component of the layer stack: red TMD heterostructure, blue top hBN and black/purple graphene. b) 3D surface plot obtained using reflected light from the sample: the topography is extremely clear and it is possible to individuate the region of interest in the structure. c) Side view of the layer stack: the colours correspond to different materials. The size is not scaled for clarity and better visualization of the layer stack composition.*

The technique used is broadband reflectivity. The principle and implementation of this technique has been described in chapter 2 but here the key features will be reported for clarity. The sample is placed in a cryostat and a power stabilized quartz light source is wave-guided and shined onto the sample. A confocal microscope collects the reflected light from the sample giving us a spatial resolution of half micron[5]. A spectrum of the

[5]In general, the spatial resolution depends on the core of the collection fiber and on the wavelength of the radiation. Since we are working in the visible range, and estimation can be calculated by $\lambda/2$.

reflected light is collected for every spatial point giving rise to a 2D map. A nice way to image the sample is to plot the intensity integrated at a specific wavelength range as a function of the x and y position on the sample. This gives rise to a 3D surface that allows us to image the sample with a good resolution providing its topography: this can be seen in figure (3.7 b)). Moreover, the location and linewidth of excitonic transition can be identified by peaks in the differential reflectivity spectrum, obtained using equation (2.30).

The sample characterized with this technique is an heterostructure with two different thin TMDs ($MoSe_2$ and WSe_2) whose layer stack and topography are rather complex. Figure (3.7) shows a sketch of the regions of particular interest on this van der Waals heterostructure. The heterostructure made by $MoSe_2$ and WSe_2 is encapsulated in hBN and offers different regions for optical characterization: WSe_2 monolayer (size of 8 by 8μm), 1ML $WSe_2/1MLMoSe_2$ (size of 5 by 4μm), 2ML $WSe_2/1MLMoSe_2$ (size of 5 by 5μm) and 2ML $WSe_2/1MLMoSe_2$ (size of 5 by 5μm). The hBN thickness has been estimated by optical contrast and found to be around 30μm for both the top and the bottom layer[6].

Magnetic effects are expected to be observable in excitons due to the interaction of electrons with the external magnetic field. The experimental setup allows to apply a strong magnetic field (up to 7 T) perpendicularly to the sample: the excitons transition energies are expected to shift in these conditions for the manifestation of the Zeeman splitting and the diamagnetic shift. These information can be accessed using again differential broadband reflectivity of polarized light. The experimental results are reported in the second part of this chapter.

3.2.1 Exciton energies and transition linewidth

The sample described above has been investigated and the experimental results are hereby reported. The measurement performed by the spectrometer consists of a map of spectra of the reflected light for each region of the sample. An excitonic transition causes a peak at a wavelength corresponding to the transition energy, to make every feature clearer, one can choose two different points on the sample and perform the differential reflectivity $\Delta R/R$.

The reference point should be chosen in such a way that the reflected light will not contain information about the excitonic transitions of interest: equation (2.30) shows indeed the spectral differences between the two selected regions.

Once the region of interest and the reference have been selected, one can plot the differential reflectivity spectrum as shown in figure (3.8). To analyze the effect of the dielectric environment on the transition energies of excitons, one should start from the region of the sample where the WSe_2 monolayer is surrounded by bare hBN. The measurement using unpolarized light (3.7) allows to identify spectrally the excited states of WSe_2 monolayer encapsulated in hBN up to the 4s state. That means that with respect to room temperature measurements, the weakly bounded 3s and 4s state can be now

For details see chapter 2.

[6] Some layers of graphene have been added to apply biases to the structure and investigate the effects of doping and static electric field.

located.

To obtain a reduction of the noise in the differential reflectivity spectrum, it is possible to exploit polarized light. By exciting the sample with circularly polarized light (σ^+ or σ^-) one can select the electronic population involved in the light absorption thus increasing the signal to noise ratio. The improvement of the suggested method on the $\Delta R/R$ spectrum is relevant. This can be seen in figure 3.9 where the detected differential reflected light is displayed both in case of, respectively in blue and orange, σ^+ and σ^- circularly polarized light. Surprisingly, new peaks can be recognized, and we identify these two new transitions with the excited 5s and 6s excitonic states of WSe_2 monolayer.

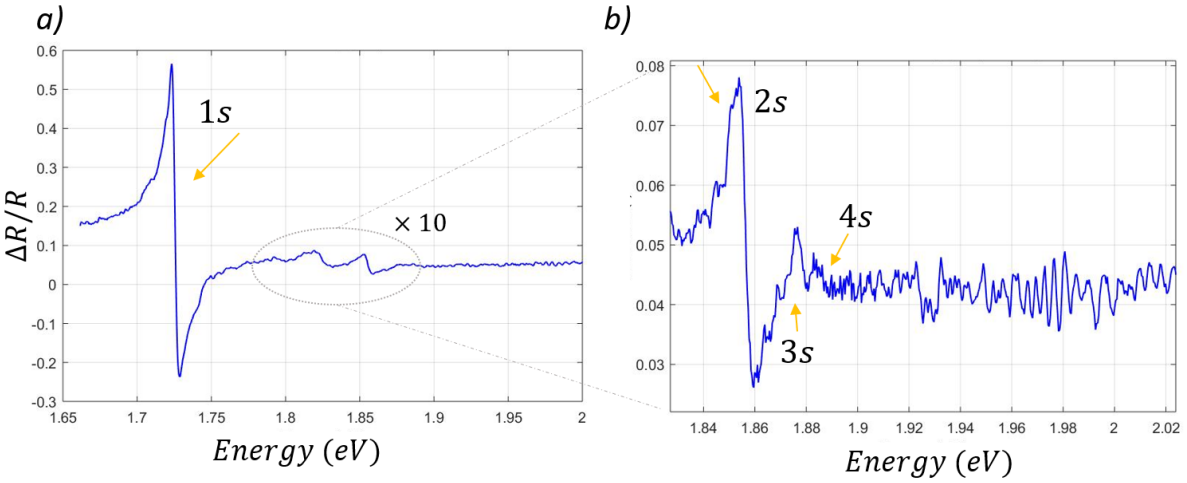

Figure 3.8: *a) Plot of the experimental differential reflectivity $\Delta R/R$ of WSe_2 monolayer encapsulated in 30nm hBN at 4K. In b) the spectral region circled is zoomed in to individuate the excited states of the A exciton. It is remarkable how this technique allows to clearly identify the exciton resonances. The reference has been chosen in a region of the sample without the monolayer.*

A number of resonance peaks can be identified, and their spectral position can be obtained by numerical fit of the experimental data. To do so, we have used a code in Wolfram Mathematica that simulates the layer stack using the transfer matrix method to calculate the differential reflectivity. This programming language was chosen due to its powerful analytical computation. Instead of a numerical evaluation, the code creates analytical expressions for the transfer matrices and the refractive indices of the materials: the numerical evaluation is made only after the numerical fit. The model used for the excitonic resonances is again the Lorentz oscillator (3.1)[7]. Figure (3.10) shows the experimental data and the plot of the analytic function calculated by the numerical fit.

[7]Further information about the code utilized for the numerical fit of the resonance peaks can be found in Appendix B, at the end of the report.

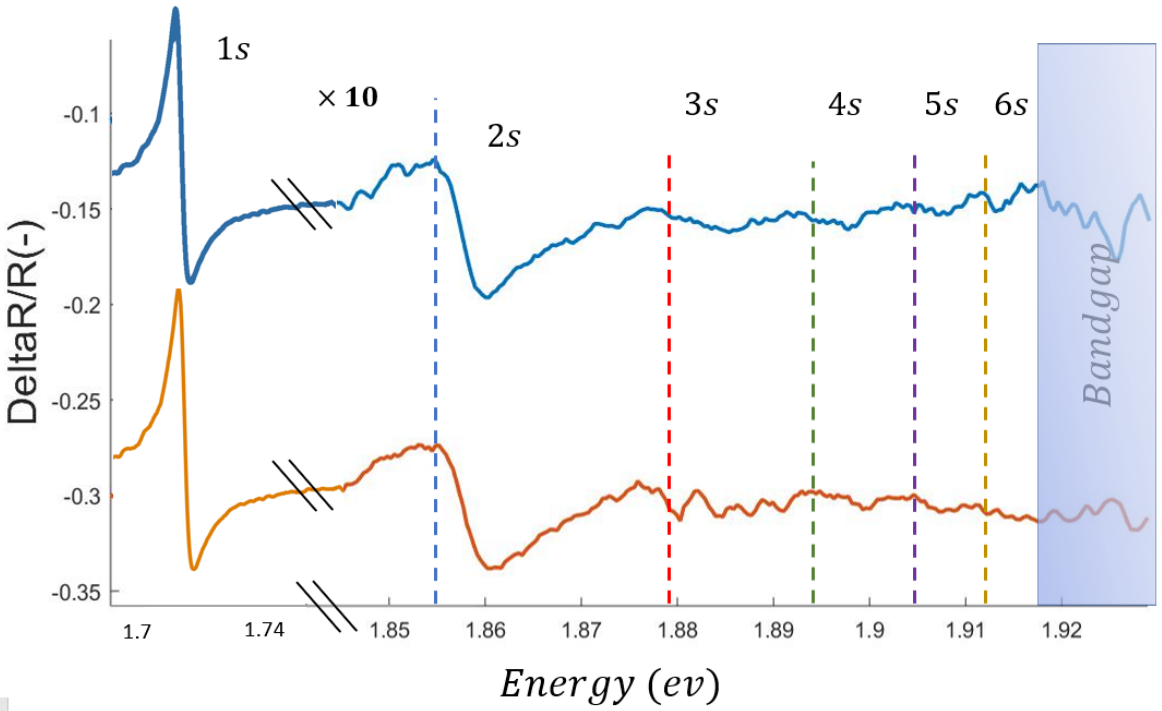

Figure 3.9: *Plot of the experimental differential reflectivity $\Delta R/R$ of WSe_2 monolayer encapsulated in 30nm hBN at 4K using polarized light (blue the RHCP and orange the LHCP). The higher excited states of the A exciton have been magnified by ten times for clarity. The result obtained with polarized light, if compared with the one in figure 3.8, shows a strong noise reduction that allows the 5s and 6s to be identified using broadband differential reflectivity. This is, probably, a manifestation of the selection on the electron population using σ^+ or σ^- light.*

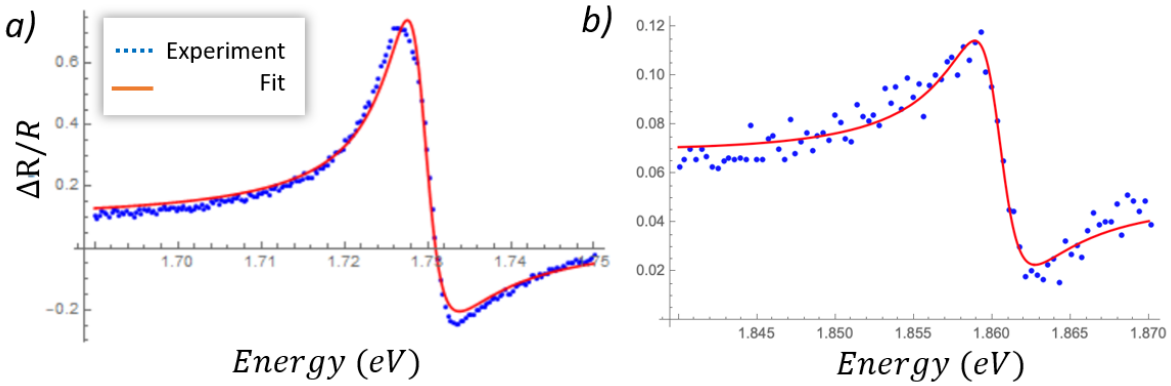

Figure 3.10: *Results of the numerical fit on the experimental differential reflectivity for the encapsulated WSe_2 monolayer. a) fit of the 1s state of the A exciton series and b) fit of the 2s state of the A exciton.*

We have performed the calculation for each peak in the spectrum and the results, both for the transition energy and linewidth, are summarized in table 3.4. A recent

article, [**49**], has reported a similar investigation on the excited states of A exciton in WSe_2: the results presented below, agree with the ones present in literature.

Exciton	n	$E_{n,exp}(eV)$	$E_n(eV)$	$FWHM(meV)$
A	1	1.7240(5)	1.712	5(1)
	2	1.8575(5)	1.843	5(1)
	3	1.8783(5)	1.864	6(1)
	4	1.893(1)	1.873	7(1)
	5	1.903(1)	-	8(2)
	6	1.911(1)	-	8(2)

Table 3.4: *Here the results ($E_{n,exp}$) of the numerical fit for the excited A exciton states of WSe_2 monolayer are reported. Our results includes the linewidth of the optical transition observed. The values have been compared with recent literature (E_n)* in [**8**].

If one compares the transition energies with the results of ellipsometric measurements at room temperature (table 3.3), as expected, can observe a blue-shift in the resonance positions. Moreover, the transitions in the samples where the monolayer is encapsulated have a sharper linewidth. The encapsulation indeed is protecting the thin TMDs avoiding contaminations on the monolayer surface, maintaining its quality.

This new technique allowed us to investigate the excited states of the A exciton in WSe_2 monolayer accessing states that were not visible using room-temperature ellipsometry. The experimental points can be plotted as a function of the integer n in the frame of the 2D hydrogenic model. By fitting the experimental data with the functional form of equation (1.29), one can obtain an estimation for the gap energy $1.916eV$ and the reduced Rydberg constant $0.0441eV$: the result is displayed in figure (3.11).

This numerical fit with the Hydrogenic series allows one to calculate the binding energies of the using the quasiparticle bandgap, the binding energy of the *nth* exciton state is therefore [8]

$$E_b^n = \frac{\mu e^4}{2\hbar^2\epsilon^2(n-1/2)^2}, \tag{3.3}$$

Where ϵ is the effective dielectric constant and μ is the exciton reduced effective mass.

	$E_g(eV)$	$Ry^*(eV)$	$E_b^{1s}(meV)$	$E_b^{2s}(meV)$	$E_b^{3s}(meV)$	$E_b^{4s}(meV)$
$1ML$ in hBN	1.916	0.044	192	63	37	23

Table 3.5: *Results of the numerical fit of the experimental excitons energies in WSe_2 encapsulated in hBN using the functional form 1.30.*

Nevertheless, the energies in our experiment are in contrast with this dependence on n. In particular the scaling with the quantum number is much weaker and a simple fit to equation 1.30 is not possible. This result has been previously observed in the case of MoS_2 monolayer in [**25**] where the $n = 1, 2$ states are observed to deviate from the

[8] For details of the Hydrogenic Rydberg model for electron hole interaction in excitons, one can refer to chapter 1 of this manuscript.

hydrogenic model while the $n = 3, 4, ..$ possess a reasonably hydrogenic scaling. For this reason, we used these data points to obtain the quasi particle bandgap E_g. The result of the numerical fit can be seen in figure (3.11 a)) where the experimental points for $n = 1, 2$ are significantly deviating by the 2D Hydrogenic model (red line).

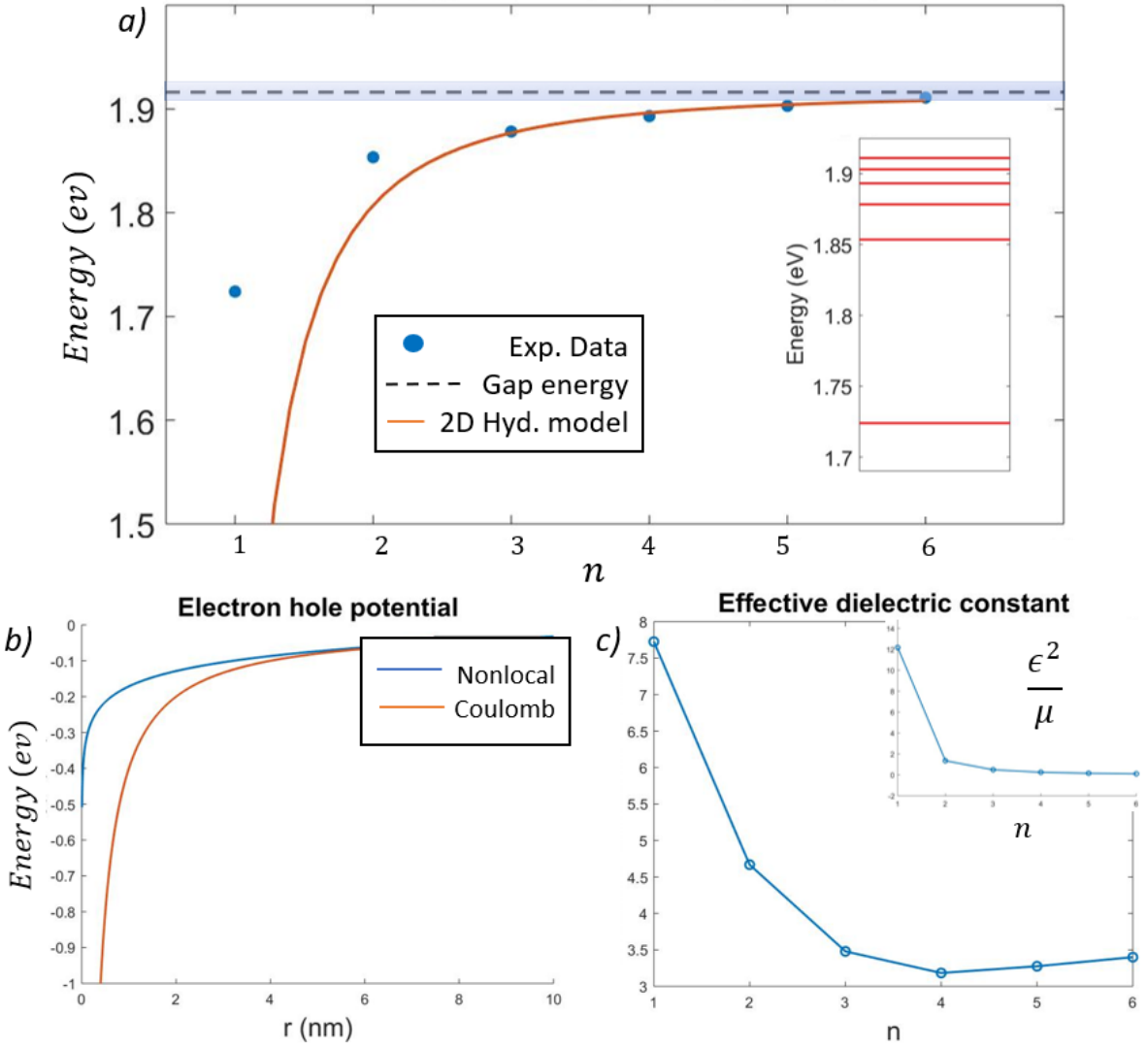

Figure 3.11: *a) Results of the numerical fit on the experimental excitons energies ($n = 3, 4, 5, 6$) for the encapsulated WSe_2 monolayer. The fitting function is 1.29 where E_g and R_y^* were free parameters. The used function is not able to follow the behavior of all the experimental points, this is due to the non-uniform environment of the TMDs monolayer. This result agrees with* **[25]**.*b) Plot of the interaction potential between the electron hole pair forming the exciton. The spatial extent of the coulomb potential is compared to the nonlocal interaction of equation 1.33. c) Experimental ratio $\frac{\epsilon^2}{\mu}$ and effective dielectric constant calculated using equation 1.36: its dependence on n shows the effects of the non-uniform environment.*

To give a justification of this approach and to provide insight into the physics of the non-hydrogenic Hamiltonian, one can use an effective dielectric constant in the 2D

Hydrogenic model. Using table 1.3 a suitable effective mass $\mu = 0.17m_0$ for the exciton can be used, as can be calculated by density functional theory at the K and K' points of the Brillouin zone. The experimental effective dielectric constant, calculated using equation (1.36) is displayed in figure 3.11 c). The equation used is reported hereby for clarity from chapter 1 being $\epsilon_n = \left[2\hbar^2 E_{b,exp}^{(n)} \frac{(n-1/2)^2}{\mu e^4}\right]^{-1/2}$.

The plot of ϵ_n shows a strong decrease in this effective dielectric constant with the quantum number n. Since the inter particle distance is larger in higher lying excitons states, one can infer that the correct physical model for the electron hole interaction is more screened at short range (where the dielectric constant is bigger) but only screened weakly at long distances. In particular, for the $n = 1, 2$ states the dielectric constant is similar to the one of the monolayer WSe_2, around 7.5, while for the excitonic states up to 6s, the value of ϵ_n is almost constant and close to the dielectric constant of the surrounding medium, bulk hBN whose $\epsilon = 3.5$. The fact that the effective dielectric constant is unchanged for states $n = 3, 4, 5, 6$, justifies the empirical use of the 2D Hydrogenic model, that involves a simple coulomb interaction between the particles, for these states only. This is also confirmed by the experimentally calculated ratio $\frac{\epsilon^2}{\mu}$, that decreases for $n > 1, 2$.

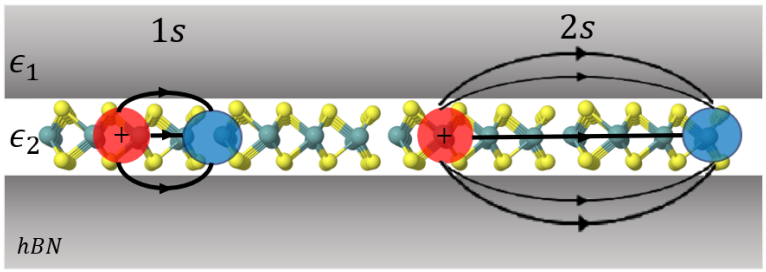

Figure 3.12: *Schematic representation of electron-hole pairs forming 1s and 2s excitonic states in a non-uniform dielectric environment. Note how the spatial extent of the electric field lines in the surrounding medium increases with the inter particle separation.*

This deviation from equation (1.29) can be understood by recalling the non-uniform dielectric environment perceived by the electric field created by the electron-hole pair forming the exciton. The electric field permeates both in the thin monolayer (with larger screening) and in the surrounding medium and its spatial extension is a function of the distance between the particles. That means when the separation between charges increases, a larger portion of the electric field is lying in the hBN with lower dielectric constant and the resulting screening is reduced. This phenomenon is known as anti-screening [**49**] and is responsible for the non-Hydrogenic behavior of excitons in 2D semiconductors. This result is extremely remarkable and is fundamental to describe excitons in van der Waals heterostructures, where the optical properties can be engineered using the dielectric environment the monolayer is embedded in.

A quantitative description of the nonuniform environment, can be obtained using a nonlocal potential in the Schrodinger equation instead of the simple Coulomb interaction

considered until now. In chapter 1 the modified electron hole potential

$$V_{eh}(r) = -\frac{e^2}{8\epsilon_0 r_0}\left[H_0\left(\frac{kr}{r_0}\right) - Y_0\left(\frac{kr}{r_0}\right)\right] \tag{3.4}$$

has already been introduced in (1.33) to describe the electrostatic interaction in a 2D monolayer. Here the most physically significant parameter is r_0, the screening length. The difference between the two potential nominated above can be seen in figure 3.11 b). At short inter particle distance ($r < r_0$), the nonlocal potential goes like $log(r)$: weaker scaling with respect to the $1/r$ coulomb interaction (red curve). For distances larger than the crossover length the two potential have the same functional behavior. The latter is the case of higher lying excitons, where the hydrogenic model is valid. The modified potential is a direct manifestation of the strong dielectric mismatch between the WSe_2 and the surrounding hBN, responsible for the displaced spectral position of $n = 1, 2$ states.

After the analysis of excitonic series in WSe_2 monolayer, it is worth to investigate the effect of different dielectric environment on the gap energy and the excitonic resonances. At the light of the consideration done above on the electron hole electric field extent, the excitonic resonances are expected to be tunable by means of stacking of thin layers in van der Waals heterostructures with dielectric mismatch among the components. Moreover, the excited states are expected to be more affected by dielectric engineering due to the large interparticle separation.

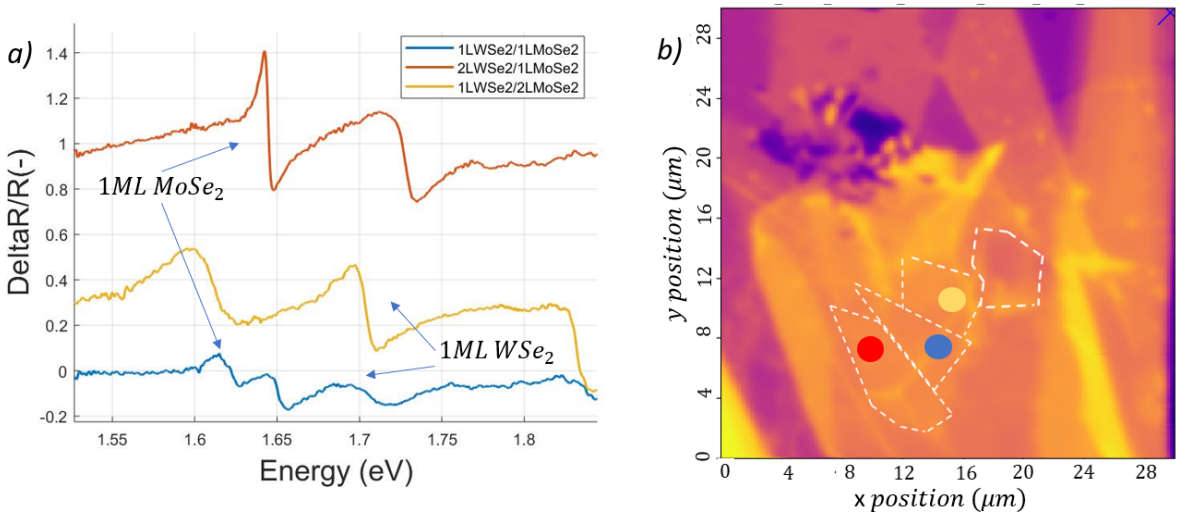

Figure 3.13: *This figure shows the evolution of excitonic transitions of WSe_2 and $MoSe_2$ in the heterostructure. a) Differential reflectivity spectra of three different regions of the sample, whose location is shown aside. Excitons (blue arrows) in monolayer $MoSe_2$ and WSe_2 do not change considerably their spectral location, but a quenching (reduction) in the absorption and a broadening of the transitions can be seen in both cases when passing from the monolayer/bilayer region to the monolayer/monolayer one. b) Spatial map of the reflected light spectrum from our sample obtained with confocal microscope. The regions highlighted contains monolayers/biayers of TMDs and the colored circles indicate the locations whose spectrum is displayed on the left.*

The sample measured is suitable for this kind of investigation since it possesses spatial regions where mono-bilayers of WSe_2 and $MoSe_2$ are stacked together. The differential reflectivity spectrum can be taken for the entire sample and can be used to create a spatial map that allows high resolution imaging of the sample and the identification of the regions of interest within the layer stack. By looking at figure 3.13 b) one can see the mono/bi layer regions contoured by dashed lines.

At first, we want to compare the differential reflectivity spectra of three regions: respectively from the top, 1ML WSe_2/2L$MoSe_2$, 1ML WSe_2/1L$MoSe_2$ and 2ML WSe_2/ 1L$MoSe_2$. The energy transitions of A exciton, *1s* state are presented in figure (3.13 a)) for comparison. From these data emerges that the spectral position of the transition of WSe_2 or $MoSe_2$ is not significantly changing if a monolayer of a different TMDs is stacked onto them with respect to the bilayer case. This can be justified by two argumentations. First of all, the state individuated is the ground exciton state and therefore is almost entirely screened by the TMDs it belongs to, secondly, the change in thickness of the stacked material is not changing significantly from mono to bilayer. What is surprisingly remarkable is the quenching in the absorption at the transition energies when the two monolayers of WSe_2 and $MoSe_2$ are packed together (blue region/ curve).

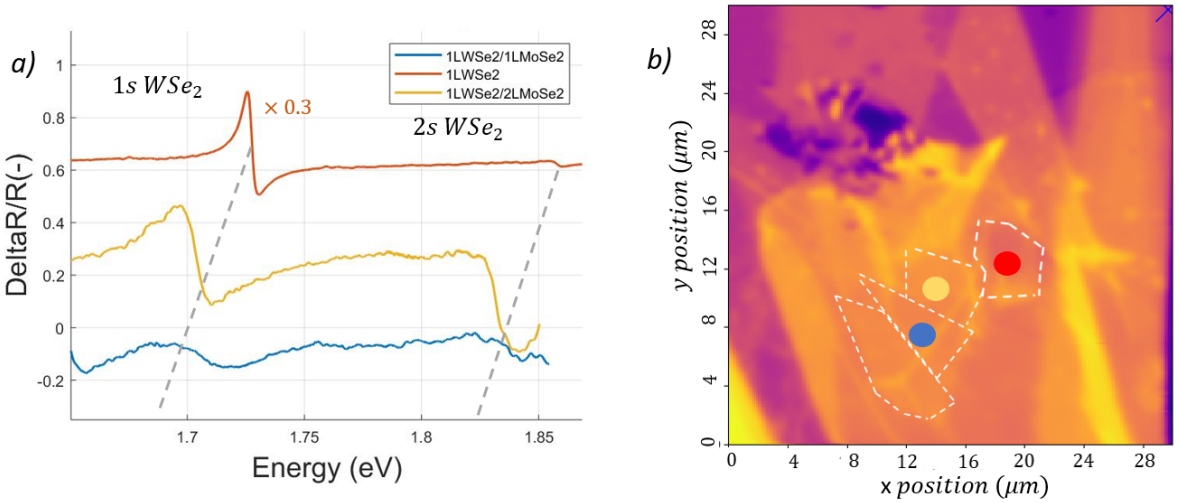

Figure 3.14: *This figure shows the evolution of the 1s and 2s states of A exciton in* WSe_2 *monolayer. In a) the differential reflectivity spectra at* $T = 4K$ *of different regions are displayed. From top to bottom: monolayer* WSe_2 *in hBN (red), heterostructure monolayer* WSe_2 *bilayer* $MoSe_2$ *(yellow) and monolayer monolayer heterostructure. It is possible to notice how the 1s transition is quenched in the heteroregion and how the presence of a TMDs in the neighborhood red-shifts the transition resonances of 1s and 2s states. b) Spatial map of the reflected light spectrum obtained with confocal microscope. Colors indicate corresponding regions analyzed on the left.*

This quenching in the exciton absorption/emission strength has been observed as well when passing from the WSe_2 isolated to the heterostructure. Nevertheless, significant effects of the dielectric environment have been in this case found, and are displayed in figure (3.14 a)). Let us now focus on the *1s* and *2s* states of A exciton in WSe_2 monolayer, regions marked in figure (3.14 b)). If embedded in heterostructure, the

excitonic energies red shift by $20meV$ and the transitions are quenched. This is why we were not able to experimentally access the higher excited states of A exciton as the *2s* is faintly visible. The shift in the resonance energies can be explained in terms of the dielectric screening provided by the high dielectric constant material piled on the absorbing TMD. As expected, since the $MoSe_2$ is less than couple of nanometers thick, the *1s* state with smaller charge separation is affected stronger than the *2s* whose shift is around $10meV$. In the second case indeed the screening is dominated by the encapsulating material, hBN. To summarize, the strength of the Coulomb interaction is reduced by the addition of TMDs layers on top of WSe_2, leading to a decrease in both the exciton binding energy and the bandgap[**27**]. This agrees with what we found using ellipsometry at room temperature.

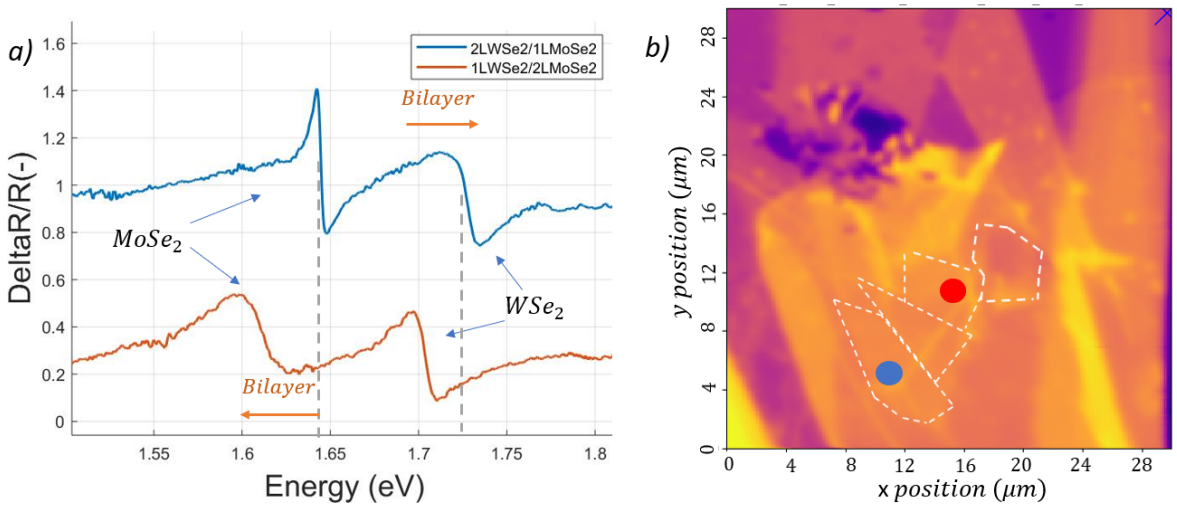

Figure 3.15: *In this figure a comparison between the two bilayer-monolayer regions is shown. a) Differential reflectivity spectra of, respectively, heteroregion bilayer WSe_2 monolayer $MoSe_2$ (blue) and the region monolayer WSe_2 bilayer $MoSe_2$ (red). The excitonic resonances indicated with the blue arrows corresponds to the lower state of A exciton of the two TMDs. Surprisingly, the resonance of WSe_2 results blue-shifted when passing from mono to bilayer while the resonance of $MoSe_2$ is red shifted. b) Spatial map of the reflected light spectrum obtained with confocal microscope. Colors indicate corresponding regions analyzed on the left.*

Another interesting aspect of the excitons in 2D materials is the dependence of the transitions on the thickness of these thin semiconductors. In figure 3.15 the two monolayer/bilayer regions are compared using again the differential reflectivity spectrum at cryogenic temperatures. In particular, the *1s* states of $MoSe_2$ and WSe_2 are spectrally compared in the case of monolayer and bilayer material. The influence of the material thickness manifests itself with a variation in the spectral position of the excitonic transitions. The ground state of A exciton in $MoSe_2$ experiences a red shift when passing from monolayer to bilayer $\Delta E \simeq 12meV$ while, surprisingly, in the case of WSe_2 the *1s* states blue shifts by roughly the same amount. A justification to this can be found in the presence of strain in the heterostructure. Non uniformity of strain can be seen in the presence of folds and wrinkle in the center of the heteroregion. In both cases the bilayer

peak is broader. This behavior is bizarre since the strong similarity of the band structure of TMDs monolayers suggest common features and conduct. Other studies, [**25**] and [**49**], suggest a small change in the transition energy of exciton ground state (typical for quasi-one-dimensional systems) due to the increase of both the exciton binding energy and quasiparticle bandgap, opposite in sign [9].

TMDs	-	$1ML WSe_2$	$1ML/1ML$	$1ML/2ML$	$2ML/1ML$
WSe_2	A exc. 1s	1.724(1)	1.704(1)	1.702(1)	<u>1.726(2)</u>
	A exc. 2s	1.853(1)	1.839(1)	1.831(1)	<u>1.834(1)</u>
$MoSe_2$	intra. #1	-	1.620(1)	<u>1.607(1)</u>	1.644(2)
	intra. #2	-	1.650(1)	-	-

Table 3.6: *Table reporting the experimental energies (in eV) of the excitonic transitions of WSe_2 and $MoSe_2$ in the Moire heterostructure. The data have been accessed using differential reflectivity from a broadband source at cryogenic temperature ($T = 4K$) and by fitting the data numerically by means of the* Mathematica *code described in the appendix. Columns refer to regions in the sample where the environment is different. The underlined values refer to an exciton belonging to a bilayer TMD while other values refer to monolayers. The exciton labeled with intra #1 (intralayer) is supposed to be the 1s excitonic transition.*

The results are summarized in table 3.6. Again the Wolfram Mathematica code described in the appendix was used to determine the spectral position of excitons exploiting a numerical fit of the dielectric function of TMDs modeled using a series of Lorentzian.

In this section the excitons of two TMDs, WSe_2 and $MoSe_2$, have been thoroughly investigated. Broadband differential reflectivity at low temperature allowed to identify excited excitonic states of WSe_2 monolayer up to the quantum number $n = 6$. This allowed to understand and show the nonlocal screening caused by the environment that manifest himself with a deviation of the low ling excitonic states. By adopting a nonlocal screened potential in the form of 1.33 it is possible to understand the effect of a different dielectric constant in the proximity of the monolayer. The possibility of stacking 2D materials in van der Waals heterostructures allows one to engineer the resonance energies of excitons in thin semiconductors. This, together with the large binding energy (around $190meV$) of intraexciton states with high thermal stability, results in a purely excitonic emission and absorption spectra of TMDs. This offers both possibilities for fundamental studies in many body physics and for realization of novel optoelectronic devices.

[9] This phenomenon is known as bandgap renormalization.

3.3 Magnetic field effects on excitons

After a first analysis of excitonic behavior of TMDs in different dielectric environments, to further explore the A exciton Rydberg states one can apply a strong out of plane magnetic field to the sample. This offers a new degree of freedom for tuning of these quasi-particle optical transition, not only for fundamental investigation but also for implementation of excitons in novel devices. In our experiment a magnetic field from $B = -7T$ to $+7T$ has been applied while the sample was shined with broadband circularly polarized light. The reflected light from a single point on the sample was collected by a spectrometer both on the sample and on the substrate, in order to compute the differential reflectivity. The application of a magnetic field significantly shifts the spectral position of the excitonic transitions in WSe_2 and $MoSe_2$ monolayers. The high order states shift more than the low-lying states. Figure (3.16 a)) shows the A exciton Rydberg states in monolayer WSe_2 under magnetic field at the temperature of 4K, as the differential reflectivity is plotted as a function of B_{ext}.

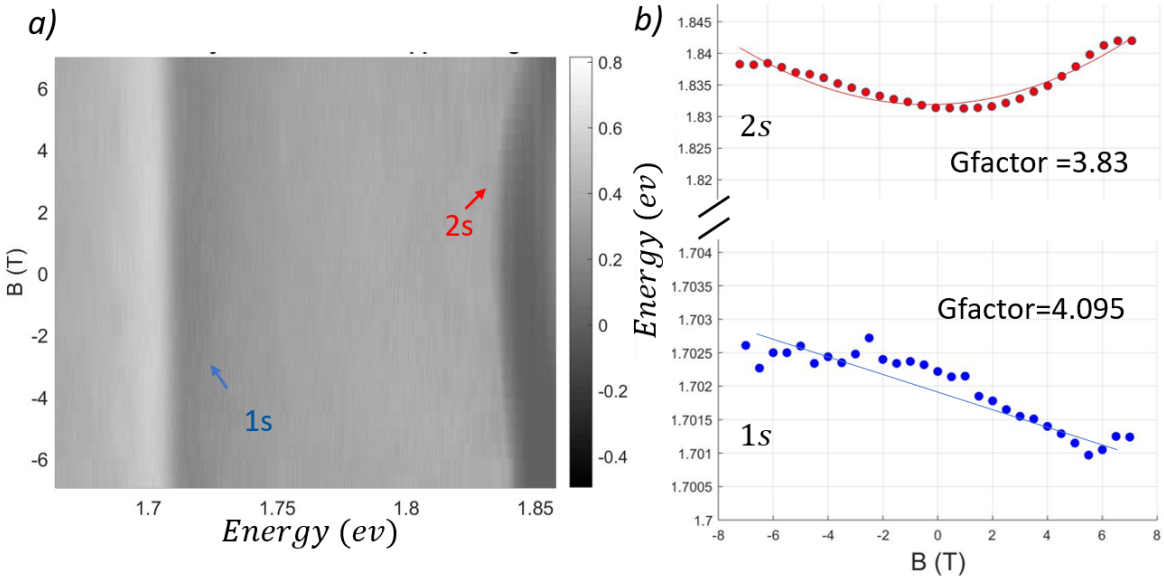

Figure 3.16: *Effects of strong magnetic field (7T) applied to the heterostructure. The 1s and 2s states of WSe_2 bilayer shift their transition energy showing a Zeeman splitting and diamagnetic effect. a) Transition energy of WSe_2 in the 2L/1L region as a function of the applied magnetic field (right handed circularly polarized light) and b) peak positions obtained using Wolfram Mathematica. The circles indicate the experimental points while the solid lines indicate the numerical fit of the magnetic field dependence. Zeeman shift is observed in both the 1s and 2s states while the diamagnetic effect is significant only in the 2s state. This is due to the spatial extent of excitons.*

By looking at the figure, it is clear how the *2s* state experiences a much larger shift if compared to the 1s state. The magnitude of the magnetic effects can be quantitatively measured performing again a numerical fit of the transition peaks. In figure (3.16 b)) the peak shift can be clearly observed when the excitonic peak position is plotted as a function of B_{ext}. It has been already stated how different states of the Rydberg series

evolve differently under the effect of magnetic field. This is due to the combination of two different magnetic effects on the electronic band structure of thin TMDs, the Zeeman shift and the diamagnetic effect. As thoroughly described in chapter 1, the Zeeman shift is an odd function of the B field, and one calls Zeeman splitting the difference between energies at opposite magnetic fields. On the other hand the diamagnetic shift is an even function of B field and its magnitude is the average at opposite magnetic fields.

The two time-reversal valleys (K and K') in monolayer TMDs have opposite spin and orbit configuration. The presence of an external magnetic field enlarges (or respectively, diminishes) the band gap at the two valleys so that the resulting difference between the two optical transitions is proportional to the applied B_{ext}. We recall here the expression for the splitting being $\Delta E_{ZM} = g\mu_B B$, where g is the effective *g factor*. If then one considers the diamagnetic shift, in the weak [10] field limit, one can express it for an exciton as $\Delta E_{DM} = \frac{e^2}{8\mu} < \psi|r^2|\psi > B^2$, where the term containing r^2 is the expectation value of the radial coordinate over the exciton envelope wave function ψ. Two important differences between the two expressions can be highlighted: first the dependence on the B field is quadratic and not linear, and secondly a larger exciton size produces a much larger diamagnetic shift.

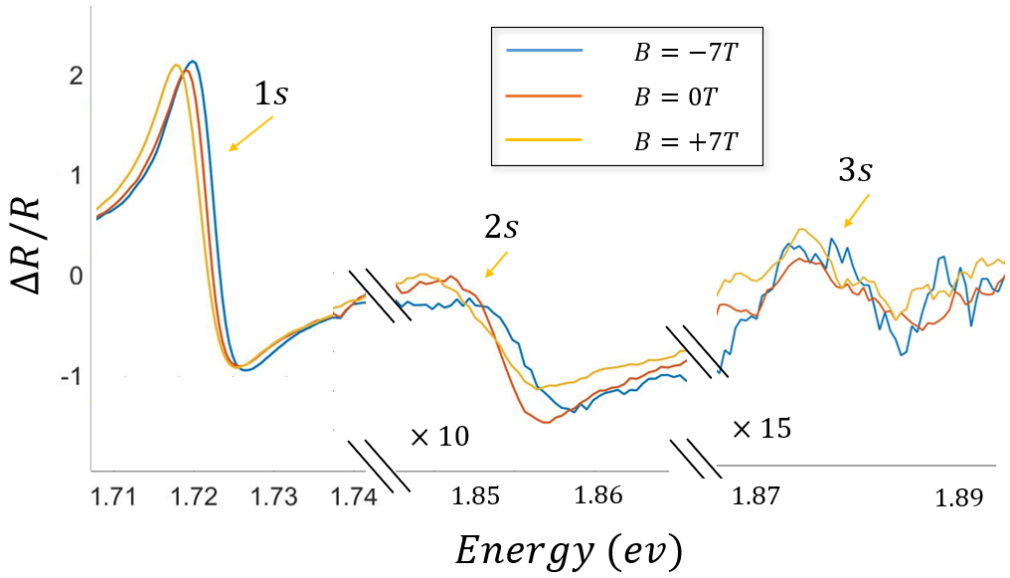

Figure 3.17: *Magnetic effects on exciton resonances in WSe_2 monolayer. Here the differential reflectivity spectrum of the thin TMDs is plotted for different magnetic field applied out of plane. The measurement has been performed with right circularly polarized light. It is possible to see how the diamagnetic shift prevails for states higher than the 2s. For example, the 3s state have the peaks of strong magnetic field, at higher energy with respect to the red peak ($B = 0$), expected for even function with respect to B.*

Both these differences have been experimentally observed in our measurements. As can be seen in figure (3.16), it is now clear why the *1s* state shows a linear shift (with

[10] This means the Landau-level spacing is much smaller than the exciton binding energy, this corresponds to $B \simeq 15T$. For details see chapter 1.

negative slope since this measurement refers to right handed circularly polarized light) while the *2s* presents a superposition of linear and quadratic shift. This is due to the different spatial extent of the exciton envelope wavefunction which increases with the quantum number n. Indeed the root mean square radius of the electron-hole couple in WSe_2 is for the ground state $r_{1s} = 1.68nm$ while for the 2s $r_{2s} = 6.66nm$ [**49**].

We have observed the shift of resonances for all the excited states individuated in the previous section. A comparison between the peaks for different B_{ext} is shown in figure (3.17) in case on $n = 1, 2, 3$ for WSe_2 monolayer again.

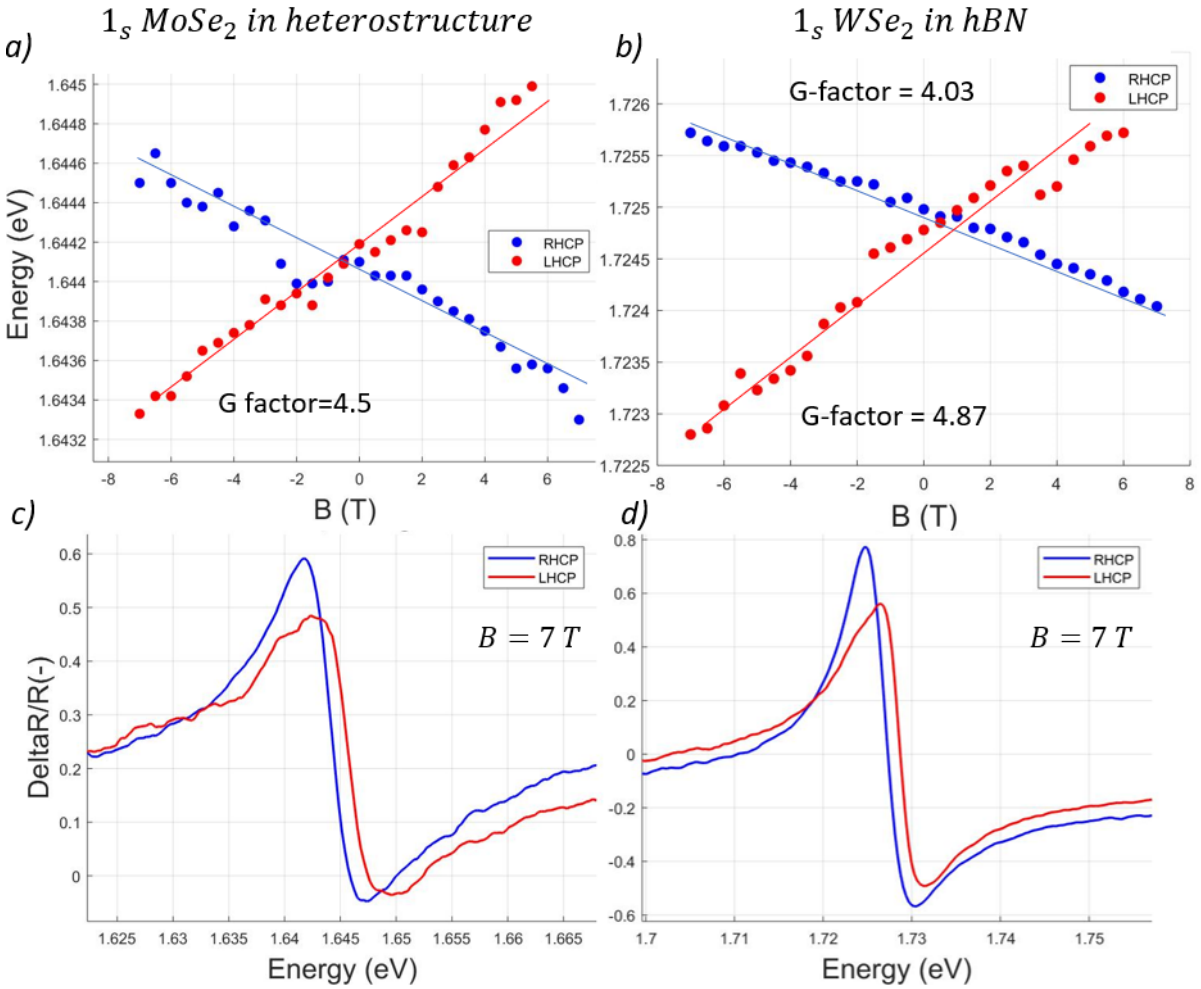

Figure 3.18: *Figure illustrating the effects of magnetic field (up to 7T) on the excitons in TMDs. a) Zeeman shift of the ground state A exciton of $MoSe_2$ monolayer. The two valleys can be accessed with circularly polarized light and the left and right handed polarization states are reported, respectively, in red and blue. The g-factor of the exciton can be extracted by a linear fit of the data (solid line) and its theoretical value is predicted to be 4. b) Zeeman shift of WSe_2 monolayer A exciton (ground state). The calculated g-factors are close to the value predicted by the theory. The difference of the energy levels is called Zeeman splitting. c) and d) peaks corresponding to the excitonic transition of the TMDs: in the presence of strong magnetic field the Zeeman splitting remove the valley degeneracy that can be accessed with σ^+ and σ^- polarized light.*

Figure 3.18 shows the analysis for the *1s* state of $MoSe_2$ and WSe_2 monolayers. In both cases, the major contribution of to the Zeeman splitting has been argued to come from the d atomic orbitals in the valence band whose azimuthal quantum number is $m = 2$ and -2. This means the expected contribution to this linear magnetic effect in the valleys is proportional to a g factor of -4. An experimental value for this effective Lande factor can be found with a numerical fit of the excitonic peaks. By observing the shift for one polarization state (σ^+ or σ^-) one can notice the linearity of $E_{1s}(B)$ meaning the Zeeman effect dominates on the diamagnetic shift and therefore the fitting function has been chosen to be a straight line. The data follow well the solid lines having a slope close to the predicted value of 4. This correspond to a very tiny shift of $\simeq 0.23meV/T$, nevertheless, the two transition at $B = 7T$ are distinguishable since a Zeeman splitting of $\sim 4meV$ occurs between the two spin population i.e. the two valleys, accessed with different polarization states.

Unfortunately, a magnetic field of 7T applied to our sample was not enough to produce a significant shift above the resolution of our measurements for high lying Rydberg states. Stronger magnets might probably allow to observe and also fit the magnetic effects for excited states with $n = 4, 5, 6$. Nevertheless, our experiment confirmed the possibility to access different electronic population with opposite spin using circularly polarized light. This has important consequences in spintronic application and spin investigation. The experiment also shows the time reversal symmetry breaking and the modification of the electronic bandgap that a magnetic field produces on monolayers TMDs. These results provide key-information for optical and optoelectronics application of these 2D semiconductors.

So far, the effects of the dielectric environment and of the magnetic field on the excitons in 2D materials have been separately investigated. However these two effects are not far apart but, by contributing to modifications to the electronic bandgap, they influence each other. A manifestation of the correlation between diamagnetic effect and dielectric environment in the optical properties of TMDs emerges from our measurements and was recently observed in [**50**]. The figure (3.19) is particularly interesting and compares the magnetic effect of an out of plane magnetic field in different spatial regions of the sample. Figure (3.19 a)) shows the evolution of the *2s* state of A exciton of WSe_2 monolayer encapsulated in hBN while figures (3.19 b,c,d)) show the same transition when next to it is stacked $MoSe_2$ with higher dielectric constant[11]. The unexpected difference between the two groups of figures is glaring. Indeed a much more pronounced diamagnetic shift is notable when close to the absorbing material the local dielectric constant is increased.

The physics behind this experimental observation can be explained starting from the expression for the diamagnetic shift in equation (1.16)

$$\Delta E_{DM} = \frac{e^2}{8\mu} < \psi|r^2|\psi > B^2. \tag{3.5}$$

[11] With respect to the hBN. The values of the dielectric constant of the materials composing the sample are reported in table 1.2.

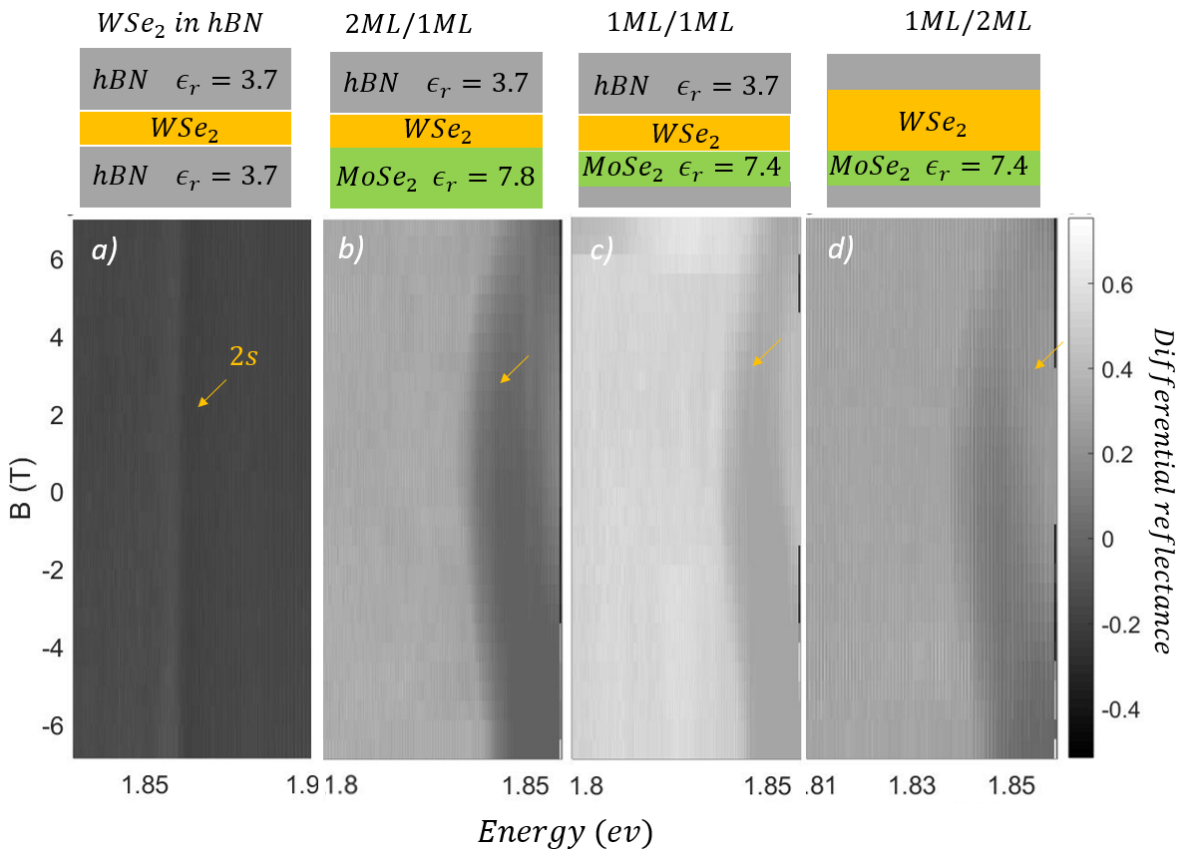

Figure 3.19: *Comparison of the 2s exciton state as a function of the applied magnetic field when the thin TMDs is located in different environments: a) WSe_2 monolayer in hBN, b) WSe_2 bilayer upon $MoSe_2$ monolayer, c) WSe_2 monolayer close to $MoSe_2$ monolayer and d) WSe_2 monolayer next to $MoSe_2$ bilayer. It is remarkable how enhanced the diamagnetic shift is in the heterostructure if compared to the hBN environment. The systematic increase of the diamagnetic shift from a) to b) reveals the corresponding increase of the exciton radius (and simultaneous decrease in exciton binding energy) as the average dielectric constant of the material surrounding the WSe_2 flake is increased.*

The key term is the spatial extent of the electron hole wavefunction. In particular the physical size of the exciton (and also the exciton binding energy) is influenced by the surrounding dielectric environment. This is shown by a small diamagnetic shift of the A exciton resonance. Following figure (3.19) from left to right, respectively, as the dielectric screening around the WSe_2 monolayer is increased, the diamagnetic shift is enhanced consequently. The term $< \psi|r^2|\psi >$ in (1.16) relate the spatial extent of the exciton to its diamagnetic shift, therefore the size of the exciton can be retrieved entirely by this measurement in presence of magnetic field. *The shrinkage of the exciton is therefore due to the reduction of dielectric screening by the surrounding environment.*

This result shows once again how the dielectric environment can be used to engineer the optical properties of thin TMDs[**51**]. Also, in the other way around, the non-local dielectric screening discussed above allows diamagnetic shift measurements to be used to quantify the influence of the surrounding environment on the exciton binding energy[**50**]. This is a peculiarity of 2D materials where the effective dielectric constant seen by a

bound electron hole pair (exciton) depends strongly by their separation[12].

[12]See figure (3.12) to visualize the changes in the electric field extent of excitons.

Chapter 4

Conclusions

In this report, the optical properties of thin TMDs have been investigated. In particular the aspect on which we focused on are the excitonic transition, responsible for sharp peak observed in the absorption spectrum of these materials. The band structure of transition metal dichalcogenides has a direct bandgap that experiences spin-orbit splitting at the top of the valence band: transitions to valence band from these two levels are optically active (allowed by dipole selection rules) and therefore an electron can be excited in the conduction band upon the absorption of incoming radiation. The electron - hole pair can be modeled using the Hamiltonian similar to the one of the hydrogen atom, and the solution of this problem gives rise to a series of bounded states that are called excitons. Excitons are particularly interesting in 2D materials since the lower dimensionality makes the quasi particle to be strongly bounded if compared to the case of bulk material. This makes their investigation feasible, even at room temperature.

The first technique used was ellipsometry in the visible range. The measurements performed in glovebox (Ar atmosphere to avoid contamination of the samples) at room temperature use the light reflected from the sample to obtain information about its optical properties. At first, the refractive index of both $WSe2$ and $MoSe_2$ was modeled as a sum of Lorentzian oscillators and fitted to the experimental ellipsometric angles. This gave us an estimation for the position of energy transitions as well as their linewidth. For these two monolayers, exfoliated and transferred on SiO_2, the first two excited states of the A and B excitons have been found and their spectral position matches the values reported in literature. The WSe_2 monolayer was then encapsulated and, as one expects, the position of the excitons resonances is blue shifted. This can be explained by means of the non-uniform dielectric environment that the charges experience.

Even if ellipsometry is a technique that allows fast measurements, it does not allow us to detect higher excited states mainly for two reasons: the binding energy of $s = 3, 4, 5$ states is lower than the thermal excitations k_bT, and the oscillator strength of these transitions is weaker if compared to other states and does not produce significant features in the ellipsometric angles Ψ and Δ. For this reason we have continued our investigation using confocal microscopy at low temperature (4K). In this case the shined light over the sample is a broad band quartz source, differences in the reflected light from the monolayer and from the substrate can highlight sharp peaks that can be associated to the excitonic transitions in the thin TDMs. We were able to experimentally determine

the spectral location of excited states of the A exciton for $n = 1, 2, 3, 4, 5, 6$ and this allowed us to obtain a more accurate determination of the excitonic binding energies and optical bandgap for WSe_2 encapsulated in hBN. The physical model utilized is the 2D Rydberg model described in chapter 2 whose expression for the energy ladder is

$$E_n = E_g - \frac{R_y^*}{\left(n - \frac{1}{2}\right)^2} \tag{4.1}$$

The remarkable result emerging from our experiments is that the low lying Rydberg states deviate significantly from the Hydrogenic model, respected instead for higher excited states. This is a direct manifestation of the non uniform dielectric environment that can be described by a nonlocal correction to the electron-hole Coulomb interaction. Also, different areas in the sample shown in chapter 3.2 were investigated and significan effects of the dielectric environment has been noted.

By applying a strong out of plane magnetic field, the electronic band structure of 2D TMDs can be modified. Combination of Zeeman splitting and diamagnetic shift in the energy levels of the K and K' valleys manifest itself in the (altered) excitonic transitions. In our experiments we were able to show linear and quadratic effects of excitonic states in WSe_2 and $MoSe_2$ monolayers as a function of the applied field B_{ext}. Also, a more sophisticated and relevant result was the correlation between the electron hole quasi particle (exciton) size and the dielectric environment of the monolayer. This was demonstrated by the increment of the diamagnetic effect on excitons when a material with higher dielectric constant was stacked in the proximity of WSe_2.

A further development to this report might be the investigation of the influence of different dielectric environment on the optical properties in a systematic way. That means the fabrication of samples with a large variety of TDMs monolayers embedded in dielectric of different nature and different thickness. This can be implemented using a different, effective, Hamiltonian for the electron hole pair that considers the dielectric constant of the material surrounding the monolayer as non uniform. An example can be seen in [**48**]. Moreover, the mathematical model for the dielectric function itself, used in this report 2.23

$$\epsilon(\omega) = 1 + \sum_i \frac{f_i}{\omega_i^2 - \omega^2 - i\gamma_i\omega}. \tag{4.2}$$

in spite of its simplicity, does not take into account the absorption continuum for energies above the band gap. A more physically consistent model can therefore be used as for example proposed in [**52**]. In this way, a proper understanding of this complex, multi-body physics might allow the engineering of semiconductor nanostructures for optoelectronic application in quantum optics, light detection and semiconductor physics. At last, the possibility of applying a stronger magnetic field to the sample might allow one to investigate magnetic effects on high order excitonic states of TMDs.

Chapter 5

Appendix

5.1 Appendix A: Matlab code to simulate the ellipsometric parameters

In this section, I will introduce the Matlab code $transfer-matrix-example.m$. The aim of this code is to simulate the ellipsometric angles for a simple physical system that corresponds to the substrate where the exfoliated flakes are transferred and are optically analyzed. The layer stack is composed by SiO_2 slab 100 nm thick on a Si substrate of "infinite" thickness (Figure 5.1 a)). The code uses the experimental dispersion data of the two materials $n_{Si}(\lambda), n_{SiO_2}(\lambda)$ to calculate the transfer matrix of the structure with the formalism in chapter 2.1. In our case the light is shined on the sample and is detected after being reflected back. The angle of incidence (50, 55, 60° in this case) is known and can be adjusted in order to get different plots of Ψ and Δ. From the transfer matrix, one can directly infer the reflection coefficients for different polarization directions and therefore the ellipsometric angles as a function of the incoming wavelength.

Along with the calculated values, the experimental values of Ψ and Δ, measured on the same structures are plotted in the same figure. In this way one can visualize the agreement of the experiment with the calculated model. An example of the output of the code is shown in figure (5.1 b)). The attached files consist of the code, the two dispersion and the Matlab figure that results from the simulation.

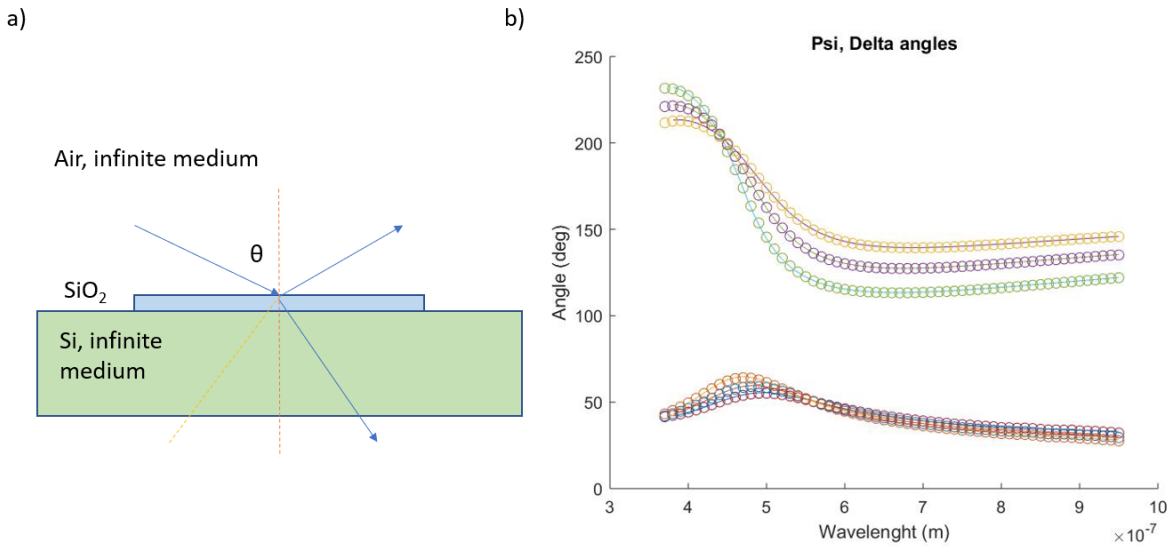

Figure 5.1: *a) Schematic of the structure simulated in the code: 100 nm SiO2 on Si substrate. b) Result of the simulation performed by Matlab. The* Ψ *and* Δ *parameters are plotted for different angle of incidence (*$\theta = 50, 55$ *and* $60°$*) as a function of the radiation wavelength. In solid line the calculated values, dots represent instead the experimental data.*

This code is useful not only to have a preview of the ellipsometric angles of a specific structure, to be compared with the experimental data of a measurement, but also to better understand ellipsometry. In particular how to relate physical quantities such as thickness and refractive index of a layer to the ellipsometric measurements.

5.2 Appendix B: Mathematica code to extract the linewidth

This Section is dedicated to present the code *HeterostructureReflectivity.nb* used in the data analysis for this project. This code has the purpose of computing a numerical model for the light reflected by a multi-layer structure in order to obtain the parameters of the excitonic peaks of the material to be investigated. This is done using a numerical fit of the experimental reflectivity spectrum obtained using a broadband light source.

It is known that the absorption of a layered structure can be calculated using the transfer matrix formalism [1]. The code written in the computational language of *Wolfram Mathematica* is simulating the layered structure our sample is made of and is calculating the Fresnel coefficients and the propagation and transmission matrices for each different material. The dispersions of SiO_2, hBN and Si are imported using the values from literature. The dielectric function of the monolayer has to be obtained instead using a numerical fit of the experimental data. We have decided to model the dispersion of the TMDs according to

$$n(E) = \sqrt{(n+ik)^2 + \frac{A_p}{(E_p)^2 - E^2 - i\gamma E}} \tag{5.1}$$

where n, k are the constant (i.e. independent on photon energy) part of the refractive index, A_p is the oscillator strength, E_p is the resonance frequency and γ is the linewidth (FWHM) of the transition. The refractive index is a complex function of the incoming photon energy and considers only one Lorentz oscillator. This approximation for the dielectric function is valid if we assume that a peak in the broadband reflectivity spectrum, that corresponds to an excitonic transition, is sufficiently isolated and does not overlap with other resonances. If we fit one transition at the time, the approach described produces physically consistent results.

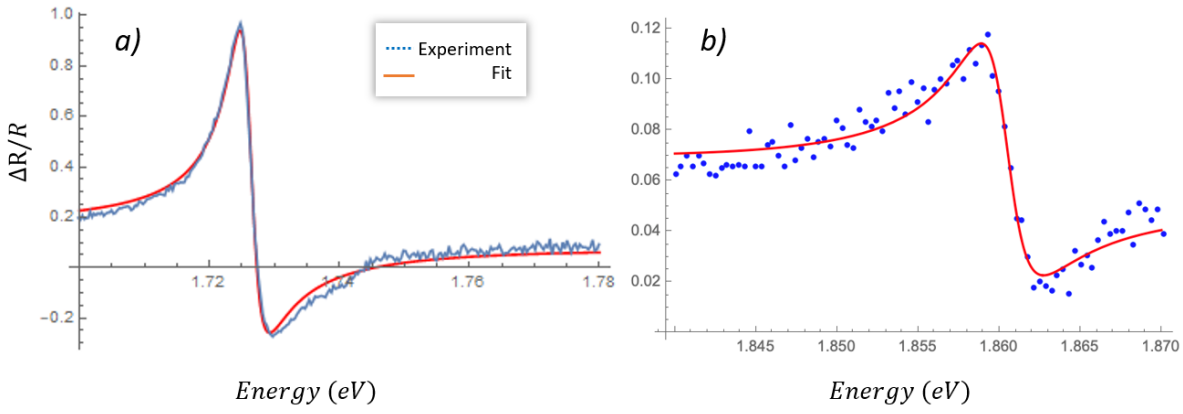

Figure 5.2: *Result of a numerical fit on the excitonic absorption peaks of WSe_2 monolayer encapsulated in hBN. a) and b) are, respectively, the 1s and 2s states of the A exciton.*

The numerical fit is performed by the function *NMinimize* that tries to find a global

[1] A detailed explanation of this method is presented in chapter 2 along with its mathematical derivation.

minimum to the difference between the calculated and the experimental differential reflectivity squared: this gives an estimation for the parameters listed above between the constrains imposed. A result of one fit is presented in figure 5.4.

5.3 Appendix C: Quantum Photonics Laboratories facilities

The research project described in the previous chapters was developed at the Quantum photonics Laboratories of the Physics department at Heriot Watt University (UK). In this section, the laboratories facilities will be presented and briefly described.

The first part of the project took part in the clean room which is fully equipped with modern nanofabrication and characterization setup. This is where the EPSRC Two-Dimensional Photonics Fabrication facility is located. Electron beam evaporators and electron beam lithography instruments are located in the spacious laboratory. My experiments with ellipsometry were conducted in a homemade setup for 2D materials fabrication (all-dry) in an inert environment and an imaging ellipsometer enabling characterization of 2D materials and thin films.

Figure 5.3: *Clean room facility of the department of Physics at Heriot Watt University (UK). In this photo is displayed the glovebox used during the first part of this experimental thesis. It is equipped for 2D fabrication and ellipsometric characterization of thin films in an inert environment.*

In the second part, the characterization of 2D heterostructures with broadband reflectivity, we operated in the labs dedicated to quantum optics and spintronics in solid-state materials. The labs are fitted with state-of-the-art equipment, meticulously selected for low-light experiments.

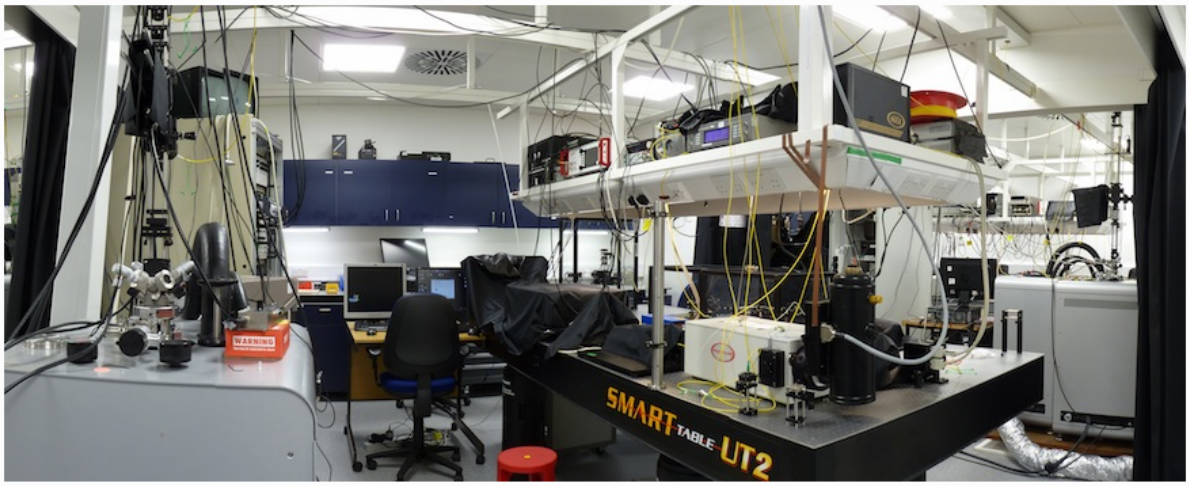

Figure 5.4: *Lab dedicated to quantum optics and spintronics in solid-state materials at HWU. In this photograph it is possible to see on the right the cryostat with the confocal microscope head and an insulating table (center) where spectrometer, lasers and detectors are located. This lab is designed for experiments in low light conditions.*

In particular, one can find high grade tunable lasers, state of the art detectors and spectrometers (using liquid nitrogen cooled cameras) and finally Attocube Atttodry cryostats. These helium-free cryostats for confocal microscopy and solid-state physics, are equipped with superconducting magnets and XYZ piezo motors and scanners to allow for all the freedom needed to explore the sample. It is also located there a broadband Tungsten-halogen light source (ThorLabs), used for our differential reflectivity measurements, which is stabilized in color temperature and output power.

More information can be found on the website of the Quantum Photonics Laboratories at *https* : *//qpl.eps.hw.ac.uk/*.

Bibliography

[1] Voshell, A., Terrones, M., Rana, M. (2018, September). *Review of optical properties of two-dimensional transition metal dichalcogenides.* In Wide Bandgap Power and Energy Devices and Applications III (Vol. 10754, p. 107540L). International Society for Optics and Photonics.

[2] Dragoman, M., Dragoman, D. (2016). *2D Nanoelectronics: physics and devices of atomically thin materials.* Springer.

[3] Novoselov, K. S., Mishchenko, A., Carvalho, A., Neto, A. C. (2016). *2D materials and van der Waals heterostructures.* Science, 353(6298), aac9439.

[4] Ruiz-Tijerina, D. A., Danovich, M., Yelgel, C., Zólyomi, V., Fal'ko, V. I. (2018). *Hybrid kp tight-binding model for subbands and infrared intersubband optics in few-layer films of transition-metal dichalcogenides: MoS 2, MoSe 2, WS 2, and WSe 2.* Physical Review B, 98(3), 035411.

[5] Xiao, J., Zhao, M., Wang, Y., Zhang, X. (2017). *Excitons in atomically thin 2D semiconductors and their applications.* Nanophotonics, 6(6), 1309-1328.

[6] Koperski, M., Molas, M. R., Arora, A., Nogajewski, K., Slobodeniuk, A. O., Faugeras, C., Potemski, M. (2017). *Optical properties of atomically thin transition metal dichalcogenides: observations and puzzles.* Nanophotonics, 6(6), 1289-1308.

[7] Kumar, A., Ahluwalia, P. K. (2012). *Electronic structure of transition metal dichalcogenides monolayers 1H-MX 2 (M= Mo, W; X= S, Se, Te) from ab-initio theory: new direct band gap semiconductors.* The European Physical Journal B, 85(6), 186.

[8] Liu, G. B., Xiao, D., Yao, Y., Xu, X., Yao, W. (2015). *Electronic structures and theoretical modelling of two-dimensional group-VIB transition metal dichalcogenides.* Chemical Society Reviews, 44(9), 2643-2663.

[9] Griffiths, D. J., Schroeter, D. F. (2018). *Introduction to quantum mechanics.* Cambridge University Press.

[10] Arora, A., Koperski, M., Nogajewski, K., Marcus, J., Faugeras, C., Potemski, M. (2015). *Excitonic resonances in thin films of WSe 2: from monolayer to bulk material.* Nanoscale, 7(23), 10421-10429.

[11] Mak, K. F., He, K., Shan, J., Heinz, T. F. (2012). *Control of valley polarization in monolayer MoS 2 by optical helicity.* Nature nanotechnology, 7(8), 494-498.

[12] Kaviraj, B., Sahoo, D. (2019). *Physics of excitons and their transport in two dimensional transition metal dichalcogenide semiconductors.* RSC advances, 9(44), 25439-25461.

[13] Arora, A., Nogajewski, K., Molas, M., Koperski, M., Potemski, M. (2015). *Exciton band structure in layered MoSe 2: from a monolayer to the bulk limit.* Nanoscale, 7(48), 20769-20775.

[14] McIntyre, J. D. E., Aspnes, D. E. (1971). *Differential reflection spectroscopy of very thin surface films.* Surface Science, 24(2), 417-434.

[15] Li, Y., Chernikov, A., Zhang, X., Rigosi, A., Hill, H. M., Van Der Zande, A. M., ... Heinz, T. F. (2014). *Measurement of the optical dielectric function of monolayer transition-metal dichalcogenides: MoS 2, Mo S e 2, WS 2, and WS e 2.* Physical Review B, 90(20), 205422.

[16] Liu, E., van Baren, J., Taniguchi, T., Watanabe, K., Chang, Y. C., Lui, C. H. (2019). *Magnetophotoluminescence of exciton Rydberg states in monolayer WSe 2.* Physical Review B, 99(20), 205420.

[17] Srivastava, A., Sidler, M., Allain, A. V., Lembke, D. S., Kis, A., Imamoglu, A. (2015). *Valley Zeeman effect in elementary optical excitations of monolayer WSe 2.* Nature Physics, 11(2), 141-147.

[18] Liu, E., van Baren, J., Taniguchi, T., Watanabe, K., Chang, Y. C., Lui, C. H. (2019). *Magnetophotoluminescence of exciton Rydberg states in monolayer WS e 2.* Physical Review B, 99(20), 205420.

[19] Stier, A. V., McCreary, K. M., Jonker, B. T., Kono, J., Crooker, S. A. (2016). *Exciton diamagnetic shifts and valley Zeeman effects in monolayer WS 2 and MoS 2 to 65 Tesla.* Nature communications, 7(1), 1-8.

[20] Seyler, K. L., Rivera, P., Yu, H., Wilson, N. P., Ray, E. L., Mandrus, D. G., ... Xu, X. (2019). *Signatures of moire-trapped valley excitons in MoSe 2/WSe 2 heterobilayers.* Nature, 567(7746), 66-70.

[21] Ueta, M., Kanzaki, H., Kobayashi, K., Toyozawa, Y., Hanamura, E. (2012). *Excitonic processes in solids* (Vol. 60). Springer Science and Business Media.

[22] Online resource from: http://homes.nano.aau.dk/tgp/PhD_Course/, *Excitons in Bulk and Two-dimensional Semiconductors.*

[23] Thygesen, K. S. (2017). *Calculating excitons, plasmons, and quasiparticles in 2D materials and van der Waals heterostructures.* 2D Materials, 4(2), 022004.

[24] Wang, G., Chernikov, A., Glazov, M. M., Heinz, T. F., Marie, X., Amand, T., Urbaszek, B. (2018). *Colloquium: Excitons in atomically thin transition metal dichalcogenides.* Reviews of Modern Physics, 90(2), 021001.

[25] Chernikov, A., Berkelbach, T. C., Hill, H. M., Rigosi, A., Li, Y., Aslan, O. B., ... Heinz, T. F. (2014). *Exciton binding energy and nonhydrogenic Rydberg series in monolayer WS 2*. Physical review letters, 113(7), 076802.

[26] Ugeda, M. M., Bradley, A. J., Shi, S. F., Felipe, H., Zhang, Y., Qiu, D. Y., ... Wang, F. (2014). *Giant bandgap renormalization and excitonic effects in a monolayer transition metal dichalcogenide semiconductor*. Nature materials, 13(12), 1091-1095.

[27] Raja, A., Chaves, A., Yu, J., Arefe, G., Hill, H. M., Rigosi, A. F., ... Nuckolls, C. (2017). *Coulomb engineering of the bandgap and excitons in two-dimensional materials*. Nature communications, 8(1), 1-7.

[28] Laturia, A., Van de Put, M. L., Vandenberghe, W. G. (2018). *Dielectric properties of hexagonal boron nitride and transition metal dichalcogenides: from monolayer to bulk*. npj 2D Materials and Applications, 2(1), 1-7.

[29] Berkelbach, T. C., Hybertsen, M. S., Reichman, D. R. (2013). *Theory of neutral and charged excitons in monolayer transition metal dichalcogenides*. Physical Review B, 88(4), 045318.

[30] Berkelbach, T. C., Hybertsen, M. S., Reichman, D. R. (2013). *Theory of neutral and charged excitons in monolayer transition metal dichalcogenides*. Physical Review B, 88(4), 045318.

[31] Jin, Z., Li, X., Mullen, J. T., Kim, K. W. (2014). *Intrinsic transport properties of electrons and holes in monolayer transition-metal dichalcogenides*. Physical Review B, 90(4), 045422.

[32] Mak, K. F., He, K., Lee, C., Lee, G. H., Hone, J., Heinz, T. F., Shan, J. (2013). *Tightly bound trions in monolayer MoS 2*. Nature materials, 12(3), 207-211.

[33] Chernikov, A., Van Der Zande, A. M., Hill, H. M., Rigosi, A. F., Velauthapillai, A., Hone, J., Heinz, T. F. (2015). *Electrical tuning of exciton binding energies in monolayer WS 2. Physical review letters*, 115(12), 126802.

[34] Aivazian, G., Gong, Z., Jones, A. M., Chu, R. L., Yan, J., Mandrus, D. G., ... Xu, X. (2015). *Magnetic control of valley pseudospin in monolayer WSe 2*. Nature Physics, 11(2), 148-152.

[35] Conley, H. J., Wang, B., Ziegler, J. I., Haglund Jr, R. F., Pantelides, S. T., Bolotin, K. I. (2013). *Bandgap engineering of strained monolayer and bilayer MoS2*. Nano letters, 13(8), 3626-3630.

[36] Ross, J. S., Klement, P., Jones, A. M., Ghimire, N. J., Yan, J., Mandrus, D. G., ... Cobden, D. H. (2014). *Electrically tunable excitonic light-emitting diodes based on monolayer WSe 2 p–n junctions*. Nature nanotechnology, 9(4), 268.

[37] Lee, H. S., Kim, M. S., Jin, Y., Han, G. H., Lee, Y. H., Kim, J. (2015). *Selective Amplification of the Primary Exciton in a Mo S 2 Monolayer*. Physical review letters, 115(22), 226801.

[38] Englund, D., Fattal, D., Waks, E., Solomon, G., Zhang, B., Nakaoka, T., ... Vuckovic, J. (2005). *Controlling the spontaneous emission rate of single quantum dots in a two-dimensional photonic crystal.* Physical review letters, 95(1), 013904.

[39] Friedbacher, G., Bubert, H. (Eds.). (2011). *Surface and Thin Film Analysis: A Compendium of Principles, Instrumentation, and Applications.* John Wiley and Sons.

[40] Pedrotti, F. L., Pedrotti, L. M., Pedrotti, L. S. (2017). *Introduction to optics.* Cambridge University Press.

[41] Hinrichs, K., Eichhorn, K. J. (Eds.). (2018). *Ellipsometry of functional organic surfaces and films* (Vol. 52). Springer.

[42] Accurion GmbH (2019),*COMPENDIUM: Principles of Nulling and Imaging Ellipsometry*

[43] Born, M., Wolf, E. (2013). *Principles of optics: electromagnetic theory of propagation, interference and diffraction of light.* Elsevier. Ch. 8

[44] Hogele, A., Seidl, S., Kroner, M., Karrai, K., Schulhauser, C., Sqalli, O., ... Warburton, R. J. (2008). *Fiber-based confocal microscope for cryogenic spectroscopy.* Review of scientific instruments, 79(2), 023709.

[45] Chhowalla, M., Shin, H. S., Eda, G., Li, L. J., Loh, K. P., Zhang, H. (2013). *The chemistry of two-dimensional layered transition metal dichalcogenide nanosheets.* Nature chemistry, 5(4), 263.

[46] He, K., Kumar, N., Zhao, L., Wang, Z., Mak, K. F., Zhao, H., Shan, J. (2014). *Tightly bound excitons in monolayer WSe 2.* Physical review letters, 113(2), 026803.

[47] Hanbicki, A. T., Currie, M., Kioseoglou, G., Friedman, A. L., Jonker, B. T. (2015). *Measurement of high exciton binding energy in the monolayer transition-metal dichalcogenides WS2 and WSe2.* Solid State Communications, 203, 16-20.

[48] Molas, M. R., Slobodeniuk, A. O., Nogajewski, K., Bartos, M., Babiński, A., Watanabe, K., ... Potemski, M. (2019). *Energy spectrum of two-dimensional excitons in a nonuniform dielectric medium.* Physical review letters, 123(13), 136801.

[49] Deslippe, J., Dipoppa, M., Prendergast, D., Moutinho, M. V., Capaz, R. B., Louie, S. G. (2009). *Electron-hole interaction in carbon nanotubes: novel screening and exciton excitation spectra.* Nano letters, 9(4), 1330-1334.

[50] Stier, A. V., Wilson, N. P., Clark, G., Xu, X., Crooker, S. A. (2016). *Probing the influence of dielectric environment on excitons in monolayer WSe2: insight from high magnetic fields.* Nano letters, 16(11), 7054-7060.

[51] Cudazzo, P., Tokatly, I. V., Rubio, A. (2011). *Dielectric screening in two-dimensional insulators: Implications for excitonic and impurity states in graphane.* Physical Review B, 84(8), 085406.

[52] Toyozawa, Y. (1962). *Further Contribution to the theory of the line-shape of the exciton absorption band.* Progress of Theoretical Physics, 27(1), 89-104.